ANGULAR DISTRIBUTION OF THE PRODUCTS OF NITRIC OXIDE DISSOCIATION THROUGH RYDBERG STATES AND HIGH RESOLUTION COHERENT THREE DIMENSIONAL SPECTROSCOPY OF BROMINE

A Dissertation

Presented to the Faculty of the Graduate School

of Cornell University

in Partial Fulfillment of the Requirements for the Degree of

Doctor of Philosophy

by

Benjamin Richard Strangfeld

May 2014

ANGULAR DISTRIBUTION OF THE PRODUCTS OF NITRIC OXIDE DISSOCIATION THROUGH RYDBERG STATES AND HIGH RESOLUTION COHERENT THREE DIMENSIONAL SPECTROSCOPY OF BROMINE

Benjamin Richard Strangfeld, Ph.D.

Cornell University 2014

The first portion of this dissertation focuses on the velocity mapped imaging experiments that have been used to study the angular distribution of the products of nitric oxide predissociation following its excitation to the *11s*, *10p*, *11p* and *9f* Rydberg levels based on the NO^+ ($X\ ^2\Sigma^+$) core. Ion dip spectra of the Rydberg states were recorded along with velocity-mapped images at the major peaks. Theory is presented based on previous analyses of Hund's coupling cases (a) and (b) and has been modified to include transitions to states of case (d) coupling. The reasonable agreement of the calculated and experimental anisotropy parameters β_2 and β_4 shows the predictive value of the theory.

The second portion of this dissertation explores high resolution coherent multidimensional spectroscopy as an alternative to conventional methods for generating rotationally resolved electronic spectra of gas phase molecules. In addition to revealing information such as the relationships among peaks, it can provide clearly recognizable patterns for systems that otherwise appear patternless due to rotational congestion. These patterns depend upon the scanning strategy and the corresponding four wave mixing process. The background and theory necessary for using high resolution coherent 3D spectroscopy are presented, including pattern prediction and dependence upon rotational constants and quantum numbers. These tools are then applied to a detailed rotational-vibrational analysis of bromine gas.

BIOGRAPHICAL SKETCH

The author was born in Ridgewood, NJ in 1982 and grew up nearby in Ramsey, NJ. He graduated from Ramsey High School in 2000, and his desire to pursue the physical sciences had already become evident. Upon attending Rutgers University, he joined a research group as an undergraduate, where he investigated protein folding and aggregation using dynamic light scattering. In 2004 he graduated from Rutgers, receiving a B.A. in Chemistry with a minor in Physics.

In July of 2005, the author began a Ph.D. program at Cornell University. His experience and interest in photochemistry led him to join the research group of Professor Paul Houston later that year. After completing the necessary coursework and requirements, he received his Masters in Physical Chemistry early in 2008. Soon after, Professor Houston became the Dean of Science at the Georgia Institute of Technology, and the Houston lab moved from Ithaca, NY to Atlanta, GA. By the end of 2008 the lab was becoming operational again, and he spent the next couple years assisting the senior members of the research group with their projects.

While pursuing his research on the dynamics of Rydberg molecules with the assistance of Dr. Houston and Dr. Jun Chen, he began assisting a former Cornell graduate, Dr. Peter Chen, who is a professor at Spelman College in Atlanta. This work turned into a lengthy collaboration on the development of High Resolution Coherent Three-Dimensional Spectroscopy. While it was difficult to split time between two laboratories working on two rather different research projects, the experience with both principle investigators and their approach to research was well worth the time and effort.

For my family

ACKNOWLEDGEMENTS

My interest in science was partly derived from my inquisitive nature, however I cannot begin this section of acknowledgements without recognizing the excellent science teachers and professors I had at Ramsey High School and Rutgers University. Perhaps most importantly I should thank my mother and father, who always encouraged me to set goals and strive for them, and that all things worth achieving are only done so with dedication and effort. I could not have done this without their support.

I would like to thank my special committee members. I appreciate the early collaborative group meetings with Professor Davis and his research group, and especially for stepping in as my committee chair after the Houston group moved to Georgia Tech. Professors Ezra and Loring were instrumental in my instruction at Cornell University, and always took the time to aid me with any difficulties I had with the course material. I am thankful for their time and patience.

The members of the Houston research group, especially Clarice Kelleher Ulrich and David Lee, were responsible for showing me the ropes in the laboratory setting, and I am grateful to them. Dr. Jun (Jack) Chen was a truly amazing person to work under in a lab setting. I learned so much about laser systems, optics, electronics, and analysis from him, and I am convinced that there is not a problem that we could ever encounter in the lab that Jack could not fix.

As strange as it sounds, it was somewhat fortunate that the Houston lab had some equipment problems late in 2011, as it allowed me to begin collaborating with Dr. Peter Chen. I welcomed the challenge of exploring a new technique, and what started as a short-term sharing of ideas turned into two years of working together. I appreciate the way he encouraged me to

overcome obstacles in the laboratory and analysis, and the trust he had in my findings and opinions. It was a great experience working with Peter.

Finally, we come to the person who has had the most influence on my scientific career, Dr. Paul Houston. Paul is exactly the type of person one would want as their advisor. Whatever the topic, Paul was always able to point me in the right direction, and so often in a way that was uniquely logical. He has a way of explaining things that is perfect whether you are a first year student or an expert in the field. As I got to know Paul better, I was so impressed by all he has accomplished; he excels at everything he does. I am very grateful for having had the opportunity to work with you, Paul, and thank you.

TABLE OF CONTENTS

LIST OF FIGURES

LIST OF TABLES

Chapter 1

1. Introduction to Photofragment Imaging

The ability to garner detailed information about the kinetics and dynamics of gas phase reactions has been an important field of study over the last half century. The development of flash photolysis by George Porter and coworkers[1] around 1950 was the first step forward in being able to spectroscopically study the reactions of atoms, molecules, and free radicals. The primary spectroscopic tool at the time was absorption spectroscopy, and often it was not possible to detect intermediates of reactions that were not present on a long time scale, or products of reactions that were too low in concentration to be directly measured. By recording spectra on a one-twenty thousandth of a second time scale from the flash tubes, it was possible to resolve spectroscopic lines from species whose concentrations were very small or intermediates whose lifetimes were rather short.

Later, in 1969, Diesen et al.[2] first demonstrated photofragment recoil spectroscopy (PRS), and their experiments were an early example of a photofragment translational spectroscopy (PTS). This technique was one of the first to demonstrate the ability to determine the angular distribution of products from a photodissociation reaction. By rotating the direction of the linearly polarized photolysis laser using a half-wave plate and taking several measurements at different angles with respect to the direction of the molecular beam, Diesen and coworkers were able to determine the angular distribution of chlorine ions from the photolysis of molecular chlorine. The chlorine ions were mass selected by the use of a quadrupole mass

spectrometer. Similarly, at the time, Riley and Wilson[3] were performing experiments on iodine from alkyl halide dissociation.

Another method used to mass select the products of a photodissociation reaction is time of flight mass spectrometry (TOFMS). In TOFMS, the species of interest is carried by an inert gas in a molecular beam, where is it then intersected by the photolysis laser. The resultant cloud of ions and neutrals will be subject to an external electric field, which accelerates any ions into a field-free flight tube of known length. The time of flight of the ions is recorded by a detector, and the mass to charge ratio of the ion can be determined from the length of the flight tube and the time of flight, as shown by Wiley and McLaren.[4]

1.1 Molecular Beams

Molecular beams are widely used in the study of gas phase dynamics because molecules in molecular beams have several desirable qualities. Molecules in the beam have a generally well defined direction of flow, the local velocity distribution of the molecules in the beam is quite small, and the number density of molecules in the beam is low enough that most collisional effects are avoided. The use of nozzle beams employed in the experiments mentioned to this point was first proposed by Kantrowitz and Grey[5] in 1951, as an improvement upon what was referred to as the oven nozzle. As opposed to the oven beam which worked by effusion through two slits, they proposed using a supersonic nozzle. Expansion from high backing pressure behind the nozzle, through a small aperture into a very low pressure region converts most of the

random translational and internal energy of the bulk gas into directed translational motion after the nozzle. In both the oven beam and the nozzle beam, a secondary slit, often called a skimmer, was placed downstream from the first slit or nozzle to further collimate the beam. However since the supersonic nozzle has some "precollimation" effects on the beam when compared to the oven beam, it was proposed that the intensity of the nozzle beam would be appreciably higher than the previous oven beam.

After several experiments showed the beam intensities and velocity distributions did not quite come to match the theory proposed by Kantrowitz and Grey, Anderson and Fenn[6] then refined the theory of nozzle beams. In their approach it was assumed that the gas stream at the skimmer entrance has a three-dimensional Maxwell distribution of molecular velocities for stream temperature T_s, superimposed on the stream flow velocity v_s. They further assumed that upon entering the skimmer, the molecules would no longer undergo collisions with each other or with the walls of the skimmer, meaning the trajectories and velocities of the molecules in the final beam are the same as those of the molecules entering the skimmer. Under these conditions, Anderson and Fenn were able to determine T_s and v_s as follows:

$$v_s = M \sqrt{\gamma k T_s / m}$$

$$T_s = T_0 \left(1 + \frac{\gamma - 1}{2} M^2\right)^{-1}$$

where M is the Mach number, defined as the ratio of the average speed to the local speed of sound, γ is the specific heat ratio C_P/C_V of the gas, k is the Boltzmann constant, m is the mass of the species in the beam, and T_0 is the nozzle stagnation temperature. With increasing Mach

number the velocity distribution narrows, and the peak of the distribution shifts towards higher velocity. The terminal Mach number sets the conditions where collisions in the beam stop, and

$$M_T = 1.17\ Kn^{-0.4}$$

where Kn is the Knudsen number, which is related to the mean free path of the species in the beam. In this case, $Kn = \frac{1}{\sqrt{2} D n_0 S}$, where D is the diameter of the nozzle, S is the effective molecular collisional cross section at the nozzle, and n_0 is the stagnation number density. The beam intensity a distance *l* downstream from the skimmer thus will be:

$$I_0 \approx A_s\ n_s\ v_s\ (\pi\ l^2)^{-1}\ (\frac{1}{2}\gamma M_s + \frac{3}{2})$$

where A_s is the skimmer entrance area and n_s is the number density at the entrance to the skimmer. This statement holds true for Mach numbers greater than 3. The number density at the skimmer entrance is approximately related to the stagnation number density by the expression $n_s \approx .157\ n_0\ (l/D)^{-2}$, where this expression assumes ideal gas behavior, and a distance *l* that is at least four times larger than D. Finally, the beam intensity for a distance r off the axis of the beam, at a distance *l* downstream from the skimmer will be:

$$I_r \approx A_s\ n_s\ v_s\ (\pi\ l^2)^{-1}\ (\frac{1}{2}\gamma M_s + \frac{3}{2})\ \exp(-\frac{1}{2}\gamma M_s^2 r^2/l^2)$$

which holds true as long as the Mach number is greater than 4 and $r/l < 0.1$.[6]

1.2 State Selective Techniques

By employing electron impact ionization and mass spectrometric detection, experiments to this point in time had the ability to be product selective, however the selectivity was achieved through the mass of the product and thus was not quantum state specific.[7]

1.2.1 Laser Induced Fluorescence

When tunable laser sources became more commonplace in the laboratory setting, several state selective methods came about. In 1972, Zare and coworkers[8] performed laser induced fluorescence (LIF) experiments on the product barium oxide from the reaction of Ba + O_2 in a molecular beam. By scanning a tunable dye laser through many v", J" → v', J' transitions in the A-X band system of BaO and by monitoring the resultant fluorescence, they were able to determine the vibrational-rotational distribution of the products of the reaction in the molecular beam.

1.2.2 Resonance Enhanced Multiphoton Ionization

Another method that was made possible by the advent of tunable laser systems is resonance enhanced multi-photon ionization (REMPI). Like LIF, REMPI allows the observer to determine the quantum states of the products of molecular beam experiments. Whereas LIF to this point had been used to detect the quantum states of products from these reactions, employing a REMPI tagging scheme in these experiments allows for the selection of the quantum state of the product ions, which are then detected by another means, such as an electron multiplier or multichannel plate detector. In an experiment using REMPI tagging, a photolysis laser breaks a bond in a species in the molecular beam, and one of the two products of that bond cleavage is ionized via a REMPI scheme. It is also possible to detect the products of collisions using this technique, for the example of dual molecular beams, a product of photolysis in one beam parallel to another could cause reactive collisions in the second beam, and REMPI can then be used to ionize a product of the collision.

For many neutral products of molecular beam reactions, photoionization requires the absorption of more than one visible-to-ultraviolet photon of light. The probability of such a multiphoton excitation occurring is greatly increased when there is a real excited electronic state of the neutral product that is resonant with the frequency of one of the photons involved in the REMPI tagging. It is possible to use this technique such that 1 or more photon energies can be required to reach this excited electronic state, however it is necessary that there be sufficient overlap between the states that the transition probability is larger than zero. Also, the excited state must have a long enough lifetime to allow the absorption of yet another photon, which will

have sufficient energy to ionize the product from the excited electronic state.[9] If one or two photons is required to reach the intermediate electronic state, it is referred to as 1+1 REMPI or 2+1 REMPI respectfully. Also, if the final ionizing photon is of the same frequency as the excitation photons, as opposed to being of a different frequency, it would be referred to as 2+1 REMPI as opposed to 2+1' REMPI respectfully. Figure 1.1 shows an excitation diagram that represents a common 2+1 REMPI scheme.

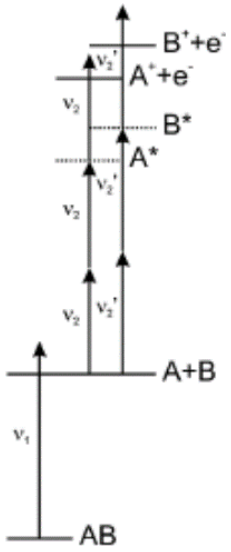

Figure 1.1. Excitation diagram of a 2+1 REMPI process. One photon of frequency ν_1 has sufficient energy to break the bond between the A and B fragment of species AB. Frequency ν_2 is used in the 2+1 REMPI tagging of product A, and frequency ν_2' is used in the 2+1 REMPI tagging of product B.[7]

In Figure 1.1, ν_1 represents the frequency of the photolysis laser. For 2+1 REMPI tagging of product A, there must be a real excited electronic state denoted A*, that is $2\nu_2$ in energy higher than the resultant state of product A, and this state must have a nonzero two photon transition possibility, and also have a sufficiently long lifetime to allow the absorption of another photon of

ν_2 which ionizes product A. Figure 1.1 also shows an analogous process for product B using a tagging laser frequency of ν_2'.

A photolysis event occurs in the volume with which the profile of the laser overlaps the volume of molecular beam, and at that instant in time the products of the event begin expanding in a series of concentric spheres, called Newton spheres.[7] The velocity at which the products recoil from each other, forming these spheres, is related to the amount of energy of the incident photolysis photon, as well as the dissociation energy, and the amount of internal energy that remains in the products. For the example of the dissociation of species AB into products A and B in Figure 1.1, the total energy equation would be:

$$E_{photon} = E_{dissociation,\ AB} + E_{internal,\ A} + E_{internal,\ B} + \tfrac{1}{2}m_A v_A^2 + \tfrac{1}{2}m_B v_B^2 \ .$$

The REMPI lasers must interact with the product some time after the photolysis event has occurred, and therefore the products of the reaction will be expanding with some nonzero velocity. Any product that has a component of its velocity vector in the direction either towards or away from the incoming REMPI laser field will resonantly absorb light either at a slightly higher or lower frequency when compared to a stationary product or a product moving exactly perpendicular to the field. The frequency of the REMPI laser must then be scanned over a small range of frequencies, which corresponds to the Doppler profile. Failure to do so will result in portions of the Newton sphere being preferentially ionized, which will cause an overall loss of information.

1.3 Velocity Map Imaging

The next important advancement in the field of photofragment imaging came in 1987 when David Chandler and Paul Houston[10] laid the foundation for a technique that became known as velocity map imaging (VMI). By employing a REMPI scheme and utilizing the Doppler technique to ionize the quantum state selected products in the resulting Newton spheres from a molecular beam experiment, they were able to detect a two dimensional projection of the three dimensional spatial distribution of the desired product ion. Figure 1.2 shows a diagram of the steps involved in velocity map imaging.

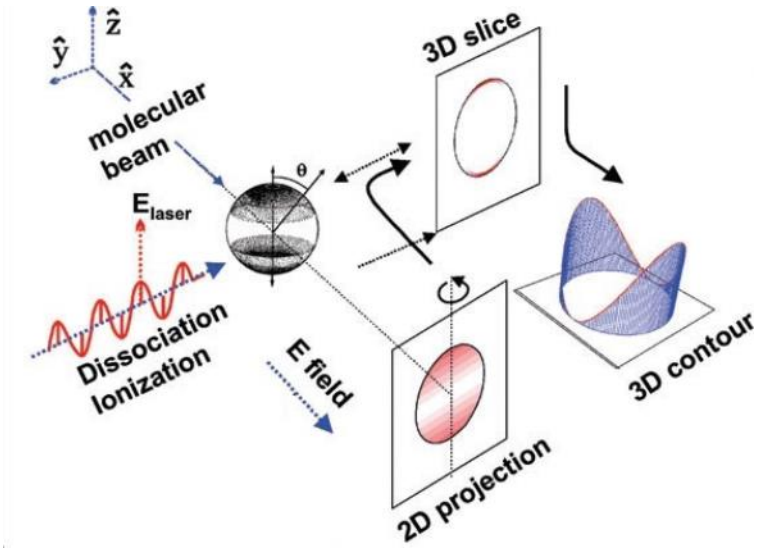

Figure 1.2. A schematic diagram of the steps involved for measuring Newton spheres from dissociation via imaging. See text for details.

The first step is the photodissociation of molecules in a molecular beam with linearly polarized light whose polarization direction is parallel to the face of the detector. The next step is the

ionization of the products of the photodissociation that form Newton spheres by REMPI or another ionization scheme. The ions then interact with the two dimensional position sensitive detector, forming a 2D projection of the Newton spheres. Finally, the two dimensional projection is mathematically converted back to a three dimensional data set.[7] A technique proposed by Arthur Suits[11], where the CCD camera that captures the image can be timed to only record what would be the "center slice" of the Newton sphere, makes the mathematical transformation of the image much simpler.

1.3.1 Electrostatic Lens

About a decade later, Eppink and Parker[12] incorporated an electrostatic lens into the VMI technique to address blurring issues present in the experiments to this point. Since the interaction volume between the molecular beam and the waist of the ionizing lasers is not infinitely small, particles in the Newton spheres that are ionized and then accelerated towards the detector will have small spatial differentiations due to the slightly different locations where they are ionized. The electrostatic lens consists of three spaced, circular electrodes, which in order starting from the molecular beam side of the apparatus are referred to as the repeller, the extractor, and the ground electrode. During an experiment, photodissociation and ionization occur at a point between the repeller and extractor electrodes, both to which positive voltages are applied. The lens serves to "focus" the ions created with the same velocity to the same position on the 2D detector, regardless of where in the interaction volume the ion is generated. The

spacing between the electrodes and the ratio of the voltages applied to the repeller and extractor determine the specifics of the electric field experienced by the resultant ions, which can be simulated prior to experimentation using software such as Simion 6.0.[13] Figure 1.3 shows simulated trajectories for ions generated in a finite volume, interacting with the electrostatic lens.

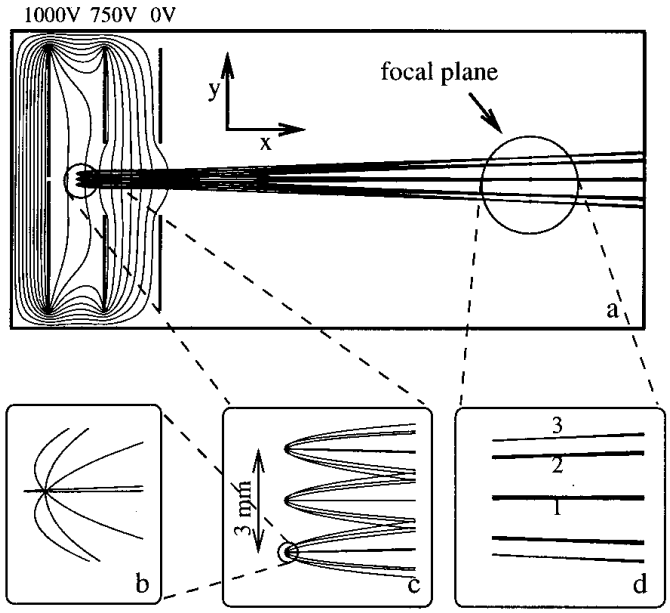

Figure 1.3. a) Total view of the simulated ion trajectories. b-d) Focused view showing that for each point in the 3mm ionization length of the incident laser, ions are generated with several trajectories, simulating spherical expansion. Regardless of the location at which the ions generated, the trajectories come together at the focal plane, with 1, 2, and 3 in panel d) illustrating 0°/180°, 45°/135°, and 90° ejection respectively.[12]

The images utilizing the electrostatic lens have significantly better resolution than the previous images taken using grid electrodes, which limited transmission, could affect trajectory, and did not compensate for the nonzero interaction volume between the input fields and the molecular

beam. Figure 1.4 shows an example of images of O^+ ions from O_2 $3d\pi$ ($^3\Sigma_{1g}^-$) ($v = 2$, $N = 2$) ← $X\ ^3\Sigma_g^-$ Rydberg excitation around 225 nm.[12]

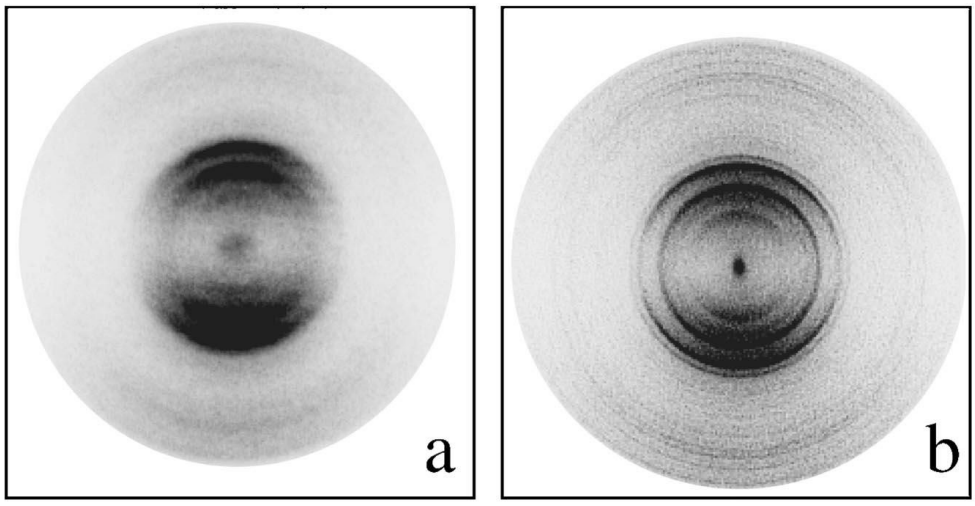

Figure 1.4. a) O^+ ion image measured with the fine mesh grid. b) The same imaged measured with the electrostatic lens.[12]

Vrakking and coworkers[14] soon after incorporated an einzel lens in conjunction with the electrostatic lens proposed by Eppink and Parker. By manipulating the charge ratio of the plate electrodes in the einzel lens, it became possible to magnify or reduce the size of the image created in absence of the einzel lens.

1.3.2 Ion Counting

One further step to the improvement of image resolution came with a technique developed by Paul Houston and coworkers[15] referred to as ion counting. When a single ion impacts a position sensitive detector, such as the MCP/Phosphor assembly used in VMI experiments, an area of about 5x5 pixels of signal is recorded by the image intensified CCD camera for each ion hit. The intensity distribution of this area approximately follows a two dimensional Gaussian profile, with the center of mass of the charge distribution for a single ion located at the peak. For thousands of ion events per image, this effect can cause significant blurring of the data. The ion counting approach analyzing each event as it is recorded, finding the centroid of the area associated with each ion impact and replacing that area of pixels with a single pixel. The accumulated assembly of single pixel events results in an image with better defined features and should facilitate the subsequent analysis.

1.3.3 Image Reconstruction

Once the 3D Newton sphere of products is collapsed onto the 2D imaging detector, or similarly, once the center slice of the sphere is captured on the detector, steps must be taken to mathematically reconstruct the three dimensional data. For systems with cylindrical symmetry it is possible to convert the two dimensional projection from the detector into a three dimensional velocity distribution using the inverse Abel transform. However, when there is alignment in the

system, it is often not possible to directly invert the data. Many of these studies require the use of a forward convolution method, where images are simulated based on a trial scattering distribution and compared with the experimental data, or conversely simulating and fitting a set of basis images and comparing to the experimental image in order to extract the parameters of interest. A common program that employs the latter procedure is Basis Set Expansion (BASEX),[16] which expands the 2D projection in a basis set of functions that are analytical projections of well-behaved Gaussian-like functions. Polar Basis Set Expansion (pBASEX)[17] differs from BASEX in that pBASEX first converts the detected image to polar coordinates prior to inversion, which results in the noise from the conversion being localized to the center of the image as opposed to along a central line as is found when utilizing BASEX.

1.4 Interpretation of the VMI Data

1.4.1 Velocity

When the product of a photodissociation event is ionized and detected by VMI, assuming the experiment is planned correctly and the instrumentation is functioning properly, the resulting data will appear as concentric rings on the 2D position sensitive detector. Determining the velocities of the product ions is relatively straight forward. The time of flight on the ions is measured during the experiment, again it is defined as the difference between the time ionization of the product and time the ions are detected. The distance at which a ring of ions appears from the center of the detector, along with the time of flight, gives one of the vector components of the

total velocity vector. For example, product ions with higher velocities will form rings further from the center of the detector than ions with lower velocity. Since the distance between where the ionization laser interacts with the products of photodissociation from the molecular beam and the detector is also known prior to the experiment from the instrumentation schematics, the angle of the trajectory of the product is also known. From these pieces of information, the velocities and therefore the kinetic energies of the product ions can be determined.

1.4.2 Angular Distribution

The other characteristic of the data besides the distance of the ring from the center of the image, is the weighting or alignment of the ring itself. While it is certainly possible for a ring of data to be completely homogeneous over the entire circumference of the ring, that is not always the case. Often it is found that certain sections of the ring, whether it be along the north and south "poles" of the ring, or along an equatorial line, there is a heavier concentration of ion impacts than in other sections of the ring. This anisotropy must be due to the interaction of some characteristic of the molecule with the linearly-polarized input laser fields. Zare and Herschbach[18] proposed that the angular distribution of the products of photodissociation would be determined by the orientation of the electronic transition dipole moment in the molecule and the direction of the polarization of the exciting light. Their 1963 paper describes in detail the case by case analysis for diatomic molecules. When dealing with a diatomic dissociation are

four cases to consider, since the transition dipole moment **μ** can either be parallel or perpendicular to the molecular axis, and the recoil velocity **v** can either be in the direction of the molecular axis or perpendicular to it (quantities in boldface denote vector quantities).

The orientation of the transition dipole moment of the molecule of interest can be identified from the symmetry properties of the initial and final molecular states. Zare and Herschbach[18] enumerated the possible transitions, and showed that the allowed $\Sigma \rightarrow \Sigma$, $\Pi \rightarrow \Pi$, and $\Delta \rightarrow \Delta$ transitions are parallel orientation, and that $\Sigma \rightarrow \Pi$ and $\Pi \rightarrow \Delta$ transitions are perpendicular orientation of **μ**. For a diatomic molecule, with the polarization of the electric field **ε** set along the Z-axis, the angular distributions $I(\theta)$ for the four cases all have the form of a characteristic dipole interaction, $1 + aP_2(\cos\theta)$, where P_2 is the second Legendre polynomial. With **ε** polarized in the Z-direction, one limiting case of $I(\theta)$ is in the case of axial recoil, recoil along the molecular axis, when the transition dipole moment is parallel, leading to $I(\theta) = 1 + 2P_2(\cos\theta)$. The other limiting case is for transverse recoil, recoil perpendicular to the molecular axis, when **μ** is parallel, or similarly for axial recoil when **μ** is perpendicular. This leads to $I(\theta) = 1 - P_2(\cos\theta)$, where the angle θ is the ordinary polar coordinate that along with φ relate the z coordinate to the Z-axis relative to the XY plane in the laboratory frame. The expression is then normalized over the solid angle and reduced to a more general form:

$$I(\theta) = \frac{1}{4\pi} [\ 1 + \beta\ P_2\ (\cos\ \theta)\ ] \qquad (\ -1 \leq \beta \leq 2\ )$$

where $P_2(\cos\theta) = \frac{1}{2}(3\cos^2\theta - 1)$, and β is defined as the anisotropy parameter. This expression for $I(\theta)$ is most effective when the timescale of dissociation is much faster than the rotational period of the parent molecule. Reactions where dissociation lifetimes are on the scale of or

longer than the rotational period will have measured angular distributions that can be artificially isotropic. The anisotropy parameter can be expressed as an average over the distribution of an angle γ, which is defined as the angle between **μ** and **v**:

$$\beta = 2 \langle P_2(\cos \gamma) \rangle$$

As γ increases from 0 to $\pi/2$, β decreases from 2 to -1. Reaffirming what was seen in the limiting cases for diatomics, $\beta = 2$ describes the transition where **μ** is parallel to **v**, and $\beta = -1$ describes the transition where **μ** is perpendicular to **v**. A value of $\beta = 0$ describes a completely isotropic angular distribution of products.

The above expression for the angular distribution $I(\theta)$ is most accurate when there is no alignment in the sample, which holds true for many cases of molecules in molecular beams. However in the case of a multistep photodissociation process using linearly polarized laser sources, it is possible for the first laser in the sequence to excite the molecule to a state that has an aligned vector for the rotational angular momentum. If the molecule dissociates on a shorter timescale than the timescale required for the molecule to depolarize, a different expression should be used to fit the angular distribution data.[19] The proper function for data where some alignment is suspected is:

$$I(\theta) = \frac{1}{4\pi} [\, 1 + \beta_2 P_2 (\cos \theta) + \beta_4 P_4 (\cos \theta) \,] \qquad (-1 \leq \beta_2, \beta_4 \leq 2)$$

where β_2 and β_4 are the anisotropy parameters and $P_4(\cos \theta) = \frac{1}{8}(35\cos^4\theta - 30\cos^2\theta + 3)$. If a fit of the angular distribution data yield a value of zero for β_4, then there was no alignment of the angular momentum vector in the sample.

1.5 Hund's cases

When considering the rotational-vibrational energy levels and wavefunctions of diatomic molecules, it is necessary to consider the couplings between the different angular momenta present in the molecule. Hund's cases (a) – (d) describe circumstances where certain couplings dominate over others. Most diatomic systems can be classified as closely following one or a mixture of Hund's cases. Cases (a), (b), and (d) are of particular relevance to the work on nitric oxide by Houston and coworkers.[19]

In the Hund's case (a) coupling scheme, the electronic orbital angular momentum **L** and the electronic spin angular momentum **S** are both tied to the internuclear axis, while the nuclear rotational angular momentum **R** is at right angles to the internuclear axis. The total angular momentum **J** is the vector sum of **R** and Ω, which is the sum of Λ and Σ, which are the projections of **L** and **S** respectively on the internuclear axis, and **J** makes a projection M (or M_J) on the space-fixed Z-axis as shown by Figure 1.5.[20]

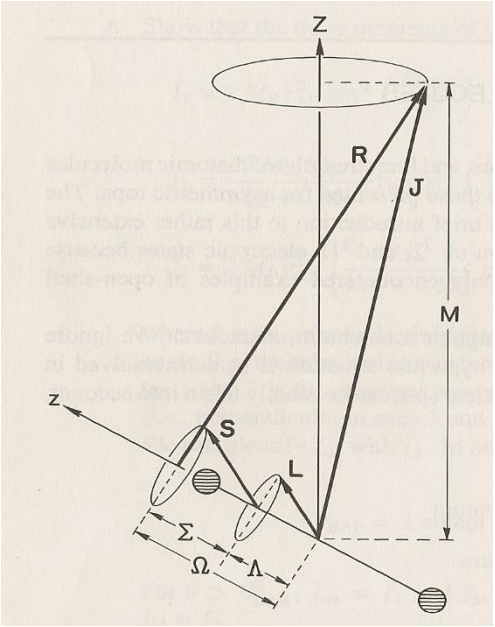

Figure 1.5. Vector diagram for Hund's case (a) coupling.

In the simplest limit, the rotational Hamiltonian is $H_{rot} = B(r)\mathbf{R}^2$, where B(r) is the rotational constant, and $\mathbf{R} = \mathbf{N} - \mathbf{L}$, where **N** is the total angular momentum excluding electronic spin, or equivalently $\mathbf{N} = \mathbf{J} - \mathbf{S}$. For diatomics with one electron in the highest occupied molecular orbital, additional terms must be considered. In a $^2\Sigma$ state ($S = ½$ and $\Lambda = 0$), a spin-rotation coupling term $\gamma(r)\mathbf{N} \cdot \mathbf{S} = \gamma(r)\ (\mathbf{J} - \mathbf{S}) \cdot \mathbf{S}$ must be included. The rotational Hamiltonian then becomes $H_{rot} = B(r)\mathbf{R}^2 + \gamma(r)\ (\mathbf{J} - \mathbf{S}) \cdot \mathbf{S}$, and the energies become $E = B_vN(N + 1) + ½\gamma_vN$ where $J = N + ½$ and $E = B_vN(N + 1) - ½\gamma_v(N + 1)$ where $J = N - ½$. In a $^2\Pi$ state ($S = ½$ and $\Lambda = \pm1$), a spin-orbit interaction term must be included, which is approximated as $H_{SO} = A(r)\mathbf{L} \cdot \mathbf{S}$. The energies are then $E = B_v\{(J - ½)(J + 3/2) \pm ½[4(J + ½)^2 + Y(Y - 4)]^{1/2}\}$ where $J = N \pm ½$ and Y is defined as the ratio of A_v/B_v.[20]

With increasing rotation, the **N** · **S** coupling term begins to dominate the rotational part of the Hamiltonian when compared to the **L** · **S** spin-orbit coupling term. In this case, **S** uncouples from the internuclear axis and recouples to **N**, which is referred to as Hund's case (b). The total angular momentum **J** is now a vector sum of **N** and **S**, as is shown in Figure 1.6.

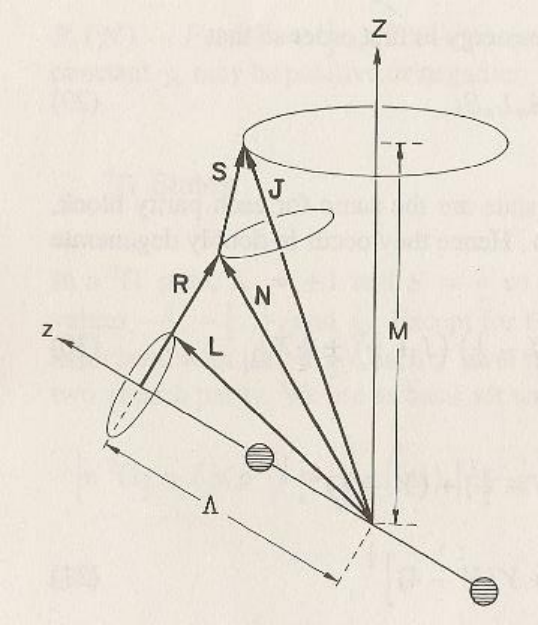

Figure 1.6. Vector diagram for Hund's case (b) coupling.

The wavefunctions for the energy levels J = N + ½ and J = N – ½ (often referred to as F1 and F2 respectively) become equally weighted linear combinations of the case (a) wavefunctions.[20]

Hund's case (c) coupling is commonly seen in diatomics with heavy nuclei, where the spin-orbit interaction becomes very large and the coupling between **L** and **S** becomes stronger than the electrostatic interaction between **L** and the internuclear axis. Hund's case (d) describes

the opposite extreme, where the interaction between **L** and **R** is so strong that **L** uncouples from the internuclear axis and recouples to **R**, as shown in Figure 1.7.

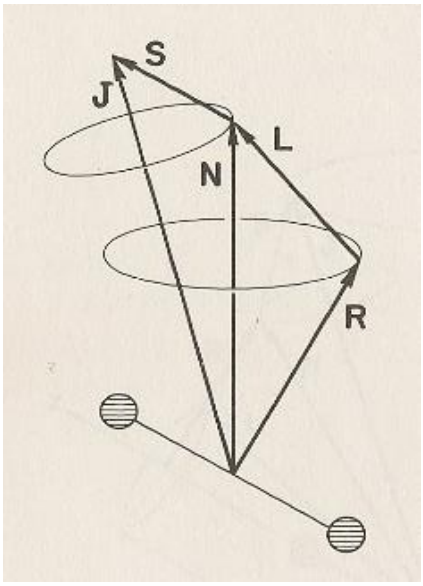

Figure 1.7. Vector diagram for Hund's case (d) coupling.

In the limit of very large rotation, such as the case of Rydberg's where the Rydberg electron only weakly interacts with the molecular core, Hund's case (d) is a limiting case of Hund's case (b). Figures 1.5-1.7 were reproduced with permission from reference 20.

1.6 Background on NO

The Rydberg series of nitric oxide have been a subject of interest for quite some time, however until more recently, there had been few studies of the angular distribution of the products of NO dissociation through Rydberg states.

1.6.1 Rydberg States

Rydberg states of atoms and molecules are (often highly) electronically excited states whose spectroscopic assignment follow the Rydberg formula, which was proposed by Johannes Rydberg in the late nineteenth century. The formula for a hydrogen-like element is:

$$\frac{1}{\lambda_{\mathrm{vac}}} = RZ^2\left(\frac{1}{n_1^2} - \frac{1}{n_2^2}\right)$$

where R is the Rydberg constant, Z is the atomic number of the element, and n_1 and n_2 are principle quantum numbers such that $n_1 > n_2$. Rydberg molecules are generally not one electron systems themselves, however the Rydberg electron in the molecule can be excited to such an energy where its behavior is similar to that of an electron interacting with an ionic core. Typically the excitation energy of the Rydberg electron approaches an ionization limit of the molecule, with many Rydberg states converging as the ionization potential is reached. If there

are more than one stable mono-cationic forms of the molecular ion, several Rydberg series are possible.

While the principle of the Rydberg formula can apply to Rydberg states of molecules, factors not encountered in the hydrogen-like formula must be considered. For Rydberg molecules, especially those where the Rydberg electron has low *n* or a low value of the orbital angular momentum, the quantum defect parameter, δ_l, becomes important. The quantum defect is a measure of the penetration of the Rydberg electron into the region of the electron distribution of the ion-like core, and represents a phase shift in the radial portion of the Rydberg electron wavefunction relative to its hydrogenic form.[21] In the limiting case where there is essentially no interaction between the Rydberg electron and the ionic core, such as in Hund's coupling case (d), the energy can be approximated as the sum of the core energy and the energy of the Rydberg electron. The equation is:

$$E(v^+, N^+, \ldots, n, l, m_l) = I(v^+, N^+, \ldots) + \frac{R}{(n - \delta_l)^2}$$
$$I(v^+, N^+, \ldots) = I_0 + E(v^+, N^+, \ldots)$$

where I_0 is the adiabatic ionization energy, and $E(v^+, N^+, \ldots)$ is the ionic core rotational-vibrational energy. However since most systems are not pure representations of Hund's case (d), it is necessary to consider some electrostatic coupling between the Rydberg electron's angular momentum with the core's rotational angular momentum, which approaches Hund's case (b). In Hund's case (b), v^+ and N^+ are no longer good quantum numbers, however the projection of the Rydberg electron's angular momentum onto the internuclear axis becomes well defined, and Λ

or λ becomes a good quantum number. In the limit of case (b) coupling, the energy expression is now approximated as:

$$E = I_0 - \frac{R}{(n - \delta_{l\lambda})^2} + E_v + B_{vl\lambda}[J(J+1) - \lambda^2].$$

Note that the coupling results in a series of rotational energy levels built on each vibronic level associated with *v*, *l*, and λ.[21] For states where the Rydberg electron has low values of *n* and/or *l*, Hund's case (b) coupling is a better estimation, where states with higher *n* tend to have more Hund's case (d) character.

1.6.2 Spectroscopy of NO

Early work by Miescher and coworkers[22,23] used absorption spectroscopy of cold NO to establish an "atlas" of the energetic requirements to access many Rydberg series in the region of the first three (v = 0, 1, 2) ionization limits of NO. Soon after, Zakheim and Johnson[24] examined the multiphoton ionization spectrum of NO cooled by supersonic expansion. They proposed that since the ground state electronic structure of NO consists of a single loosely bound electron outside of a filled core, the excited states leading up to the first ionization potential should be Rydberg-like states, where the weakly bound electron is in an atomic-like orbital. With the highest occupied orbital in ground state NO acting much like a *d* orbital, atomic-like selection rules should apply, and single photon excitation would predominantly result in

excitation to *p* or *f* type Rydberg states. Even though this was not the case for all of the states observed, their examination of predissociation from various Rydberg states was noteworthy.

Anezaki et. al.[25] used two-color multiphoton ionization to examine the Rdyberg states above the ionization threshold of NO, and fluorescence dip spectroscopy to examine those below the threshold. All Rydberg levels were accessed via the $A\ ^2\Sigma^+$ intermediate state, which has a mixed configuration of 3*s*σ with 5% *d* and a small amount of *p* character. Only *ns*, *np*, and *nf* Rydberg states of NO were observed from this excitation scheme. While the $A\ ^2\Sigma^+$ (3*s*) state belongs to Hund's coupling case (b), it was observed that Rydberg states with higher principle quantum number mixed in more and more case (d) coupling as *n* increased. They proposed that the molecular wavefunctions in this scenario could be expressed by a linear combination of the basis set of case (b), where the coefficients would be variation parameters. For the *f* complex, the rotational structure of the observed spectra showed the branches increasing in energy separation as N increased, which indicates an intermediate case between cases (b) and (d). The rotational energies of the *A* state (case (b)) are given by BN"(N" + 1) while the energies of pure case (d) are given by BR'(R' + 1), and the branches occur by the selection rule R' – N" = 0, ±2. The numerical energies can be obtained by matrix diagonalization and fit to the form

$T_\Lambda^{ev} = T_\Sigma^{ev} + C\Lambda^2$, where T_Λ^{ev} are the pure Hund's case (b) energies, and C is the energy splitting of the vibronic sublevels. The degree of case (d) coupling can be evaluated by the ratio of C to the rotational constant, with C = 0 meaning the sublevels are completely degenerate, indicating pure case (d). For the *p* complex, the spectra showed some resolution of the vibronic sublevels for moderate values of *n*, which again indicates an intermediate between cases (b) and (d), and resulted in the selection rule R' – N" = 0. For lower values of *n*, more case (b) behavior

in the spectra was evident. For the *s* complex, there is no orbital angular momentum and the difference between Hund's case (b) and (d) disappears, and the rotational energy is given by the expression $E = T^{ev} + BN(N + 1)$.

The ability to express Hund's case (d) wavefunctions as linear combinations of case (b) wavefunctions[25], and thus case (a) wavefunctions[20] is important when predicting the angular distribution of the products of dissociation from excitation to Rydberg states. Consider a state $|J\ M\rangle$, where **J** precesses uniformly about, and makes a projection *M* onto, the Z axis. The probability of finding **J** making a projection *M*' onto a new axis called Z', which shares an origin with the Z axis but is rotated by an angle θ is:

$$| D^{J}_{M',M} (\varphi, \theta, \chi) |^2 = [\ d^{J}_{M',M} (\theta)\ ]^2$$

where the two Euler angles φ and χ represent azimuthal rotation about the old and new Z axes and play no role in the probability interpretation.[20] Figure 1.8 displays the vector model picture for this rotation.

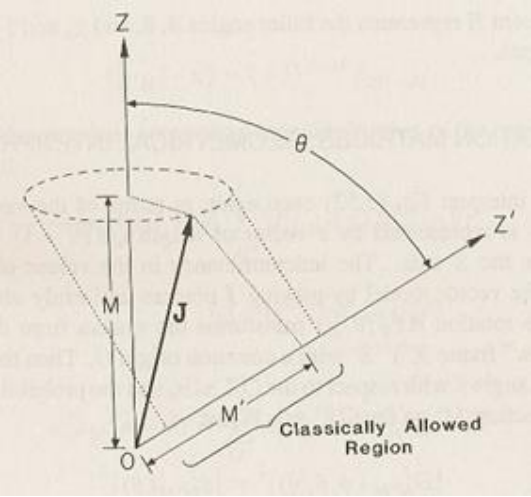

Figure 1.8. Vector model picture for the rotation of the state function $|J\ M\rangle$ from Z to Z' by the angle θ.

When recalling Figure 1.5 which shows the vector diagram for Hund's coupling case (a), one will note that **J** makes a projection *M* onto the Z axis, and also makes a projection Ω onto the internuclear axis, also called the z axis. Comparing to Figure 1.8, with Ω analogous to *M*' and the internuclear axis analogous to the Z' axis, it is possible to relate the Z and internuclear axes by the angle θ. Thus the ability to express Hund's case (b) and (d) wavefunctions, and the intermediate cases, in terms of the case (a) wavefunctions allows for the determination of the two projections of **J**. In the limit of axial recoil of the products of photodissociation (which is the case for NO), it is then possible to predict the angular distribution of the products for the above mentioned coupling cases. Figure 1.8 was reproduced with permission from reference 20.

Expanding somewhat on the work by Anezaki et. al., Geng et. al.[26] used two-color resonant four wave mixing spectroscopy to obtain the spectra of the *ns*, *np*, and *nf* Rydberg series

of NO, with *n* both above and below the first ionization potential. Rydberg states were accessed via the ($A\ ^2\Sigma^+$, v =0, N = 2, J = 1.5) ← ($X\ ^2\Pi$, v = 0, N = 1, J = 0.5) transition, as opposed to the work by Anezaki et. al. where most of the Rydberg states observed were accessed via an $A\ ^2\Sigma^+$, v =1 state. For the *ns* states, they reaffirm pure Hund's case (b) coupling due to the lack of orbital angular momentum of the Rydberg electron, and the rotational energies are E = T + BN(N + 1), where T is the term value and B is the rotational constant, as before. Similarly for the *nf* states, they reaffirm the intermediate case between (b) and (d), and were able to reproduce the selection rules and calculations of the parameter C by Anezaki et. al.[25] The authors note that in contrast to the relatively sharp transition lines found in the *ns* and *nf* spectra for NO, there are some broad features present in the *np* spectra. These diffuse features are likely due to fast predissociation. In pure Hund's case (b), the *np* complex consists of three states: *np* $^2\Pi^+$, *np* $^2\Pi^-$, and *np* $^2\Sigma^+$. The *np* $^2\Pi^+$ and *np* $^2\Pi^-$ states can interact with valence states $B\ ^2\Pi$ and/or $L\ ^2\Pi$, which both converge to the N(^{2}D) + O(^{3}P) dissociation limit. Figure 1.9 shows several pertinent potential energy curves and the positions of the various dissociating limits for NO.[27] This interaction between the *np* $^2\Pi^+$, *np* $^2\Pi^-$ states above the dissociation limit, and the $B\ ^2\Pi$, $L\ ^2\Pi$ states, is responsible for the fast predissociation and thus the broad features present in the *np* spectra.

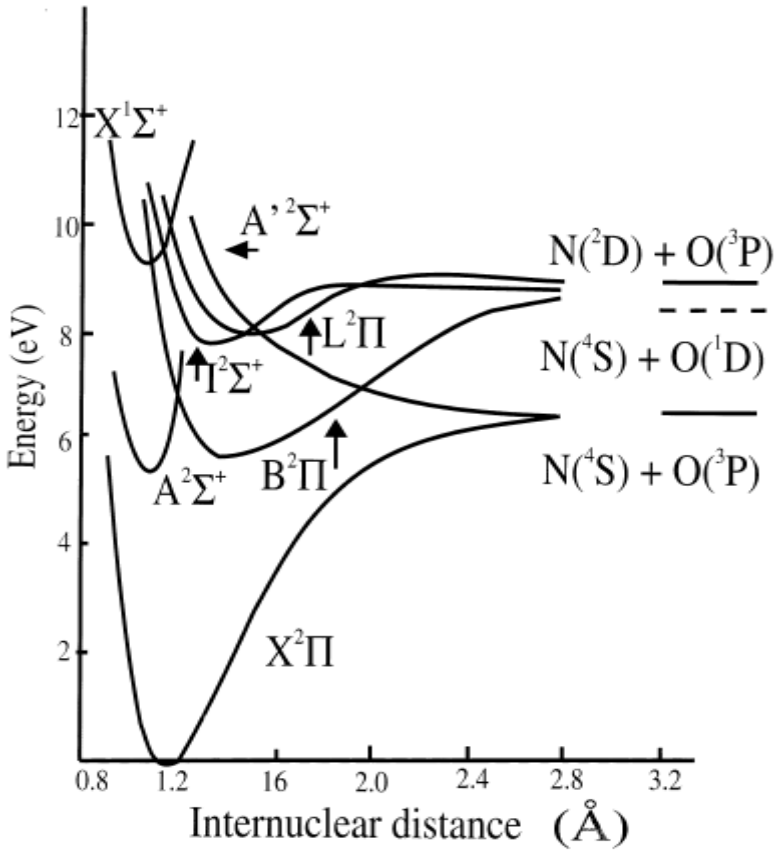

Figure 1.9. Potential energy curves for NO, showing the positions of the dissociation limits and of the valence curves correlating with them.[27]

Bakker et. al.[27] performed some of the first experiments that investigated the angular distribution of products from NO dissociation. N^+ was imaged from the $N(^2D) + O(^3P)$ channel, and O^+ was imaged from both the $N(^2D) + O(^3P)$ and $N(^4S) + O(^3P)$ channels. Angular distributions of the products are reported, and the alignment of products when fitting to the β parameters is discussed. It was found that fitting the angular distribution data using β_2 and β_4 did not provide a significant improvement over fitting with only β_2, meaning there was little alignment caused by the pump laser. The laser promoting the *A* – *X* transition was set to a

different bandhead than the one used by Geng et. al.[26] and Houston and coworkers,[19] which causes some disparity in the findings upon comparison. A more detailed analysis of this comparison is forthcoming in the subsequent chapter.

Finally, experiments by Cosofret, Lambert, and Houston[28] examined several Rydberg states of jet-cooled NO, taking velocity mapped images of O^+ from the $N(^2D) + O(^3P)$ channel. A theoretical approach for calculating the angular distributions of photoproducts from two photon excitation of NO to Rydberg levels is presented, beginning with a one photon excitation of Hund's case (a) states, expanding that to two photon excitation of case (a) states, and then modifying the result to apply to two photon excitation of Hund's case (b) states. The calculated angular distributions aided in assigning peaks in the ionization spectra of various Rydberg bands in NO. Also the angular distribution data, along with the presence or absence of peaks or branches in the ionization spectra of the investigated Rydberg bands, allowed for the determination of the character of the intermediate state in the two photon excitation scheme.

1.7 References

[1]G. Porter, *Proc. R. Soc. London, Ser. A* **9**, 60 (1950).

[2]R. W. Diesen, J. C. Wahr, and S. E. Adler, *J. Chem. Phys.* **50**, 3635 (1969).

[3]S. J. Riley and K. R. Wilson, *Faraday Discuss. Chem. Soc.* **53**, 132 (1972).

[4]W. C. Wiley and I. H. McLaren, *Re. Sci. Instrum.* **26**, 1150 (1955).

[5]A. Kantrowitz and J. Grey, *Rev. Sci. Instrum.* **22**, 328 (1951).

[6]J. B. Anderson and J. B. Fenn, *Phys. Fluids* **8**, 780 (1965).

[7]M. N. R. Ashfold, N. H. Nahler, A. J. Orr-Ewing, O. P. J. Vieuxmaire, R. L. Toomes, T. N. Kitsopoulos, I. A. Garcia, D. A. Chestakov, S. Wu, and D. H. Parker, *Phys. Chem. Chem. Phys.* **8**, 26 (2006).

[8]A. Schultz, H. W. Cruse, and R. N. Zare, *J. Chem. Phys.* **57**, 1354 (1972).

[9]M. N. R. Ashfold and J. D. Howe, *Annu. Rev. Phys. Chem.* **45**, 57 (1994).

[10]D. W. Chandler and P. L. Houston, *J. Chem. Phys.* **87**, 1445 (1987).

[11]D. Townsend, M. P. Minitti, and A. G. Suits, *Rev. Sci. Instrum.* **74**, 2530 (2003).

[12]A. T. J. B. Eppink and D. H. Parker, *Rev. Sci. Instrum.* **68**, 3477 (1997).

[13]D. A. Dahl, J. E. Delmore, and A. D. Appelhans, *Rev. Sci. Instrum.* **61**, 607 (1990).

[14]H. L Offerhaus, C. Nicole, F. Lepine, C. Bordas, F. Rosca-Pruna, and M. J. J. Vrakking, *Rev. Sci. Instrum.* **72**, 3245 (2001).

[15]B. Chang, R. C. Hoetzlein, J. A. Mueller, J. D. Geiser, and P. L. Houston, *Rev. Sci. Instrum.* **69**, 1665 (1998).

[16]V. Dribinski, A. Ossadtchi, V. A. Mandelshtam, and H. Reisler, *Rev. Sci. Instrum.* **73**, 2634 (2002).

[17]G. A. Garcia, L. Nahon, and I. Powis, *Rev. Sci. Instrum.* **75**, 4989 (2004).

[18]R. N. Zare and D. R. Herschbach, *Proc. IEEE* **51**, 173 (1963).

[19]J. Chen, B. R. Strangfeld, and P. L. Houston, *J. Chem. Phys.* **140**, 034315 (2014).

[20]R. N. Zare, *Angular Momentum: Understanding Spatial Aspects in Chemistry and Physics*, John Wiley & Sons Inc. (1988).

[21]T. P. Softley, *Int. Rev. Phys. Chem.* **23**, 1 (2004).

[22]E. Miescher and F. Alberti, *J. Phys. Chem. Ref. Data* **5**, 309 (1976).

[23]E. Miescher and K. P. Huber, *Int. Rev. Sci. Phys. Chem. (Series 2)* **3**, 37 (1976).

[24]D. Zakheim and P. Johnson, *J. Chem. Phys.* **68**, 3644 (1978).

[25]Y. Anezaki, T. Ebata, N. Mikami, and M. Ito, *Chem. Phys.* **97**, 153 (1985).

[26]J. Geng, T. Kobayashi, and M. Takami, *Chem. Phys. Lett.* **266**, 290 (1997).

[27]B. L. G. Bakker, A. T. J. B. Eppink, D. H. Parker, M. L. Costen, G. Hancock, and G. A. D. Ritchie, *Chem. Phys. Lett.* **283**, 319 (1998).

[28]B. R. Cosofret, H. M. Lambert, and P. L. Houston, *J. Chem. Phys.* **117**, 8787 (2002).

Chapter 2

2. NO Dissociation through *ns*, *np*, and *nf* Rydberg States: Angular Distributions

Velocity-mapped imaging and theoretical calculations have been used to study the angular distribution of the products of NO predissociation following its excitation to the *11s*, *10p*, *11p* and *9f* Rydberg levels based on the NO^+ ($X\ ^2\Sigma^+$) core. The Rydberg states were reached from the NO ($A\ ^2\Sigma^+$, v =0, N = 2, J = 1.5) level prepared with strong alignment by excitation with linear polarization from NO ($X\ ^2\Pi$, v = 0, N = 1, J = 0.5). Ion dip spectra of the Rydberg states were recorded along with velocity-mapped images at the major peaks. The results are compared to calculations based on a previous theoretical approach modified to include transitions to states of Hund's case (d) coupling. The reasonable agreement shows the predictive value of the theory. The theory has also been used to reassess and explain previous results and to understand variations in the rate of photodissociation with components of the *10p* and *11p* Rydberg states.

2.1 Introduction

The use of multiphoton excitation techniques has made it possible to examine in detail the Rydberg states of a great number of molecules, leading in many cases to a better understanding of their structure, spectroscopy, and behavior. The nitric oxide molecule in particular has been an interesting test case.[1-13] Of special note is the early work by Meischer, Jungen, Fredin, Gauyacq and others. Jungen and Meischer first reported observation of the first

two bands of the *nf* Rydberg series of NO and analyzed their rotational structure.[1] Meischer and Huber subsequently published a review article on the electron spectroscopy of the NO molecule focusing on the Rydberg structure.[2] The *s* and *d* Rydberg series of NO were later analyzed by Fredin *et al.*,[3] and these bands were important to the development of multichannel quantum defect analysis. Raoult et al. continued the investigation of *nf* and *np* Rydberg states by studying their linear Zeeman effect, again using a multichannnel quantum defect approach for the analysis. Following these pioneering studies, Anezaki et al.[6] investigated the spectroscopy of the *n*s, *np*, and *nf* Rydberg states built on the NO^+ ($X\ ^2\Sigma^+$) core using fluorescence dip spectroscopy in a supersonic free jet. This work was followed by further spectroscopic study[7] as well as investigations into the dissociation dynamics.[8,9] Geng et al.[10,11] and Kobayashi et al.[13] provided further spectroscopic detail using two-color four-wave mixing spectroscopy. It appears that the only report of the angular and velocity distribution of the N + O products followed the investigation by Bakker et al.,[12] who used velocity mapped imaging to monitor the $O(^3P)$ and $N(^2D)$ products produced in the multiphoton dissociation of NO using light at 226 and 355 nm. The angular distribution of photoproducts as a function of excitation frequency, rotational constant and level, and lifetime has been discussed by Kim et al.[14] The theory they present applies to any dissociating molecule whose states can be described as behaving as a mixture of Hund's case (a) and (b). While for NO the coupling in the ground state is close to Hund's case (a) and in the first excited state is close to Hund's case (b), the coupling in the Rydberg states for the *np* and *nf* levels is most closely described by a mixture of Hund's case (b) and (d). One purpose of the investigation reported here was to extend and test the theory to Hund's case (d)

molecules. A second objective was to improve our understanding of the interaction between the Rydberg levels and the dissociative levels leading to products.

2.2 Experiment

The experiment is carried out in a stainless steel reaction chamber where the interaction region of the chamber is kept at ~1 x 10^{-7} Torr while the supersonic jet system is running. The molecular beam is generated when a gas mixture of 1:5 NO (Matheson, Chemically Pure) to He (Matheson, Ultra High Purity) with a backing pressure of 2 psi above atmosphere passes through a 0.5 mm diameter aperture, pulsed jet nozzle into a source chamber of pressure ~2 x 10^{-5} Torr. The pulsed molecular beam then travels through a 0.5 mm diameter skimmer located 1 cm downstream from the nozzle. Source and interaction chamber pressures are maintained using a Varian TV2K-G turbo pump, and an Oerlikon 1000C Turbovac turbo pump, respectively. Varian SD-700 mechanical pumps back both turbo pumps.

To achieve the desired excitation scheme, the first of the two pump lasers must be set to the transition energy for the $A\ (^2\Sigma^+)$ (v' = 0, N' = 2, J' = 1.5) $\leftarrow$ $X\ (^2\Pi_{1/2})$ (v" = 0, N" = 1, J" = 0.5) transition of NO, which is approximately at λ_1 = 226.1 nm. Laser pulses at this wavelength are generated when the third harmonic of a Spectra Physics DCR-3 neodymium:yttrium aluminum garnet (Nd:YAG) laser pumps a PDL-1 dye laser using Coumarin 450. The fundamental output of the dye laser is then doubled using an Inrad Autotracker. The doubled light at wavelength λ_1 then passes through two neutral density filters to reduce the energy per pulse to about 10 μJ. The second pump laser operates in the λ_2 = 335-355 nm range. The

second harmonic of a Spectra Physics GCR-200 Nd:YAG laser pumps a Lambda Physik SCANmate dye laser, using LDS 698 (Exciton dyes), which is then doubled to provide output at wavelength λ_2.

The locations of the various Rydberg transitions are determined using a type of dip spectroscopy with λ_1 and λ_2. Two photons of λ_1 have sufficient energy to ionize NO to NO^+. However, when λ_2 is scanned to the appropriate wavelength such that the energy corresponding to λ_1 and λ_2 is equal to the energy of a Rydberg state, some population of NO in the *A* state is excited to the Rydberg rather than being ionized, and the NO^+ signal is reduced.

Once the λ_2 values for the various Rydberg states were determined, the $N(^2D_{3/2})$ photofragment is probed by three-photon ionization near 268.9 nm via the $3p\ ^2S_{1/2}$ state.[15] The sibling fragment is primarily $O(^3P_2)$. Probe laser pulses are generated when the third harmonic of a Spectra Physics GCR-270 Nd:YAG laser pumps a Lambda Physik SCANmate OPPO using Coumarin 540. All frequency doubling is done using BBO (beta barium borate) crystals, with the desired doubled light λ_1, λ_2, and λ_{probe} being separated from the fundamental dye and Nd:YAG frequencies using a set of four Pellin-Broca prisms.

All three lasers were polarized in the same direction, which is the vertical direction in the image to be described below. The polarization of the third harmonic of the DCR-3, the second harmonic of the GCR-200, and the third harmonic of the GCR-270 are all vertical, since the respective dye lasers require the input polarization to be vertical. The output polarization of the PDL-1, the Scanmate, and the Scanmate OPPO dye lasers are all horizontal. In the case of the output of PDL-1 and the Scanmate, which are identified as pump lasers 1 and 2 above, the polarization is changed from horizontal to vertical using a pair of rotating polarizers. The

outputs from these polarizers then are propagated by right angle prisms and, in the case of laser 1, one dichroic mirror set at 45 degrees, maintaining vertical polarization. For the output of the Scanmate OPPO, called laser 3 or the probe laser above, we used two setups depending on whether horizontal or vertical polarization is needed. In the case of horizontal polarization, 3 right angle prisms propagate the horizontal output from the Scanmate OPPO into the interaction region of the chamber. When we require the probe to be vertically polarized, a set of two right angle prisms are placed at the output of the Scanmate OPPO, one prism located vertically with respect to the other. The propagation of horizontally polarized light through the two right angle prisms in this configuration changes the polarization to vertical, and then one additional right angle prism propagates the resulting light into the chamber. Finally, all output polarizations were verified using a "stack of plates" polarizer.

The polarization of the probe laser made essentially no difference to the measured angular distributions. We at first measured the angular distributions of the $O(^3P)$ product using 226 nm ionization. While there was too much interference from 266-nm excited NO to use this product reliably, we did observe that the $O(^3P_2)$ image was unchanged in switching the 226 nm polarization from vertical to horizontal. Similarly, we measured images for the $N(^2D_{3/2})$ in both polarizations for the $^2R_{-1}$ transition of the *9f* Ryberg level and for the R-branch transition of the *11s* Rydberg level; the small differences in β_2 and β_4 between vertical and horizontal probe polarization were well within our experimental error.

The two pump lasers are focused into the interaction region using a 25-cm lens, while the probe laser is focused using a 12-cm lens. The two pump laser beams counter-propagate with the probe laser beam across the output of the molecular beam nozzle and are spatially aligned for

maximum overlap in the molecular beam. The pump lasers excite the NO in the beam into one of the various Rydberg series, selected by choice of the wavelength λ_2. Following a 10 ns delay, the probe laser ionizes the $N(^2D_{3/2})$ photofragment. The energies are typically ~10 μJ per pulse for the first pump laser, ~2-3 mJ per pulse for the second pump laser, and ~0.5 mJ per pulse for the probe laser.

Velocity and angular distributions were measured using the velocity-mapped, product imaging technique.[16,17] The interaction region where the three lasers intersect the molecular beam is located between the first and second of a set of three circular, parallel, plate-like electrodes inside our interaction chamber. Voltages are applied to these first two plates causing the ions resulting from the experiment to be accelerated towards and through the center of the third plate, which is held at ground, and down a 30 cm field-free region towards a position-sensitive detection assembly. The ion "cloud" will expand while traversing this field-free region, allowing for better spatial separation of the products. The ratio of the charge on the first two plates is such that ions with similar velocities immediately after the photodissociation will arrive at a similar position on the detector.

The detector itself consists of a microchannel plate assembly with a fast phosphor attached. A PMT (Hamamatsu 1P21) monitors the phosphor output to determine the time of flight of the ions resulting from the reaction with respect to the time at which the lasers fire. By monitoring the PMT signal at the arrival time of the N mass, we can determine the signal-to-background level for various laser combinations. The two-laser background level measured with $\lambda_1 + \lambda_2$, $\lambda_1 + \lambda_{probe}$, or $\lambda_2 + \lambda_{probe}$ is at least 10 times smaller than the three-laser signal, and often the signal-to-background ratio is much better. Once the time of flight of the N^+ ions is known,

the MCP voltage is held constant at 1000 V until the ions of interest are due to arrive. Then, using a pulsed voltage generator (DEI, model GRK-3K-H), the voltage of the MCP is gated up to 1700-2000V for 150 ns, ensuring that only the ions of the proper mass are detected during the imaging experiment. A CCD camera records the position of each of the ion hits on the MCP/phosphor, and that data is transmitted to a computer running Labview 5.0. The position of the ion events relative to the center of the image reveals the velocity of the ions resulting from the experiment, and their distribution relative to the axis of linear polarization provides the degree of anisotropy, which gives information about the dynamics of the reaction. Images were analyzed using the BASEX program.[18]

2.3 Theory

Product angular distributions as a function of dissociation lifetime, excitation frequency, rotational level, and rotational constant have been discussed in detail previously,[14] but the method for their determination can be summarized in a few words. For a single transition with linear polarized light in a diatomic molecule from a state described by Hund's case (a) coupling to a similar state that subsequently dissociates in the axial recoil limit, the angular distribution is obtained from the square of a rotation matrix element. The simplicity of this relationship depends on the case (a) coupling, for which the rotation matrix element $d^{J}_{MJ,,\Omega}(\theta)$ gives the probability amplitude that, when the total rotation J makes a projection of Ω onto the molecular axis and a projection of M_J onto the axis of linear polarization, the molecular axis will make an

angle θ with respect to the light polarization axis. This relationship can be seen from the figures on pages 92 and 298 of reference 21.

The interesting variations occur when there are multiple pathways between the initial state and the state leading to dissociation along angle θ. A typical example is excitation via multiple rotational transitions, e.g., P- and R- branch transitions, or P-, Q-, and R-branch transitions. Then the probability amplitude for each pathway depends on a transition matrix element, given in Table I of reference 19, and on the overlap between the excitation wavelength and the absorption profile for that path. In analogy with light passing through multiple slits, the probability amplitude for each path is summed, the sum is multiplied by the appropriate rotation matrix element, and the result is then multiplied by its complex conjugate to obtain the overall probability. When the lines for each rotational transition are narrow compared to the spacing between them, then for a narrow laser linewidth principally one transition dominates at any given wavelength, so that each transition has a separate angular distribution. For a parallel transition, Zare calculated these probabilities as early as 1982.[20] When the rotational transitions are broadened, for example by rapid dissociation, then the absorption of even a narrow band laser line typically involves simultaneous excitation on all branches; the pathways then interfere with one another. In the extreme case of such broadening, the angular distribution at any absorbed wavelength is nearly the same, typically yielding $\beta_2 = 2$ for a parallel electronic transition and $\beta_2 = -1$ for a perpendicular one, where the angular distribution is given by $I(\theta) \propto 1 + \beta_2 P_2(\cos\theta)$. It is important to remember, however, that this conclusion holds only when the broadening is large compared to the rotational spacing, or, equivalently stated, when the dissociation lifetime is shorter than a rotational period.

Most electronic states are not pure Hund's case (a). However, other coupling cases can always be expanded in a basis of Hund's case (a) wavefunctions.[21,22] This expansion is useful because, as discussed above, the case (a) wavefunctions can easily be related to the angular distribution. For example, mixed case (a/b) coupling has been considered elsewhere,[21] and formulae expanding any mixed case (a/b) wavefunction into a sum of case (a) wavefunctions are available. The expansion coefficients depend on the on the ratio, A_{so}/B, of the spin-orbit coupling constant to the rotational constant. For dissociation through Rydberg states, it would be useful to expand mixed case (a/b)/(d) wavefunctions into case (a) coupling. Such an expansion can be accomplished as follows, using the method outlined by Anezaki et al.[6]

We expand the case (d) wavefunction as

$$| J, M, N_{ryd}, S, L_{ryd}, \ell, N^+ > = \sum_{\Lambda=L_{\min}}^{L_{\max}} d(N_{ryd}, N^+, \ell, \Lambda) | \Lambda, N, S, J, M >, \qquad [1]$$

where L_{min}, $L_{max} = -L_{ryd}, L_{ryd}$ if $N^+ \geq L_{ryd}$, and $L_{min}, L_{max} = -N^+, N^+$ otherwise. In this equation, N^+ is the rotation of the ion core, L_{ryd} is the angular momentum of the Rydberg electron, N_{ryd} is the vector sum of N^+ and L_{ryd}, and $\boldsymbol{\ell}$ is the projection of L_{ryd} onto the N^+ axis of rotation. $|\Lambda, N, S, J, M>$ is the case (a/b) wavefunction, and the coefficients $d(...)$ are to be determined. Of course, as noted above, the case (a/b) wavefunction can be expanded in case (a) as

$$| \Lambda, N, S, J, M >= \sum_{\Omega} \alpha_{\Omega} | J, M, \Omega >, \qquad [2]$$

where the coefficients α_{Ω} are the coefficients referred to above and found in ref. 21.

Combining these two equations and rearranging the order of summation, we have

$$| J, M, N_{ryd}, S, L_{ryd}, \ell, N^+ >= \sum_{\Omega} \sum_{\Lambda=L_{\min}}^{L_{\max}} d(N_{ryd}, N^+, \ell, \Lambda)\alpha_{\Omega} | J, M, \Omega > , \quad [3]$$

or

$$| J, M, N_{ryd}, S, L_{ryd}, \ell, N^+ >= \sum_{\Omega} aryd(\Omega) | J, M, \Omega > , \quad [4]$$

where

$$aryd(\Omega) = \sum_{\Lambda=L_{\min}}^{L_{\max}} d(N_{ryd}, N^+, \ell, \Lambda)\alpha_{\Omega} . \quad [5]$$

The coefficients *d*(...) are determined by diagonalization of the secular matrix. For the case of NO, this matrix is given for L_{ryd} = 1 or 3 by Anezaki et al.[6] Diagonalization provides eigenvalues giving the energies for each N_{ryd} or $\boldsymbol{\ell}$ state, as well as eigenvectors which are the elements *d*(...) providing for each eigenstate the fractional composition to the wavefunction of the basis states. In the case of L_{ryd} = 1, a closed form solution is straight-forward. The basis states in order of decreasing energy are the Σ^+, Π^-, and Π^+ states corresponding to $\boldsymbol{\ell}$ = -1, 0, 1, and the corresponding eigenvectors are $d(\boldsymbol{\ell} = -1) = [\ s^+ , 0, p^+]$, $d(\boldsymbol{\ell} = 0) = [\ 0 , 1, 0]$, and $d(\boldsymbol{\ell} = 1) = [\ s^-, 0, p^-]$, where

$$s^{\pm} = 1/((z^{\pm})^2 + 1)^{1/2}, \quad [6]$$

$$p^{\pm} = z^{\pm}/((z^{\pm})^2 + 1)^{1/2}, \quad [7]$$

and

$$z^{\pm} = -\frac{C - 2B_{ryd} \pm \sqrt{(2B_{ryd} - C)^2 + 4c^2}}{2c} . \quad [8]$$

In these equations B_{ryd} is the rotational constant for the ion core, $c = -2\ B_{ryd}\ (N_{ryd}\ (N_{ryd} + 1))^{1/2}$, and C describes the energy separation between the zero-order, case (b), states:[6]

$$T_{\Lambda}^{ev} = T_{\Sigma}^{ev} + C\Lambda^2 \quad . \qquad [9]$$

In the case of $L_{ryd} = 3$, it is more convenient to obtain the eigenvectors by numerical methods. The degree of case (d) coupling is determined by the ratio of C to B_{ryd}, with pure case (d) corresponding to $C/B_{ryd} = 0$. Values for C and B_{ryd} are tabulated by Anezaki et al.[6] for several n*p* and n*f* Rydberg states of NO, though mostly in v = 1. For $L_{ryd} = 0$, we have $\Lambda = 0$, so that there is no decoupling of Λ from the internuclear axis. Thus, n*s* Rydberg states can simply be treated in case (b) coupling.

The computer code described previously[14] was modified to handle case (d) coupling as described above and then used to predict the value of β_2 and β_4 as a function of wavelength, rotational constant and level, and lifetime broadening.

While this approach is sufficient for determining the spectra and angular distributions in straightforward cases, it is worth noting that Rydberg spectra can be quite complex. For example, interactions can couple states with different values of l (l-mixing), such as in the NO *s* and *d* Rydberg states for low values of n^*,[3] and the overall behavior can best be described by multichannel defect theory.

2.4 Results

Two types of experiment were performed. Ion dip spectra obtained by scanning λ_2 while monitoring the decrease in the NO^+ signal induced by λ_{probe} were recorded and compared to previous results.[6,11] For the most part, the spectra were similar except for small shifts of the whole spectrum due to a shift in wavelength calibration. In many cases, the spectra were weak, and two spectra were recorded, one using focused light for λ_2 and one using unfocused light. More and sharper features were detected in the focused case.

The second type of experiment was to fix wavelength λ_2 and use the velocity mapped imaging to detect the angular and speed distribution of the N^+ product. The angular distributions were analyzed using BASEX[18] and fit to the function $I(\theta)= 1 + \beta_2 P_2(\cos \theta) + \beta_4 P_4(\cos \theta)$. Calculations were performed under two different assumptions. In principle, excitation at wavelength λ_1 with a linearly polarized laser aligns the sample prior to its interaction with the pulse at λ_2. Thus, one assumption was that this alignment is present. A second assumption is that the alignment is completely degraded due, for example, to hyperfine depolarization. In this case, the wavelength λ_2 interacts with an isotropic sample in the selected state, NO ($A\ ^2\Sigma^+$, v' = 0, N' = 2). Issues of alignment by the polarization of λ_1 will be discussed below.

Figure 2.1 shows a representative image of the N^+ ion positions on the CCD screen. The distribution is not isotropic, and there is a strong ring indicating that that there is one predominant speed. This particular image is for the $^0Q_0$ transition to the $^2\Pi^-$ component of the 9f Rydberg level at an energy of the second laser pulse of 29168.8 cm^{-1}.

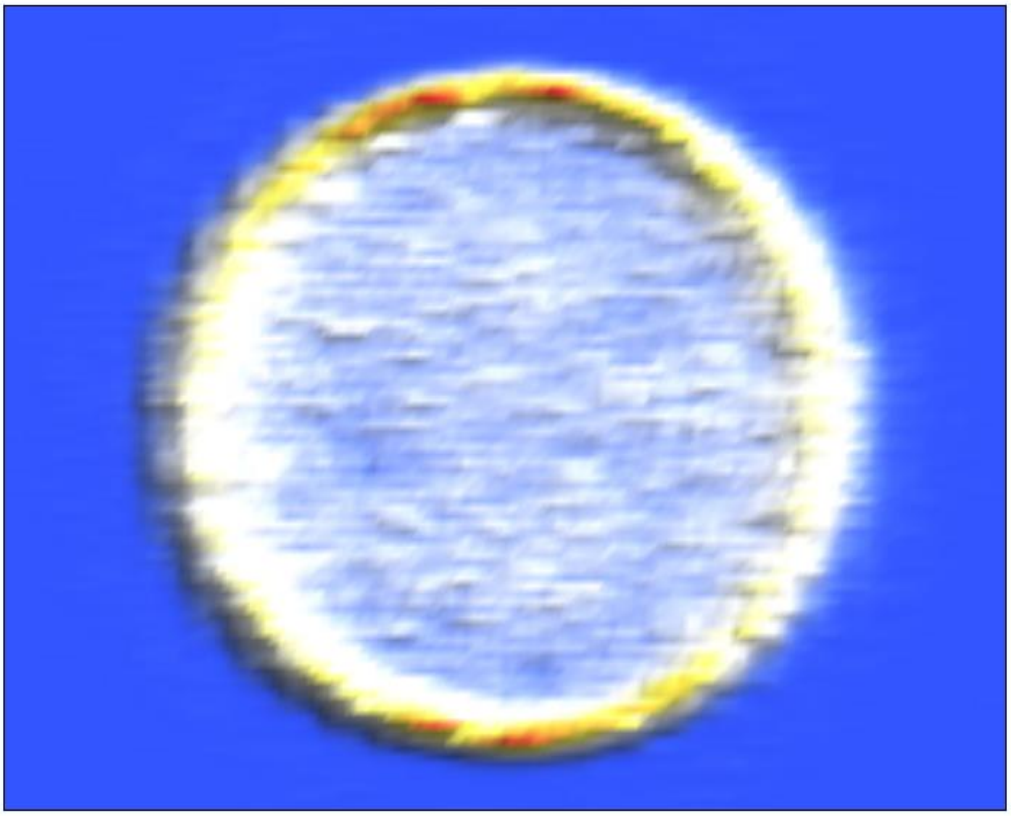

Figure 2.1. Velocity-mapped image of the N^+ produced following excitation of NO from the $A\ ^2\Sigma^+$, v = 0, N = 2, J = 1.5 level on the $^0Q_0$ transition to the $^2\Pi^-$ component of the 9f, v=0, Rydberg level at 29168.8 cm^{-1}.

Figure 2.2 shows the analysis of the data of Fig. 2.1 using the BASEX computer code. Given the dissociation energy and the heat of formation of NO, and the dissociation energies for N_2 and O_2, one can calculate that the N velocity should be1.05 km/s for N($^2D_{3/2}$) detected in coincidence with O($^3P_2$) at the wavelengths used. The speed distribution in the top panel shows a prominent peak at 43 pixels, in rough agreement with this calculation using previous values for pixel-to-velocity calibration. While this value can be used as a calibration of the speed per pixel

ratio, the angular distribution is unaffected by the choice as long as it is taken at the peak of the speed distribution. The angular distribution in the bottom panel shows that a function of the form $1 + \beta_2 P_2(\cos\theta) + \beta_4 P_4(\cos\theta)$ with $\beta_2 = 0.57$ and $\beta_4 = 0.22$ fits the variation of intensity with angle relative to the direction of linear polarization.

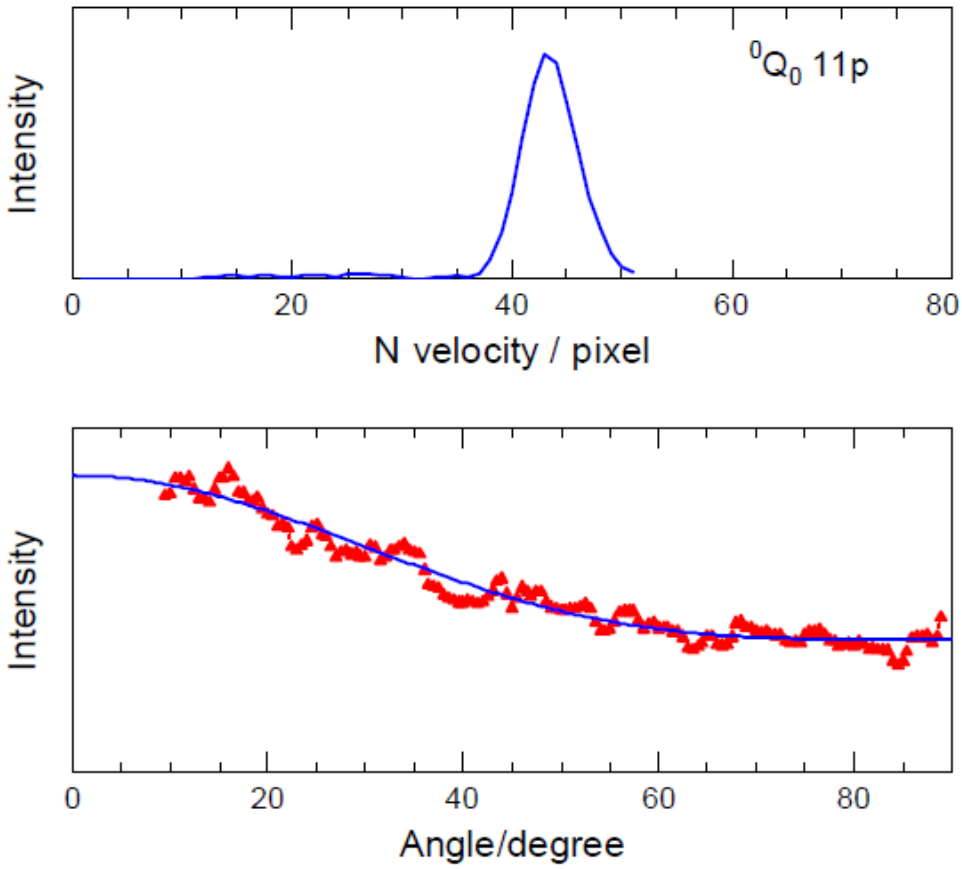

Figure 2.2. Analysis of the data from Fig. 2.1 using BASEX.[18] Top panel: speed distribution of the N^+, showing a prominent peak at 43 pixels, corresponding the the expected velocity of N. Bottom panel: angular distribution and fit of the function $I(\theta) \propto 1 + \beta_2 P_2(\cos\theta) + \beta_4 P_4(\cos\theta)$ to the data, with $\beta_2 = 0.57$ and $\beta_4 = 0.22$.

Results for experiment and theory are shown in Figs. 2.3 – 2.6 for the *11s*, *10p*, *11p*, and *9f* Rydberg states based on the NO^+ ($X\ ^2\Sigma^+$) core. The values of β_2 and β_4 are read on the right-hand ordinate, while the spectral intensities in arbitrary units are read on the left-hand ordinate. The solid red line gives β_2 for the aligned assumption, the dashed one for the isotropic assumption and the dot-dashed one for the saturated, aligned assumption. The value of β_4 is shown in green for the aligned assumption. For the isotropic assumption, the value of β_4 is zero. Measured spectra are in red, while calculated ones are in blue. The red triangles and green squares represent the respective values of β_2 and β_4 measured at a particular energy. The transition energies are given on the bottom axis, while the total energies relative to the NO ($X\ ^2\Pi_{1/2}$, $v = 0$, $J = 0.5$) level are given on the top axis. The uncertainties indicated in the plot were based both on a repeated measurement of the $^2R_{-1}$ line of the *9f* Rydberg transition and from an estimate of the results of the BASEX program, where the angular results are given for the peak in the velocity distribution, but different values would be obtained at points ±10% from the peak.

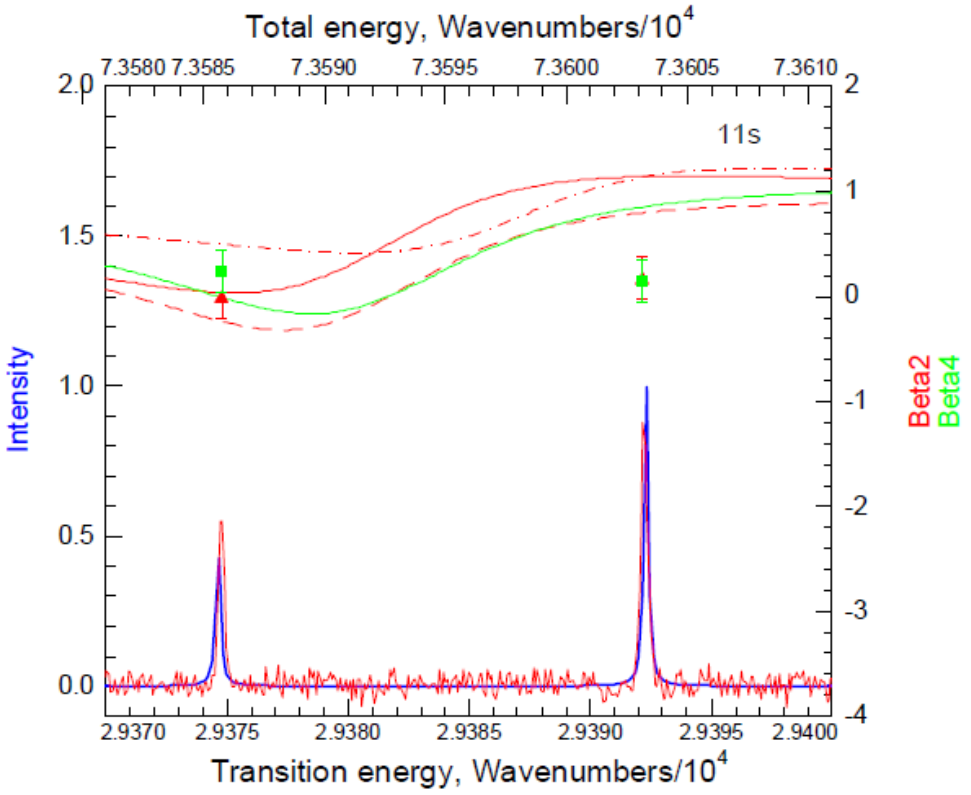

Figure 2.3. Experimental and theoretical results for the *11s* Rydberg state. The values of β_2 and β_4 are read on the right-hand ordinate from the red and green curves, respectively, while the spectral intensities in arbitrary units are read on the left-hand ordinate. The solid red line gives β_2 for the aligned assumption, and the dashed provides β_2 for the isotropic assumption. The value of β_4 is shown in green for the aligned assumption. For the isotropic assumption, the value of β_4 is zero. Measured spectra are in red, while calculated ones are in blue. The red and green squares represent the respective values of β_2 and β_4 measured at a particular wavelength. The bottom abscissa gives the transition energy from the NO $A\ ^2\Sigma^+$ (v = 0, N = 2, J=1.5) level. The top axis gives the total energy relative to the level NO $X\ ^2\Pi$ (v = 0, N = 1, J=0.5).

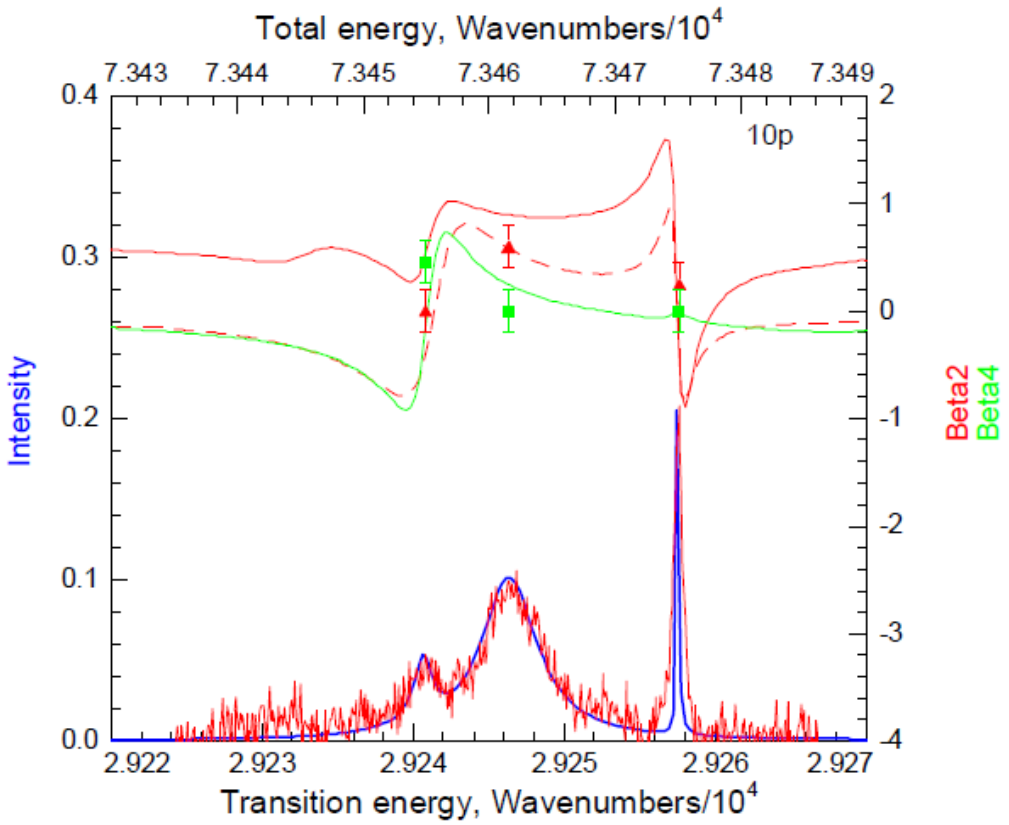

Figure 2.4. Experimental and theoretical results for the *10p*, v=0, Rydberg state. See the caption to Fig. 2.3 for an explanation of the symbols.

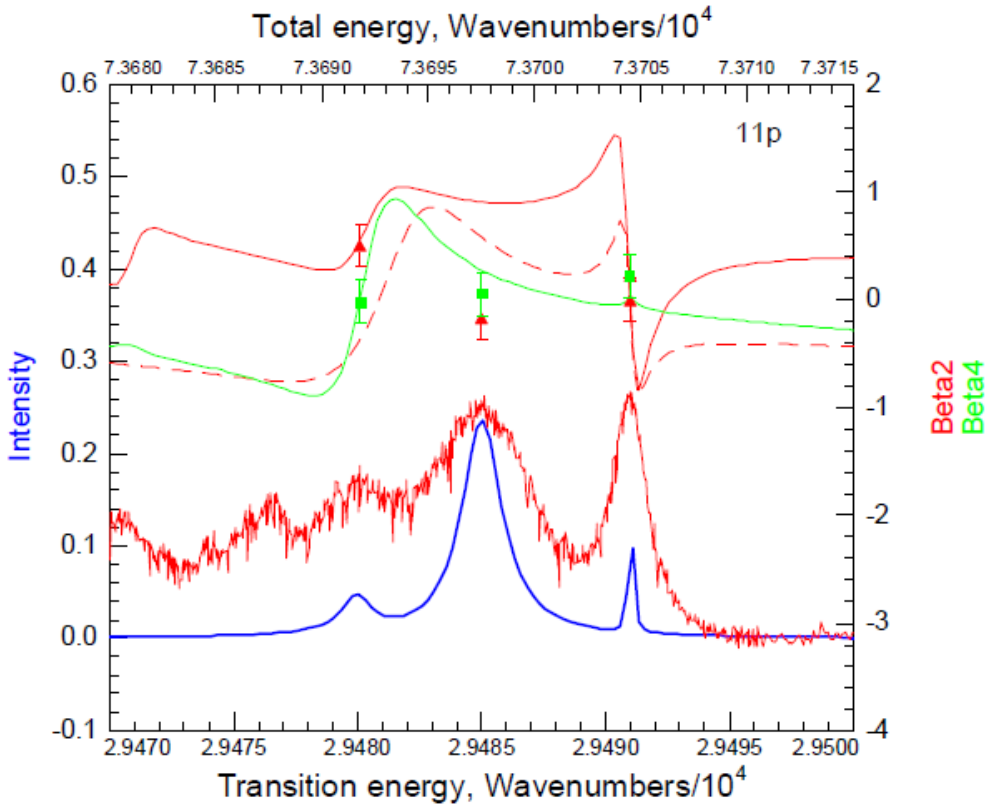

Figure 2.5. Experimental and theoretical results for the *11p*, v=0, Rydberg state. See the caption to Fig. 2.3 for an explanation of the symbols.

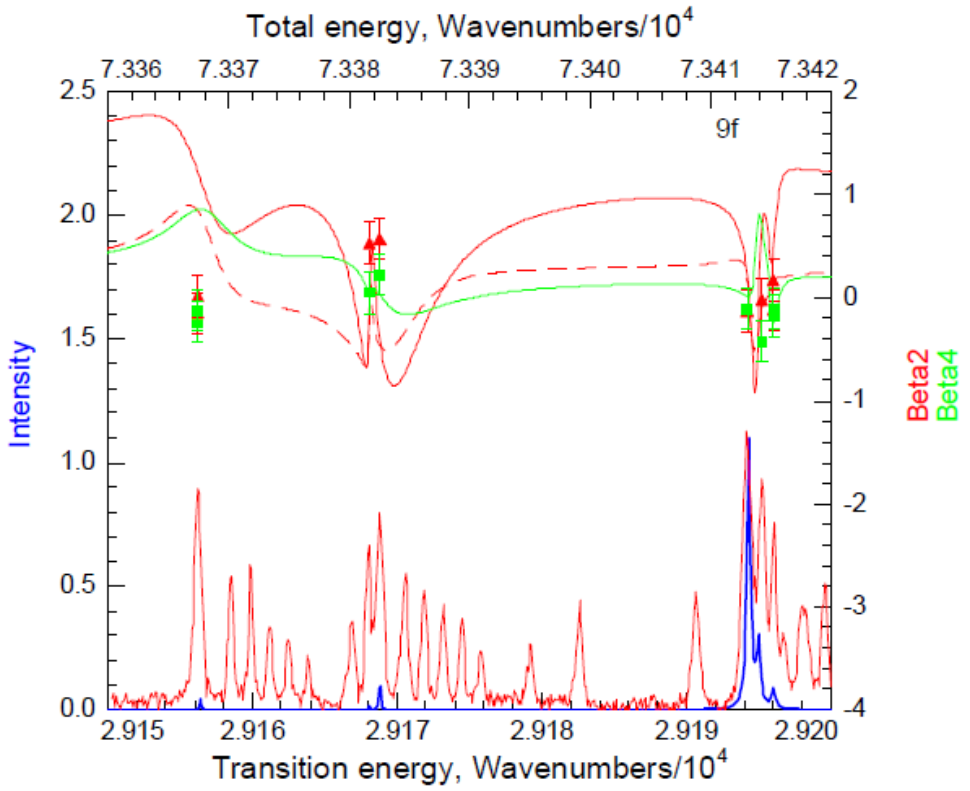

Figure 2.6. Experimental and theoretical results for the *9f*, v=0, Rydberg state. See the caption to Fig. 2.3 for an explanation of the symbols.

The calculated and measured spectra are shown but should be taken with some caution. First, the experimental spectra in the case of the *9f* and, to a lesser degree, the *11p* states are saturated spectra and differ from those published previously.[6,11] The additional lines in the *9f* spectrum could be caused by *l*-mixing or by other Rydberg-Rydberg interactions, or they could arise from inadvertent excitation of other rotational levels of the NO *A* ($^2\Sigma^+$) state. As mentioned previously, the calculational method may be inadequate for the former case, whereas in the second case the calculation should still produce the correct answer for the *9f* levels. Second, the calculations also have adjustable parameters, such as the value of Δv that determines the

broadening, discussed below.[14] Thus, the widths of the lines are fitted, while the intensities, angular distributions, and the positions are calculated. The calculated line positions are accurate and used for the *11s*, *10p*, and *11p* transitions. Those for the *9f* transition were not sufficiently accurate to match the experiment, and calculated values were adjusted by up to 0.5 cm^{-1} to match the experimental spectrum.

2.5 Discussion

The excitation of NO with wavelength λ_1 on the $^{S}R_{21}(0.5)$ line takes the molecule from the $X\ ^2\Pi_{1/2}$ F1, v=0, N=1, J=0.5 level to the $A\ ^2\Sigma^+$ F2, v=0, N=2, J=1.5 level. In linear polarization, the M_J level will not change in the excitation, and since the initial state has only $M_J = \pm ½$, the final state must also have only these two levels; that is, levels $M_J = \pm 3/2$ are missing and the state is said to have an aligned vector for the rotational angular momentum, ***N***. In time, however, ***N*** will become coupled with the spin angular momentum, ***S***, and the nuclear spin angular momentum, ***I***, resulting in loss of alignment. Reid has investigated the coupling time for such loss in the NO case.[23] For the state under consideration, use of her formulae provide a depolarization time of about 20 ns. Because the λ_2 laser pulse is timed to coincide with the λ_1 pulse to within 0-5 ns, it would seem that the alignment should be preserved for our experiment. Indeed, the presence of non-zero values for β_4 indicates that some alignment must take place. On the other hand, Bakker et al.[12] reported no evidence for alignment under similar conditions, although the $Q_{11} + P_{21}$ line(s) they used for excitation included more than one transition for each initial J level (more discussion of this issue will follow below). It appears quite likely that there is substantial retention of alignment in our experiment, but we have performed the calculation of

the angular distribution parameters for both assumptions B aligned and isotropic NO in the initial state selected by λ_1. There are of course differences in the results for the two assumptions, but for the wavelengths we measured the values of β_2 and β_4 on the peaks are not substantially different.

While the agreement between the calculated values of β_2 and β_4 and the measured ones in Figs. 2.3 – 2.6 is not perfect, it is fairly good. In the case of the 11s Rydberg state, there are only two observed lines, the R-branch transition at about 29392.3 cm^{-1} and the P-branch transition at about 29374.6 cm^{-1}. The measured values for β_2 and β_4 are both small but positive, in agreement with the prediction for the P-branch transition, but somewhat below the prediction for the R-branch. For the *10p* and *11p* Rydberg states, the results are in fairly good agreement with the predictions for all three transitions. For the *9f* Rydberg state, the agreement is similarly good, except that the results for the $^{-2}R_3$ line at 29156.2 cm^{-1} are both a bit low compared to theory. Bakker et al.[12] have reported the velocity and angular distributions of N($^2D_{3/2}$) following two-photon dissociation of NO using techniques similar to those used in the current study. In their case, the laser fundamental was tripled to provide the $A\ ^2\Sigma^+ \leftarrow X\ ^2\Pi$ excitation of NO and was also doubled to provide the excitation from the $A\ ^2\Sigma^+$ state to the *11p* Rydberg state at 29465 cm^{-1}. This wavelength is not resonant with any transition from N=2 of the NO $A\ ^2\Sigma^+$ state to the Rydberg state, and the authors suggested that the transition originated from the N=3 level of the NO A state, also populated by the $A\ ^2\Sigma^+ \leftarrow X\ ^2\Pi$ excitation that they used. (They excited NO on the $Q_{11}+P_{21}$ bandhead, whereas the current work excited it on the $^SR_{21}(0.5)$ line, the line also used previously by Geng et al.[11]) With this assumption, excitation in the Bakker et al. experiment could occur on a weak transition to the N=3, $^2\Pi^+$ component of the *11p* Rydberg level. Their measurement of the angular distribution, obtained both from the N($^2D_{3/2}$) image and

from multiple measurements of the O($^3P_2$) image, gave $\beta_2 = -0.71 \pm 0.17$ and $\beta_4 = 0$. While they argue that a negative value of β_2 should be expected on the basis of a $^2\Pi \leftarrow {}^2\Sigma^+$ transition, this argument is true for all J values only if the lifetime broadening is large compared to the rotational spacing. The individual rotational transitions are clearly evident in the spectra, so this condition is not met. The argument would also depend on starting from unaligned levels in the NO *A* $^2\Sigma^+$ state.

A careful consideration of all the transitions that could have been excited in the experiment of Bakker et al. leads to a somewhat different explanation for their observation. We agree that the most likely transition is from N=3 level of the NO *A* $^2\Sigma^+$ state; other levels do not have the correct total energy to contribute. Under this assumption, the total energy of their experiment is the energy of the photons plus the energy of NO *X* $^2\Pi_{1/2}$ (v=0, J=3.5), measured for our purposes relative to the energy of the lowest level, NO *X* $^2\Pi_{1/2}$ (v=0, J=0.5): E_{tot}= 44197 + 29465 + 25.1 = 73687.1 cm^{-1}.

Excitation to the NO *A* $^2\Sigma^+$ state in their experiment takes place on two transitions, each of which would be expected to produce alignment. Excitation on the P_{21} transition produces NO (*A* $^2\Sigma^+$, v=0, J=2.5, N=3, F2) with an M_J distribution that varies as (J^2 - M_J^2).[19] Excitation on the Q_{11} transition produces NO (*A* $^2\Sigma^+$, v=0, J=3.5, N=3, F1) with an M_J distribution that varies as M_J^2. Based on our own results and the calculations of Reid,[23] it seems likely that these alignments would persist on the time scale of the experiment. However, we note that they are opposite in sign. The two transitions are coherently excited, since they originate from the same state in NO *X* $^2\Pi_{1/2}$. A proper calculation would take into account the interference between these two paths, but the likely result would be that, on average, there would be little overall alignment.

Bakker et al.[12] reported that there was no evidence for alignment, as judged by the lack of need for a non-zero β_4 parameter in their angular fits.

With either of the NO *A* $^2\Sigma^+$ excitations they used, the next photon would excite the molecule to the *11p* Rydberg state at an energy between that of the (very weak) $^{-2}P_1$ transition to the N=2, P=1, $^2\Pi^+$ level and that of the strong $^0Q_0$ transition to the N=3, P=0, $^2\Pi^-$ level. For reasonable parameters, a calculated spectrum for this energy range and transition is shown in Figure 2.7, made under the assumption that the level in the NO *A* $^2\Sigma^+$ state is not aligned and that the excitation to that state from the ground state was on the P_{21} transition. The $^0Q_0$ transition from the resulting NO *A* $^2\Sigma^+$ state to the $^2\Pi^-$, *11p* Rydberg state is a shoulder at a total energy of 73703 cm^{-1}. The $^{-2}P_1$ transition is too weak to be seen at 73687.2 cm^{-1}, in agreement with the fact that it is unobserved in the work of Geng et al .[11] Our calculations show that both the $^{-2}P_1$ and $^2R_{-1}$ transitions that Geng et al..[11] thought should be allowed but did not observe are at least ten times weaker than the main peaks for comparable linewidths. Figure 2.7 provides the calculated anisotropy parameters along with symbols representing the measurement by Bakker et al.[12] As can be seen from the diagram, the calculated values for β_2 and β_4 are not far from their measurements. The principal absorption, however, is on the wings of the $^0Q_0$ transition rather than on the $^{-2}P_1$ transition; the former is calculated to have a value of β_2 = -0.69 in isolation and on resonance, while the latter has one of β_2 = 0.10. A very similar calculated plot is obtained under the assumption that the level in the NO *A* $^2\Sigma^+$ state is not aligned and that the transition to that state is Q_{11} rather than P_{21}. We note that for our own experimental conditions shown in Fig. 2.5 the calculated value of β_2 at the $^2\Pi^-$ state (29480 cm^{-1}) would be near β_2 = -0.5 if we had started with NO that was not aligned. It appears that the positive values we find for this state in the *11p* and *10p* Rydbergs are due to the fact that our NO *A* $^2\Sigma^+$ state molecules are aligned,

whereas the alignment effects likely cancel in the multiple transition excitation scheme used Bakker et al.[12]

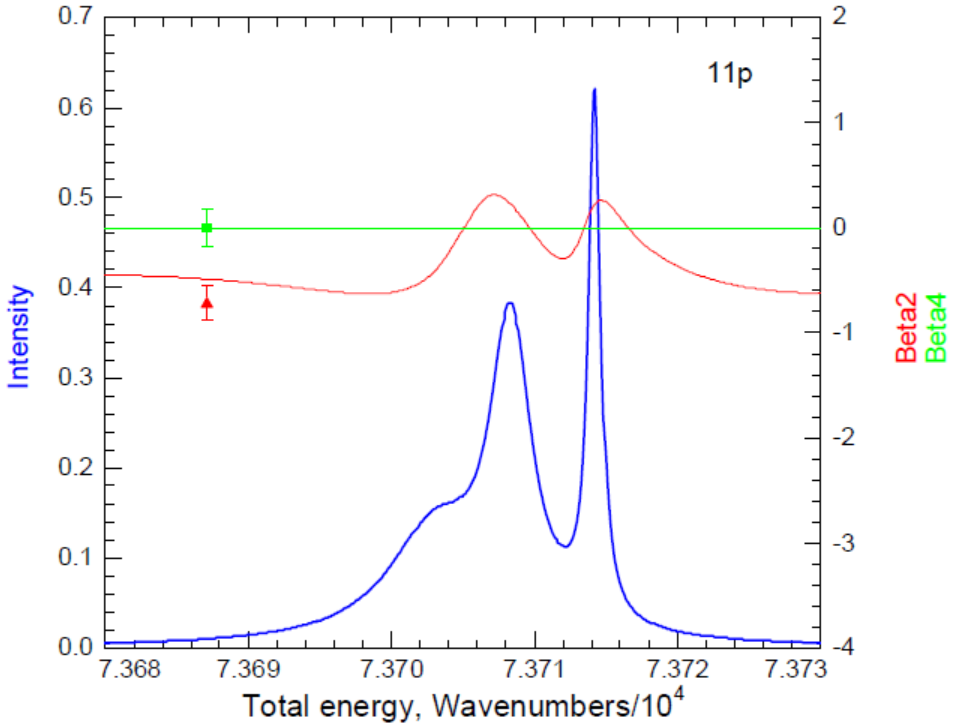

Figure 2.7. Experimental results from Bakker et al.[12] along with calculated results for their experiment, assuming $A \leftarrow X$ excitation on the P_{21} transition and a non-aligned sample. A similar result is found for $A \leftarrow X$ excitation on the Q_{11} transition.

The roles of photoionization and photodissociation in *np* Rydberg states of NO has been extensively studied by Giusti-Suzor and Jungen.[5] Predissociation is predominantly caused by Rydberg-valence interactions between the excited states and either the NO $B\ ^2\Pi$ or $L\ ^2\Pi$ states. The mechanism of predissociation thus appears to be electrostatic in nature and due to the $1/r_{12}$ operator.[24] It is interesting, then, to correlate the rate of predissociation, as evidenced by the linewidths of transitions, with the degree of Π character in the Rydberg state. The results are

most noticeable in the *10*p spectrum shown in Fig. 2.4 and *11p* spectrum shown in Fig 2.5. In each case, the three main peaks in increasing order of energy are the $^2\Pi^-$, the $^2\Pi^+$, and the $^2\Sigma^+$, and the widths entered in the calculation were {1.5, 4.6, and 0.15 cm^{-1}} for the *10p* and {1.5, 2.0, and 0.15 cm^{-1}} for the *11p*. Recall that the Rydberg states can be decomposed into case (a) basis functions, in this case Π and Σ states. The $^2\Pi^-$ Rydberg is pure case (a) Π^-, whereas the $^2\Pi^+$ and $^2\Sigma^+$ Rydbergs are each mixtures of Π and Σ case (a) basis functions. Because the predissociation coupling is homogeneous, one might expect the linewidths to correlate with the square of the case (a) Π coefficient. The squares are, respectively, {1.00, 0.82, and 0.05} for the *10p* and {1.00, 0.78, .07} for the *11p*. The correlation between these squares and the linewidths extracted from the experimental spectra is not exact, but it does provide some understanding of why the $^2\Sigma^+$ component of the *np* Rydberg states is so sharp relative to the others. In the case of the *9f* Rydberg states, there is not a noticeable difference in the broadening among the lines, and, in general, the case (a) Π component is more evenly spread among the transitions.

2.6 Conclusions

The theory of Kim et al.[14] modified as described above to include transitions to mixed case (a,b)/(d) coupling states appears to correctly predict the angular distribution of products from the photodissociation of NO through a variety of *n*s, *n*p, and *n*f Rydberg levels, as measured by velocity-mapped imaging. The theory also accounts for the experimental results of Bakker et al.[12] under the assumption that alignment effects cancel in their excitation via multiple transitions. The degree of case (a) Π character in the *10p* and *11p* Rydberg states appears to

correlate with the rate of predissociation, in agreement with previous results that suggest that a homogeneous dissociative transition to either the $B\,^2\Pi$ or $L\,^2\Pi$ state.

2.7 References

[1]Ch. Jungen and E. Miescher, *Can. J. Phys.* **47**, 1769 (1969).

[2] E. Miescher and K. P. Huber, *Int. Rev. Sci. Phys. Chem. Ser. 2* **3**, 37 (1976).

[3]S. Fredin, D. Gauyacq, M. Horani, C. Jungen, G. Lefevre, and F. Masnou-Seeuws, *Mol. Phys.* **60**, 825 (1987).

[4]M. Raoult, S. Guizard, and D. Gauyacq, *J. Chem. Phys.* **87**, 4736 (1987).

[5]A. Guisti-Zuzor and Ch. Jungen, *J. Chem. Phys.* **80**, 986 (1984).

[6]Y. Anezaki, T. Ebata, N. Mikami, and M. Ito, *Chem. Phys.* **97**,153 (1985).

[7]D. T. Biernacki, S. D. Colson, and E. E. Eyler, *J. Chem. Phys.* **88**, 2099 (1988).

[8]A. Fujii and N. Morita, *Chem. Phys. Lett.* **182**, 304 (1991).

[9]A. Fujii, and N. Morita, *J. Chem. Phys.* **98**, 4581 (1993).

[10]J. Geng, T. Kobayashi and M. Takami, *RIKEN Rev.* **15**, 81 (1997).

[11]J. Geng, T. Kobayashi and M. Takami, *Chem. Phys. Lett.* **266**, 290 (1997).

[12]G. L. G. Bakker, A. T. J. B. Eppink, D. H. Parker, M. L. Costen, G. Hancock and G. A. D. Ritchie, *Chem. Phys. Lett.* **283**, 319 (1998).

[13]T. Kobayashi, J. Geng and M. Takami, *Chem. Phys. Lett.* **284**, 195 (1998).

[14]H. Kim, K. S. Dooley, S. W. North, G. E. Hall and P. L. Houston, *J. Chem. Phys.* **125**, 133316 (2006).

[15]G. Black and L. E. Jusinski, *Chem. Phys. Lett.* **139**, 41, 1987; H. Umemoto, M. Kashiwazaki, and T. Yahata, *J. Chem. Soc. Faraday Trans.* **94**, 1793 (1998).

[16]D. W. Chandler and P. L. Houston, *J. Chem. Phys.* **87**, 1445 (1987).

[17]D. H. Parker and A. T. J. B. Eppink, *J. Chem. Phys.* **107**, 2357 (1997).

[18]V. Dribinski, A. Ossadtchi, V.A. Mandelshtam, and H. Reisler, *Rev. Sci. Instrum.* **73** 2634 (2002).

[19]R. G. Bray and R. M. Hochstrasser, *Mol. Phys.* **31**, 1199 (1976).

[20]R. N. Zare, *Ber. Bunsenges. Phys. Chem.* **86**, 422 (1982).

[21]R. N. Zare, *Angular Momentum,* John Wiley & Sons, New York, 1988, pp. 302ff. Also, see errata sheet, http://www.stanford.edu/group/Zarelab/Errata.pdf

[22]M. S. Child, *Theory of Molecular Rydberg States,* Cambridge Univ. Press, 2011.

[23]K. L. Reid, *Chem. Phys. Lett.* **215**, 25 (1993).

[24]H. Lefebvre-Brion and R. W. Field, *Perturbations in the Spectra of Diatomic Molecules*, Academic Press, Orlando, Florida, 1986.

Chapter 3

3. Introduction to High Resolution Coherent Multidimensional Spectroscopy

High-resolution spectroscopy is sometimes limited to diatomics and other small molecules that yield relatively simple and uncongested spectra. Larger molecules, and some small molecules like NO_2 where conical intersections make the interpretation of one-dimensional spectra difficult, require a different type of technique in order to resolve and identify peaks. High Resolution Coherent Two-dimensional Spectroscopy (HRC2DS), and more recently, High Resolution Coherent Three-dimensional Spectroscopy (HRC3DS) have been developed to investigate these types of spectra.

Both HRC2DS and HRC3DS involve nonlinear optical processes. When the magnitude of the input electric fields become comparable to or stronger than the electric fields present in the sample, the polarization induced in the sample is distorted by the input electric fields. In general, the polarization of a sample resulting from interaction with one or more electric fields can be written as a Taylor series:

$$\vec{P} = \tilde{\chi}^{(1)}_{i,j}\vec{E} + \tilde{\chi}^{(2)}_{i,j,k}\vec{E}^2 + \tilde{\chi}^{(3)}_{i,j,k,l}\vec{E}^3 + \ldots.$$

where $\vec{E}$ is the total electric field from all the input laser sources exciting the sample, $\vec{E} = \sum_i \vec{E}_i$ and $\tilde{\chi}^{(n)}$ is the n^{th} order susceptibility term.[1] The susceptibility term for n=1 describes linear processes while all higher order terms describe nonlinear processes. For an isotropic sample, such as an ensemble of molecules in the gas phase, $\tilde{\chi}^{(2)}_{i,j,k}$ terms must vanish, since the

polarization must reverse if the electric field reverses. As shown by the above Taylor expansion, in fact all even-ordered susceptibility tensors must not exist for an isotropic sample.

However $\tilde{\chi}^{(2)}_{i,j,k}$ plays a significant role at interfaces, where the sample can no longer be considered isotropic. For an input electric field with wave vector *k* and frequency ω,

$$\vec{E_i} = \tfrac{1}{2}\vec{E_i}^{0}\left(e^{i(\vec{k_i}\vec{z} - \omega_i t)} + e^{-i(\vec{k_i}\vec{z} - \omega_i t)}\right)$$

.

For two input beams with frequencies ω_1 and ω_2, when the $\chi^{(2)} E^2$ term in the above Taylor series is expanded, the polarization will have terms oscillating at $e^{2i(k_1 z - \omega_1 t)}$, $e^{i[(k_1+k_2)z-(\omega_1+\omega_2)t]}$, and $e^{i[(k_1-k_2)z-(\omega_1-\omega_2)t]}$, among others.[1] The nonlinear processes associated with each one of these terms in the polarization are second harmonic generation (SHG), sum frequency generation (SFG), and difference frequency generation (DFG) respectively, all of which are considered three wave mixing (TWM) processes, since two input light waves mix to create a third wave. These processes are commonly seen when using beta barium borate (BBO) or potassium dideuterium phosphate (KDP) crystals in laser applications.

3.1 Four Wave Mixing

HRC2DS and HRC3DS are both based on four wave mixing (FWM) techniques. For HRC2DS, one input source is a narrow-band, tunable laser while the other is a broadband optical parametric oscillator (OPO) that generates a large range of frequencies simultaneously. Two of the three mixing waves in this case come from the broadband OPO. For HRC3DS, two narrow-

band, tunable sources are used as well as the broadband OPO. Generally though, either case can be examined using three input laser sources with frequencies ω_1, ω_2, and ω_3. Expanding the $\chi^{(3)}$ E^3 term in the same manner as the second order term above, the polarization will have terms oscillating at $e^{3i(k_1 z-\omega_1 t)}$, $e^{i\left[(2k_1-k_2)z-(2\omega_1-\omega_2)t\right]}$, and $e^{i\left[(k_1-k_2+k_3)z-(\omega_1-\omega_2+\omega_3)t\right]}$ among others.[1] The nonlinear processes associated with the first two terms listed are frequency tripling and coherent anti-Stokes Raman Spectroscopy (CARS). The third term is one of many similar terms associated with general FWM processes, and it is these processes that will be examined more closely later on.

In these FWM processes, the output beam with frequency ω_4 can be any combination of the sum or difference of the input frequencies. The input fields must be carefully phase matched, and for the general FWM process above, the output wave vector is $\vec{k}_4 = \frac{n_4\left(\omega_1-\omega_2+\omega_3\right)}{c}\vec{a}_4$, where n_4 is the index of refraction experienced by $\vec{k}_4$ and $\vec{a}_4$ is the unit vector of the direction of the output beam. The condition for proper phase matching in this case is $\vec{k}_4 = \vec{k}_1 - \vec{k}_2 + \vec{k}_3$. The simplest way to achieve phase matching is to bring the input waves into the sample collinearly. For condensed phase spectroscopy, this is often not possible, since the real part of the refractive index of most condensed materials increases as the frequency of light interacting with the medium increases. This would likely result in a phase mismatch Δk. Figure 3.1a shows a situation where a four-wave mixing process is properly phase matched, where Figure 3.1b demonstrates improper phase matching and shows the resultant phase mismatch vector Δk.

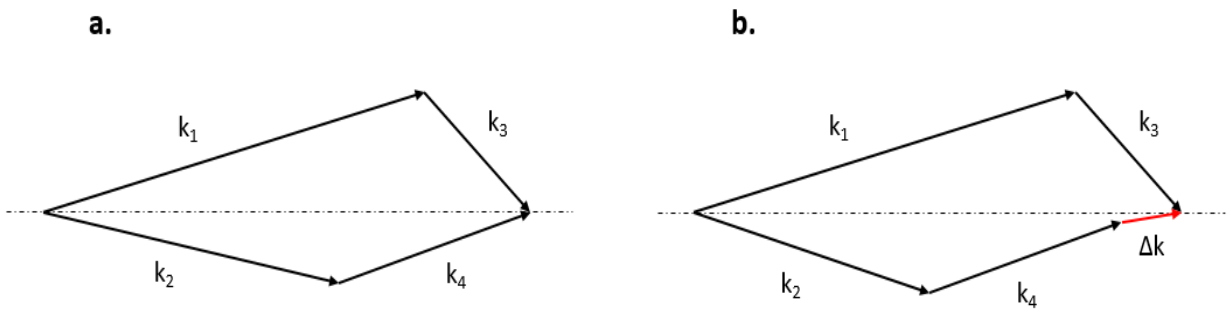

Figure 3.1 a) A vector diagram of a four wave mixing process that is properly phase matched. b) A similar diagram except this process is not properly phase matched, note that the phase mismatch vector Δk is colored in red.

For gas phase samples, usually the real part of the refractive index is fairly constant with respect to frequency, and therefore collinear phase matching is possible, which was the technique used in the experiment. However collinear phase matching results in the output beam travelling in the same direction as the three input beams, and thus requires the user to filter out the input frequencies in order to examine the resultant beam. One method to avoid the need to filter out the input beams is to bring the input beams into the sample at different angles, such that the vector addition results in phase matching. The scalar equations that must be satisfied in this geometry of phase matching are as follows: $\omega_4 = \omega_1 - \omega_2 + \omega_3$, $n_1\omega_1\sin(\theta_1) = n_3\omega_3\sin(\theta_3)$, $n_2\omega_2\sin(\theta_2) = n_4\omega_4\sin(\theta_4)$, and $n_1\omega_1\cos(\theta_1) + n_3\omega_3\cos(\theta_3) = n_2\omega_2\cos(\theta_2) + n_4\omega_4\cos(\theta_4)$, where n_i is the refractive index the i-th wave experiences, and θ_i is the angle the i-th input wave makes with the resultant output wave, k_4 (Figure 3.2).

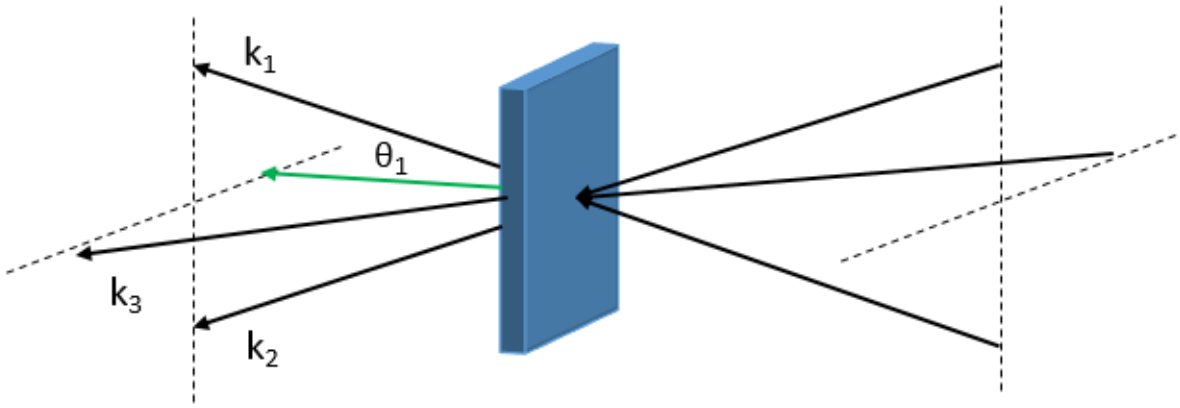

Figure 3.2. A common orientation for noncollinear phase-matched four wave mixing. Note that the resultant wave vector is colored in green and makes an angle θ_i with respect to each vector k_i

The result of the FWM processes used in High Resolution Coherent Multidimensional Spectroscopy (HRCMS) is an output beam with frequency ω_4, indicating that the process must be coherent, as will now be described. If a molecule has two quantum states *a* and *b*, and c_a and c_b are the amplitudes for the molecule being in each state, then $c_a\, c_a^*$ and $c_b\, c_b^*$ give the population of each state. Similarly $c_a\, c_b^*$ and $c_b\, c_a^*$ measure the coherence of the two states. A coherence is a quantum mechanical superposition of the two states, whose wavefunction can be written as $\Psi(x,t) = \left|\psi_a(x)e^{i\omega_a t} + \psi_b(x)e^{i\omega_b t}\right|^2$, which has cross terms that oscillate at $\omega_{ba} = \omega_b - \omega_a$. This coherence launches the fields that are responsible for molecular spectroscopy. Assuming that state *b* is significantly higher in energy than state *a*, the population $c_a \sim 1$ and $c_b \sim 0$ with no influence from an external electric field. Turning on a field of frequency ω_{ba} will cause the system to absorb energy from the field, until the populations reverse, at which point the

system will start emitting energy and the original populations of states *a* and *b* will return. These two processes are of course stimulated absorption and emission, and the cycle from the initial state and back again is called a Rabi oscillation. The Rabi frequency is $\Omega = \frac{\vec{\mu} \cdot \vec{E}}{2\hbar}$, where μ is the transition dipole induced by the electric field, $\vec{E}$. It is important to note that the Rabi frequency increases as the intensity of $\vec{E}$ increases, a fact that HRCMS takes advantage of. Interactions of the molecules with the surrounding environment, such as collisions and thermal fluctuations, will cause decoherence of the molecular states, which causes the phase relationship of the polarization to the external field to be lost. Some representative dephasing rates are ~10^3 sec^{-1} for condensed phase NMR, ~10^{12} sec^{-1} for vibrational states, and ~10^{14} sec^{-1} for electronic states. The dephasing time is longer in gas phase spectroscopy when compared to condensed phase, however it cannot be ignored. Since the three external fields must interact with the sample coherently, the ratio of the Rabi frequency to the dephasing rate must be such that successive resonance enhancements can occur. The high electric field strengths employed by the HRCMS techniques ensure that the Rabi frequency is comparable to or higher than the dephasing rate, Γ, which permits the three external fields to interact with the sample coherently.[1]

The character of a nonlinear optical process is determined by a succession of coherences and populations that are created by successive interactions with the external input fields. One common notation used to describe these successions of coherences is by use of bra and ket notation. In general, for a system with two states *i* and *j* interacting with a resonant electric field with frequency ω_{ij}, the entangled states can be written as a density matrix element ρ_{ij}. This is equivalent to $\rho_{ij} \Rightarrow |i\rangle\langle j|$, where the first subscript *i* corresponds to the ket, and the second

subscript *j* corresponds to the bra. Absorption and refraction are both indicated by a single interaction with the ket, so for a system with a population *jj*, a single interaction with the resonant electric field would create a superposition of states, which can be denoted $jj \rightarrow ij$. Now consider another system that will be representative of the systems investigated using HRCMS. There would be a ground level g, and several excited levels a, b, c, and so on. If the first input field (with frequency ω_{ag}) causes a coherence that does not dephase before the Rabi cycle ends, $gg \rightarrow ag$, then successive interactions with the second and third fields (with frequencies ω_{ba} and ω_{cb} respectively) will cause an evolution of resonances, $gg \rightarrow ag \rightarrow bg \rightarrow cg$.[1]

3.1.1 Wave Mixing Energy Level Diagrams

Wave mixing energy level diagrams are a pictorial representation of the energy levels and resonances involved in the FWM process and work well in conjunction with the Dirac notation. For the three input and one output fields involved in HRCMS, there are ten distinct four wave mixing energy level diagrams possible (Figure 3.3).[2] It is important to note that the letters assigned to the energy levels in the wave mixing energy level diagrams do not match the brief example mentioned above. In the ten diagrams in Figure 3, the lowest energy level or ground level is denoted level a, while each excited state is denoted letters b-h, dependent on their energy relative to level a. The first four of those ten processes are parametric processes, meaning the final emitting coherence involves the initial state. From the example above, after the *cg* coherence emits, the molecule returns to the ground level. The other six FWM processes are nonparametric, and the emitting resonance involves a level that is either higher or lower in

energy than the initial state. It is important to note that there are many more four wave mixing diagrams possible for the input and output fields if we consider the cases where a singular input field can interact more than once, and thus one of the input fields would not interact. The ten possible diagrams considered are the ones where each of the three input fields contributes to the output field. It is possible that many of the processes can contribute somewhat to the overall signal in the experiment, however it is likely that one or two processes will dominate the output signal.

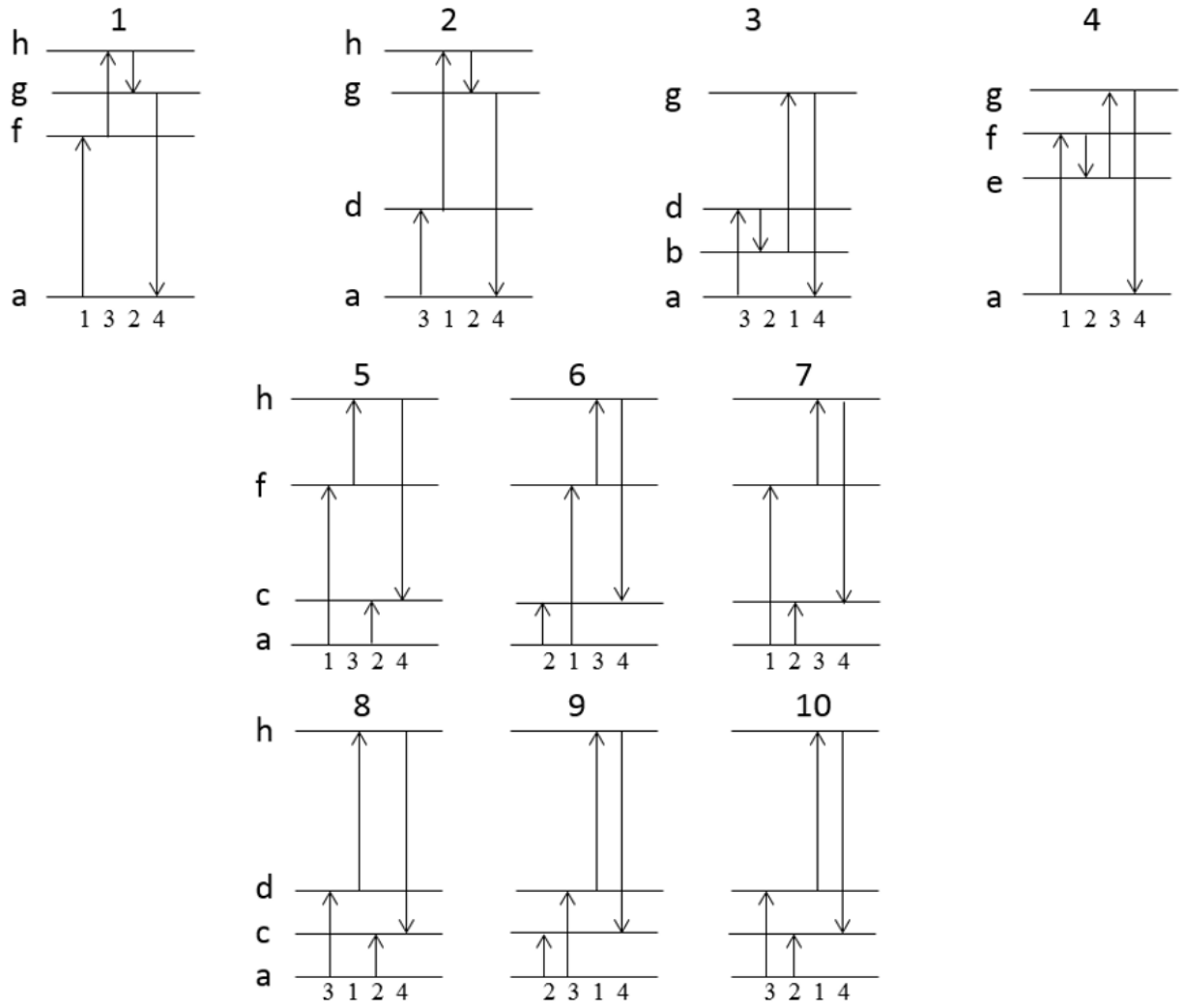

Figure 3.3. The ten distinct wave mixing energy level diagrams generated from the four wave mixing processes involved in HRCMS when $\omega_4 > \omega_1 > \omega_3 > \omega_2$. Note that the numbers 1-4 at the bottom of each diagram represent ω_1, ω_2, ω_3, ω_4.[2]

3.1.2 Resonance

One main reason that the four wave mixing diagrams considered for HRC3DS are the ones where each of the three distinct input fields contributes to the output field is that the signal in the experiment is triply resonant. Not only does the output signal depend on all three of the input fields being present, but the signal strength is also greatly enhanced when the frequency of each input field matches a resonant frequency in the sample. It is typical for triply resonant signal in the experiment to be at least ten times more intense than doubly or singly resonant signal. With regards to multiplicity of the resonances in HRCMS, it is helpful to consider what the output would look like in each case. For conventional one-dimensional spectroscopy, the single input frequency being resonant with the sample yields a peak in the output spectrum. For two dimensional, coherent spectroscopy, if only one of the two input frequencies is resonant with the sample, the output spectrum will contain a continuous line of signal. If one pictures a set of three frequency axes, one being the output and the other two the independent input frequency axes, if one input frequency is resonant with the sample, then there will be singly resonant signal present at that frequency for every point along the second input frequency axis. Only when both input frequencies are resonant with the sample will the spectrum contain discreet peaks. Finally for three dimensional, coherent spectroscopy, when only one of the three input frequencies are resonant with the sample, the spectrum will contain a continuous plane of signal. For example if the first input frequency is resonant with the sample, the plane that the second and third frequency axes create contain singly resonant signal at every point. When two frequencies are resonant, a continuous line would be present, similar to the situation described above. In this case, only when all three input frequencies are resonant with the sample are peaks the result. As

an example of this, the peaks in our HRC3DS spectra are all a result of triply resonant signal. However in the raw data, a horizontal line of signal is present, which is doubly resonant CARS signal that is independent of the one input field. This signal is very weak compared to the triply resonant signal, and is filtered out by the peak picking software that will be described later.

When three input fields interact coherently with a sample, the resulting intensity of the FWM signal is dependent upon the intensities if the three input fields according to the expression

$$I_{\mathrm{FWM}} \approx I_1 I_2 I_3 \left|\chi^{(3)}\right|^2 \left[\mathrm{sinc}\left(\frac{L\Delta k}{2}\right)^2\right]$$

where I_i is the intensity of each of the three input fields, $\chi^{(3)}$ is the 3rd order susceptibility term, L is the wave-mixing path length, and Δk is the wave vector mismatch.[3] Note that $\mathrm{sinc}(L\Delta k/2)^2 = 1$ when the three input fields are properly phase matched ($\Delta k = 0$). The third order nonlinearity $\chi^{(3)}$ is a sum of contributing terms that are directly proportional to the product of the four molecular dipole moments associated with interaction of the three input fields and the FWM field

$$\chi^{(3)} \approx \sum_{i,j,k} \frac{\mu_i \mu_j \mu_k \mu_l}{\Delta_i \Delta_j \Delta_k}$$

where each μ is a transition dipole moment of the molecule for interaction with the four fields.[3] The three resonance denominators have the general form $\Delta = \delta - i\Gamma$, where δ is the difference between the molecular transition frequencies and the input laser frequencies, and Γ is the dephasing rate. Resonance enhancement is achieved when one or more or the input field frequencies approach the molecular frequencies; when the field frequencies are much different from those of the molecule, the denominators are large and real, and the observed spectra will be

broad and rather featureless. When an input field frequency is resonant with a molecular frequency, $\delta = 0$, then $\Delta \rightarrow -i\Gamma$, and the amplitude of the nonlinear oscillation increases, producing a resonance peak in the spectrum.[3] Maximum resonance enhancement is achieved when all three of the resonance denominators collapse to $\Delta \rightarrow -i\Gamma$, and the resultant signal, as described above, is referred to as triply or fully resonant.

3.2 Bromine as a Model for HRCMS

The bromine atom and the Br_2 molecule have been very well studied since the element was first isolated in 1825. The bromine atom has two stable isotopes, ^{79}Br which accounts for 50.69% of the naturally occurring bromine, and ^{81}Br which accounts for the remaining 49.31%. This isomeric distributions leads to three common isotopologues of the bromine molecule: ^{79}Br-^{79}Br, ^{79}Br-^{81}Br, and ^{81}Br-^{81}Br, which naturally occur in roughly a 1:2:1 ratio. The first isotopologue will often be referred to as the 79 isotopologue, the second as the mixed isotopologue, and the third as the 81 isotopologue.

The first vibrational analysis on the bromine molecule was done by Kuhn in 1926,[4] which covered the visible range from 5117-6722 Å with the exception of 5280-5550 Å. In 1931, Brown established that there were two absorption systems in the region 5113-7605 Å. One was referred to as the "main system" and consisted of six v' progressions from 5113-6590 Å, and the other was referred to as the "extreme red" system, which consisted of five v' progressions from 6448-7605 Å. The more intense, main system is attributed to the transition $B\,^3\Pi_{0+u} - X\,^1\Sigma_g^+$ and the weaker, secondary system is attributed to the transition $A\,^3\Pi_{1u} - X\,^1\Sigma_g^+$. Brown[5] then

rotationally analyzed a group of bands with $2 \leq v'' \leq 4$ and $7 \leq v' \leq 13$ of the mixed isotopologue around the same time as Mulliken[6] established his electronic assignment of the $B\ ^3\Pi_{0+u} - X\ ^1\Sigma_g^+$ main system of Br_2.

In 1967 Horsely and Barrow[7] separately recorded the $B\ ^3\Pi_{0+u} - X\ ^1\Sigma_g^+$ spectra of the 79 and 81 isotopologues of Br_2 in the 5100-6200 Å region and rotationally resolved bands involving the $0 \leq v'' \leq 3$ and $9 \leq v' \leq 19$. A few years later in 1971, Coxon[8] recorded a high resolution spectrum of the $B\ ^3\Pi_{0+u} - X\ ^1\Sigma_g^+$ system of the 79 isotopologue in the range 6350-7700 Å, and used this data to calculate Rydberg-Klein-Rees (RKR) potential energy curves for the $B\ ^3\Pi_{0+u}$ and $X\ ^1\Sigma_g^+$ states. In 1974 Coxon, Barrow, and others[9] published a more complete analysis of the $B\ ^3\Pi_{0+u} - X\ ^1\Sigma_g^+$ system, including rotational constants and Franck-Condon factors for $0 \leq v'' \leq 10$ and $0 \leq v' \leq 55$ for the 79 isotopologue and $0 \leq v'' \leq 3$ and $v' = 9$, 11-13, 16, 19, and 39-54 for the 81 isotopologue.

Then in 1987, building upon the existing data, Gerstenkorn, Luc, and others[10] recorded for the 79 isotopologue a $B\ ^3\Pi_{0+u} - X\ ^1\Sigma_g^+$ absorption spectrum covering the 11600-19577 cm^{-1} region by means of Fourier Transform Spectroscopy. Analysis of the ~80000 transitions led them to publish an atlas where the transitions for $0 \leq v'' \leq 14$ and $0 \leq v' \leq 52$ could be calculated by a set of Dunham parameters.

J. L. Dunham[11] proposed in 1932 that one could express the rotational-vibrational energy levels of a diatomic molecule as an expansion of the form

$$E(v, J) = \sum_{k,l} Y_{k,l}(v + \tfrac{1}{2})^k [J(J+1)]^l$$

where v and J are the rotational and vibrational quantum numbers. The $Y_{k,l}$ constant coefficients are referred to as the Dunham parameters. Table 3.1 enumerates many of the Dunham parameters, along with their more common representations.

Table 3.1. A list of many important Dunham parameters, their equivalent symbols in rotational-vibrational spectroscopy, and the common name of the term, when applicable.

Dunham Parameter	Alternate Symbol	Common Name
$Y_{0,0}$	T_e	Electronic energy
$Y_{1,0}$	ω_e	Harmonic frequency
$Y_{2,0}$	$-\omega_e x_e$	Anharmonicity term
$Y_{3,0}$	$\omega_e y_e$	
$Y_{0,1}$	B_e	Rotational constant (equilibrium)
$Y_{1,1}$	$-\alpha_e$	Vibration-rotation interaction constant
$Y_{2,1}$	γ_e	
$Y_{0,2}$	D_e	Centrifugal distortion constant
$Y_{1,2}$	β_e	
$Y_{0,3}$	F_e	
$Y_{0,4}$	H_e	

Further analysis by Gerstenkorn and Luc[12] in 1989 led them to calculate a set of Dunham parameters for all three isotopologues of Br_2. Figure 3.4 shows the calculated potential energy curves for the B $^3\Pi_{0+u}$ and X $^1\Sigma_g^+$ states of Br_2 from Gerstenkorn and Luc.

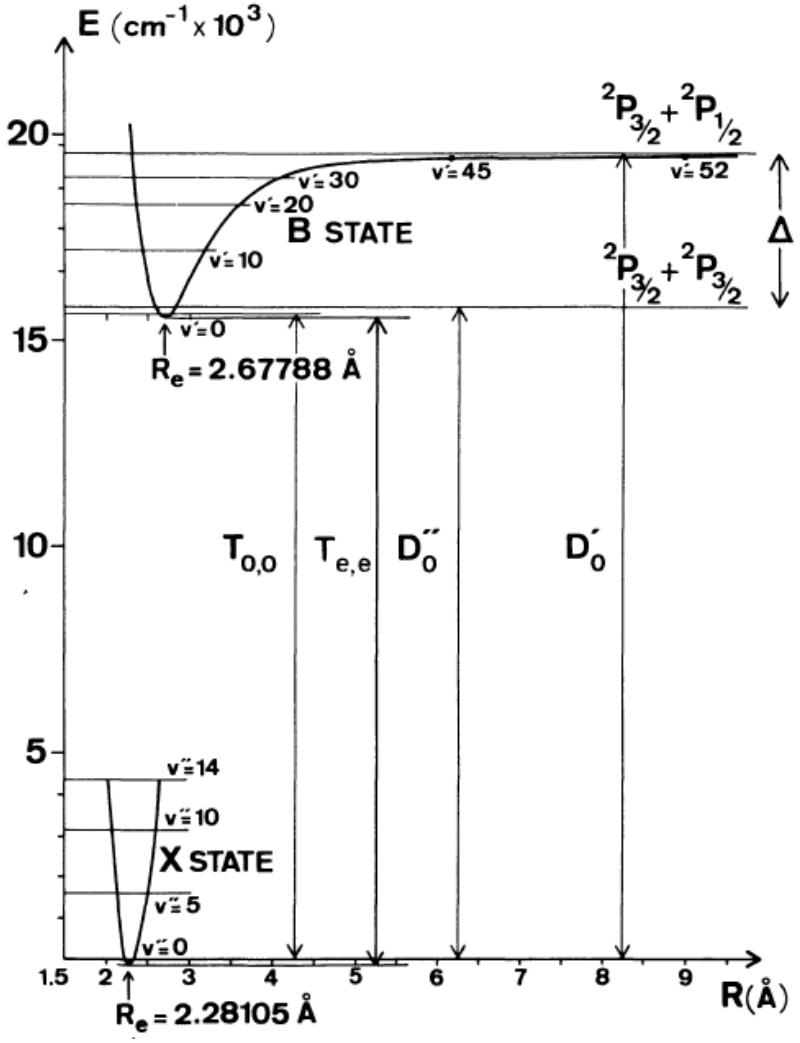

Figure 3.4. Potential energy curves deduced from Fourier transform data. *X* state: quantum mechanical potential (IPA potential) up to v" = 14. *B* state: RKR potential up to v' = 52. Values of D_c', D_c" and $T_{e,e}$ are equal to 3839.592, 16056.926, and 15902.480 cm^{-1} respectively. The values of $T_{0,0}$, the dissociation limits D_0' and D_0" are different for each of the considered isotopic species $^{79}Br_2$, $^{79,81}Br_2$, and $^{81}Br_2$.[12]

The data from Gerstenkorn and Luc allows for the calculation of the energies and frequencies for all the rotational-vibrational transitions for the vibrational levels investigated, $0 \leq v" \leq 14$ and $0 \leq v' \leq 52$. For a room temperature sample of bromine, these levels allow the calculation of expected resonances for ω_1 in HRC2DS and HRC3DS, since that resonance likely involves a low

value of v", and any value of v'. This is also true for calculating the expected output frequency ω_4. However, the resonant frequencies ω_2 and ω_3 will likely involve higher values of v" than were investigated by Gerstenkorn and Luc.

In 2000, Focsa, Li, and Bernath[13] published findings from their Laser Induced Fluorescence (LIF) spectrum of the $B\ ^3\Pi_{0+u} - X\ ^1\Sigma_g^+$ system in Br_2 also recorded by Fourier Transform Spectroscopy. They resolved ~1800 lines originating from the $10 \leq v' \leq 22$ levels of the $B\ ^3\Pi_{0+u}$ state, involving the $2 \leq v" \leq 29$ levels of the $X\ ^1\Sigma_g^+$ ground state for all three isotopologues of Br_2. These findings, along with the findings from Gerstenkorn and Luc, allowed them to improve upon the Dunham parameters for the ground state, making them applicable for a larger range of v". This data allows for a complete picture of most of the rotational-vibrational transitions in the $B\ ^3\Pi_{0+u} - X\ ^1\Sigma_g^+$ system in Br_2, and indeed this data was used for the purpose of simulating and verifying the signal from the both the HRC2DS and HRC3DS experiments.

Using the Dunham parameters from the works of Gerstenkorn and Luc[12] and Focsa, Li, and Bernath[13], a database was generated and a simple program created to identify fully resonant peaks in the HRC3DS spectra. All the rotational-vibrational transitions for the quantum numbers $0 \leq v" \leq 34$, $0 \leq J" \leq 101$, $0 \leq v' \leq 40$, $0 \leq J' \leq 101$ in the $B\ ^3\Pi_{0+u} - X\ ^1\Sigma_g^+$ system for all three isotopologues of bromine were calculated. The "target" signal that was initially investigated was for $\omega_1 = 16330.86\ cm^{-1}$ which corresponds to the v" = 1, J" = 62 to v' = 6, J' = 61 resonance for $^{79,81}Br_2$ for the $B\ ^3\Pi_{0+u} - X\ ^1\Sigma_g^+$ system. These calculations allowed for the identification of other series of data whose ω_1 resonances were within the linewidth of the fixed narrowband input laser, as will be discussed in the results. Most of the accumulated data agreed with the calculated transitions within $> 0.5\ cm^{-1}$.

3.3 Developing HRC2DS

There are several advantages when comparing HRCMS to one dimensional spectroscopies. One dimensional spectroscopies can yield spectra that are very congested, for example an absorption spectrum of bromine gas at room temperature in the $\lambda = 514$ nm region can have up to 1000 absorption lines per nanometer, partly due to the presence of several isotopologues. Cooling the sample, perhaps by means of supersonic expansion, can aid in reducing this congestion, but at a loss of information, in this case it would be rotational information. The FWM techniques employed by HRC2DS and HRC3DS allow the output signal, called ω_4, to be plotted as a function of one of the input frequencies. The result is a reduction in peak density, from possibly hundreds to thousands of peaks per nanometer in one dimensional spectroscopies, to tens of peaks per square nanometer in HRC2DS, to several peaks per square nanometer in HRC3DS. Figure 3.5 shows this effect with respect to a one-dimensional absorption spectrum of bromine being expanded into two dimensions using one of the HRC2DS techniques, in this case 2D coherent double resonance electronic (CDRE) spectroscopy.[14] The spectra in Figure 3.5 were simulated in Mathcad using spectroscopic constants from references 10 and 12.

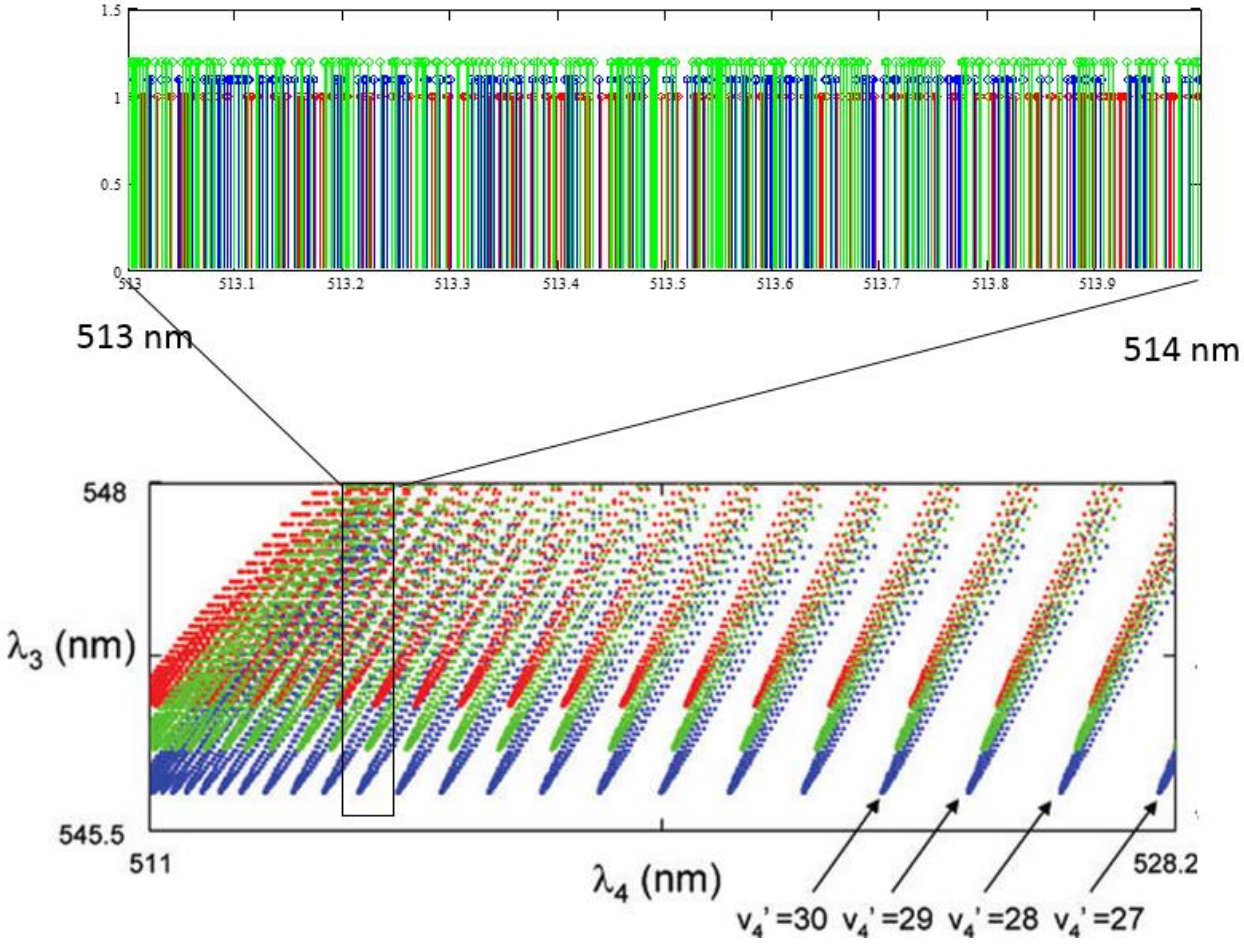

Figure 3.5. Top: 1D absorption spectrum of naturally occurring bromine (blue represents signal from $^{79}Br_2$, green represents $^{79,81}Br_2$, and red represents $^{81}Br_2$). Bottom: 2D CDRE spectrum of bromine with the above 1D section indicated. Peak separation and ordering are a result of the HRC2D technique.

3.3.1 RECARS and CDRES

Peter Chen and coworkers[14] employed several coherent, two-dimensional techniques from about 2004-2012, including work on molecules such as Br_2 and NO_2. In the case of Br_2, the techniques were called 2D resonantly enhanced coherent anti-Stokes Raman spectroscopy (RECARS) and 2D CDRE spectroscopy. The names these techniques were given reflect the FWM process that contributed the majority of the signal. Figure 3.6 shows a reproduction of the wave mixing energy level diagram for both.

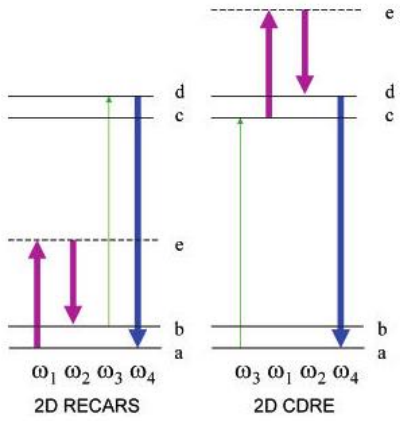

Figure 3.6. Wave mixing energy level diagrams for the FWM processes responsible for the output signal in 2D RECARS and 2D CDRE spectroscopy[14]

The FWM process responsible for 2D RECARS is analogous to process 3 in Figure 3.3, and the FWM process responsible for the 2D CDRE spectroscopy signal is analogous to process 1 in Figure 3.3.

3.3.2 Cluster Patterns in HRC2DS

2D RECARS was abandoned in favor of 2D CDRE spectroscopy (CDRES) for the later studies of Br_2 and for the studies of NO_2 by P. C. Chen and coworkers.[14,15] The output signal from 2D CDRES has clusters of signal that are vertically and horizontally aligned, where the signal from 2D RECARS showed some vertical alignment but no horizontal alignment, which made pattern recognition and thus quantum number assignment more difficult. The 2D CDRES spectra, such as the one simulated in the bottom of Figure 3.5, show two types of regular repeating patterns. First, peaks produced by the same ω_4 vibrational resonance are grouped into clusters that somewhat resemble a parabola. This clustering occurs because the energy separation between rotational levels as well as the rotational selection rules cause the distance between consecutive rotational peaks to be small and relatively consistent. Second, the parabola-shaped clusters seem to be arranged in horizontally and vertically aligned patterns.[3] As seen in the bottom of Figure 5, the vibronic origins or bases of the parabola-shaped clusters are horizontally ordered according to the upper vibrational level in the ω_4 resonance, denoted v_4', which increases as energy increases, or as wavelength decreases. Vertically, the parabola-shaped clusters will be ordered according to the upper vibrational level in the ω_3 resonance, v_3', however in the bottom of Figure 3.5, only the peaks associated with the $v_3' = 25$ resonance have been simulated.[14] As with the horizontal alignment, the vibrational quantum number v_3' will increase as energy increases, or as wavelength decreases.

The parabola shape of the clusters from the 2D CDRES simulation of bromine lend insight to the relationship between the rotational constants for the two electronic states involved in the coherence. If the rotational constants for both states were approximately equal, B' = B",

then the cluster shape would be in the form of an "X" rather than a parabola. Figure 3.7 will help elucidate the reasoning behind this.

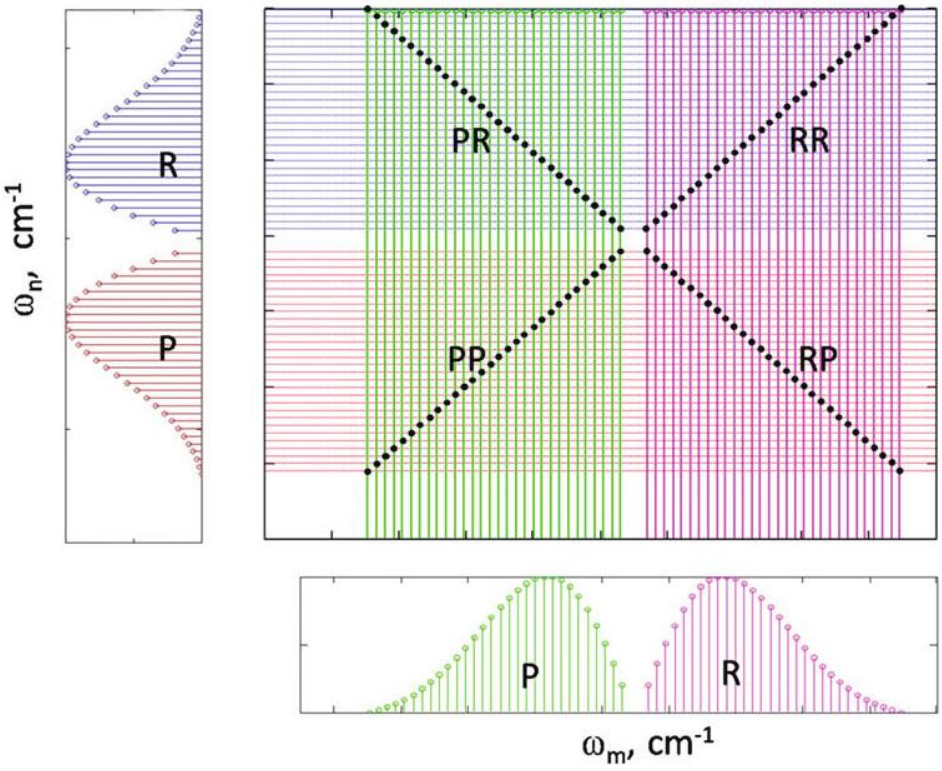

Figure 3.7. Relationship between rotational peaks in conventional 1D spectra (left and bottom), their corresponding vertical and horizontal resonance lines in a 2D spectrum, and their points of intersection. These intersection points that produce CDRES peaks are represented by the black dots and occur only for intersecting resonance lines that have identical J" values.[3]

Along the left and bottom axes of Figure 3.7 are simulated 1D spectra of the interaction of ω_n and ω_m (analogous to ω_3 and ω_4, respectively, in Figure 3.6) with the molecule. The 1D spectra show many resolved rotational lines from a single vibronic transition. As shown on the 2D plot in Figure 3.7, there can be many singly resonant lines present in the 2D spectrum, but since CDRES is a parametric process, doubly resonant peaks will only occur when the J" for the

interaction with ω_n and ω_m are the same. Figure 3.8 gives a representation of the cluster shape when the rotational constant of the two states are not equal.

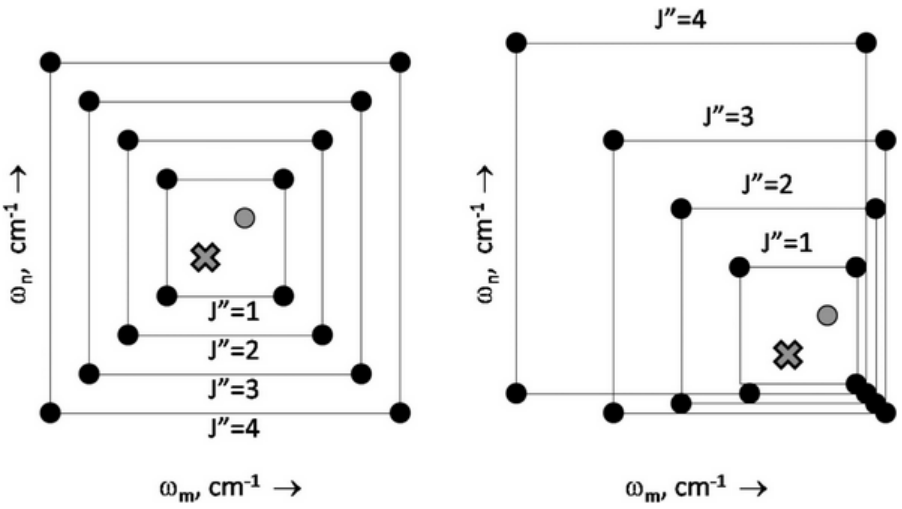

Figure 3.8. Left: predicted shape of a cluster formed by CDRES, assuming B' = B" for both axes and a rotational selection rule of $\Delta J = \pm 1$. Only a few J" values are shown here; higher values follow the same pattern. Four peaks with identical J" values form a box. Near the center, the grey point is the solitary J" = 0 peak and the X marks the location of the vibronic origin. Right: similar features for a cluster that is parabolic because B' ≠ B" for both axes (B' > B" along the ω_n axis and B' < B" along the ω_m axis).[3]

Putting the information from Figures 3.7 and 3.8 together; for a cluster where B' = B", the four doubly resonant peaks formed by singly resonant lines from the ω_m and ω_n axes with identical J" values form concentric squares. Using the rigid rotor model, the distance between peaks within each square should be equal to $4B'(J'' + ½)$ along each axis. The J" = 0 peak is near the center of the cluster but is shifted in both the x- and y-directions by B' from the exact center of the box, and is shifted by 2B' from the rotationless vibronic origin.[3] From this information, and referencing the CDRES simulation of bromine in Figure 3.5, one can deduce that B' < B" along both the ω_m and ω_n axes for bromine.

The signal acquisition in the studies of Br_2 and NO_2 by 2D CDRES was aided by a technique called multiplexing. In a typical 2D CDRES experiment, and this applies for many coherent two-dimensional spectroscopies, the resultant FWM signal is monitored while one of the input field frequencies is scanned, while the other input field frequencies are held constant. If one or more of the input frequencies is from a broadband laser source, then entire spectra can be taken each laser shot, since many resonances within the sample will be present in the broadband field. With multiplexing, the output frequencies must be spectrally resolved, in this case using a monochromator, multi-channel array detector, and CCD camera that will be described further later on.[1] For all HRC2DS techniques employed by Chen and coworkers, two of the three input fields involved in the FWM processes were from broadband laser sources. Specifically for the 2D CDRES work on Br_2 and NO_2, referring to Figure 3.5, the fields denoted ω_1 and ω_2 were from a broadband source, while ω_3 was the narrowband source that was scanned during the experiment.[14] Broadband multiplexing dramatically decreases the acquisition time that would be necessary to complete 2D and 3D spectra, especially in the case of the 2D experiments since two of the input fields are from broadband laser sources. Since the HRC3DS technique employs only one broadband source as an input field, while holding another narrowband source fixed and scanning a third narrowband source, the data acquisition time for a spectrum containing the same number of points as an analogous 2D scan would be significantly longer. However, the employment of multiplexing in the 3D case still reduces the data acquisition time by several orders of magnitude.[2]

3.4 Developing HRC3DS

The development of HRC3DS from the two-dimensional analog was spurred on by the results Chen and coworkers found when exploring 2D CDRES experiments on NO_2. Even with the reduction in peak density that the HRC2DS techniques offer, the resultant 2D spectra were still difficult to resolve. There are many vibronic origins in the spectral region that was probed, and sufficiently high rotational quantum numbers are accessed using the technique that it made pattern recognition very difficult.[15] The principle difference between the 2D and 3D version of the techniques is that for 3D, two of the three input fields are narrowband, whereas for 2D, two of the three input fields are from a single, broadband source.

The first experiments employing HRC3DS used bromine as the model molecule. As mentioned earlier, bromine has a well-studied main system, attributed to the transition $B\,^3\Pi_{0+u} - X\,^1\Sigma_g^+$.[4] This system was chosen, in part, since the frequencies of the majority of the rotational-vibrational resonances lie in the visible to near-infrared region, making the instrumental requirements for generating the input fields and separating the input fields from the resulting FWM signal more favorable. By controlling two of the three input fields, and knowing something about the energetics of the system being investigated, it is possible to begin deducing which of the FWM processes enumerated in Figure 3.3 are responsible for the resulting output signal. For processes 5-10 in Figure 3.3, one of the input fields would need to involve a near infrared resonance with levels a and c in the figure. The energy associated with this resonance is likely too small to involve anything besides an overtone band within the ground electronic state of the system, and that resonance will be much weaker than one involving two different

electronic states with favorable symmetry. Thus the primary focus of identifying the FWM process centered on processes 1-4, the parametric processes.

3.4.1 Intercluster Patterns

The spectra of bromine generated using the experimental setup described below, consisted of clusters of three peaks, and the clusters themselves were aligned vertically and diagonally when ω_3 from Figure 3.3 is plotted along the y-axis and ω_4 is plotted along the x-axis. By recognizing the intercluster pattern, it is then possible to determine which FWM process is responsible for the signal. Again, the relationship between the intensity of the resultant FWM signal can be expressed as

$$I_{\mathrm{FWM}} \approx I_1 I_2 I_3 \left|\chi^{(3)}\right|^2 \left[\mathrm{sinc}\left(\frac{L\Delta k}{2}\right)^2\right] \quad \text{and} \quad \chi^{(3)} \approx \sum_{i,j,k} \frac{\mu_i \mu_j \mu_k \mu_l}{\Delta_i \Delta_j \Delta_k}$$

where $\Delta_i = \delta_i - i\Gamma$, and δ_i are the difference between the molecular transition frequencies and the input laser frequencies.[3] When the resonance denominators go to zero, or when the input fields are resonant with the molecular transition frequencies, the most intense FWM signal is produced. From Figure 3.3, focusing on processes 1-4, the possible resonance denominators are shown in Table 3.2.

Table 3.2. Resonant denominators from the expression for $\chi^{(3)}$ for the four parametric FWM processes shown in Figure 3, where the ω_{nm} are the molecular transition frequencies and the ω_i are the input or resulting FWM frequencies.

Process 1	Process 2	Process 3	Process 4
$\Delta_{fa} = \omega_{fa} - \omega_1 - i\Gamma_{fa}$	$\Delta_{da} = \omega_{da} - \omega_3 - i\Gamma_{da}$	$\Delta_{da} = \omega_{da} - \omega_3 - i\Gamma_{da}$	$\Delta_{fa} = \omega_{fa} - \omega_1 - i\Gamma_{fa}$
$\Delta_{ha} = \omega_{ha} - (\omega_1 + \omega_3) - i\Gamma_{ha}$	$\Delta_{ha} = \omega_{ha} - (\omega_1 + \omega_3) - i\Gamma_{ha}$	$\Delta_{ba} = \omega_{ba} - (\omega_1 - \omega_4) - i\Gamma_{ba}$	$\Delta_{ea} = \omega_{ea} - (\omega_1 - \omega_2) - i\Gamma_{ea}$
$\Delta_{ga} = \omega_{ga} - \omega_4 - i\Gamma_{ga}$	$\Delta_{ga} = \omega_{ga} - \omega_4 - i\Gamma_{ga}$	$\Delta_{ga} = \omega_{ga} - \omega_4 - i\Gamma_{ga}$	$\Delta_{ga} = \omega_{ga} - \omega_4 - i\Gamma_{ga}$

Beginning with the first resonance denominator of process 1, in the experiments being investigated ω_1 is set to a transition frequency in the molecule and is held constant for the length of the scan. Thus the entire 2D plane created when plotting ω_3 vs ω_4 is resonant with $\omega_{fa} = \omega_1$. The second resonance denominator requires ω_3 to equal $\omega_{ha} - \omega_1$, which would result in a horizontal resonance line in the 2D plane when plotting ω_3 vs. ω_4. The final resonance denominator for process 1 requires $\omega_4 = \omega_{ga}$, which would result in a vertical resonance line in the 2D space when plotting ω_3 vs. ω_4. Thus periodically, when $\omega_3 = \omega_{ha} - \omega_1$ simultaneously as $\omega_4 = \omega_{ga}$, a fully resonant cluster of peaks will appear, and those clusters will be aligned vertically and horizontally. This analysis is supported by the 2D work done by Chen and coworkers when they observed the clusters for 2D CDRES, whose FWM process is analogous to process 1, were aligned vertically and horizontally.[14]

For process 2, there are two resonance denominators that are identical to the ones in process 1. However the third resonance denominator requires ω_3 to equal ω_{da} to achieve resonance. It is a rare and coincidental occurrence when $\omega_3 = \omega_{ha} - \omega_1 = \omega_{da}$ simultaneously, and thus fully resonant clusters of peaks are uncommon for process 2. Similarly for process 3, two of

its resonance denominators have been analyzed, however the third will require ω_4 to equal $\omega_{ba} - \omega_1$ to achieve resonance. Again, since ω_4 needs to equal $\omega_{ba} - \omega_1$ and ω_{ga} simultaneously, it will be rare to see fully resonant signal in this experiment from process 3.

Process 4 has two resonance denominators in common with process 1, and the third requires ω_{ea} to equal $\omega_1 - \omega_2$ to achieve resonance. From Figure 3 we can see that energetically $\omega_1 - \omega_2$ is equivalent to $\omega_4 - \omega_3$, which would result in a diagonal resonance line with slope equal to one in the 2D plane created when plotting ω_3 vs ω_4. Thus periodically, when $\omega_2 = \omega_1 - \omega_{ea}$ simultaneously as $\omega_4 = \omega_{ga}$, a fully resonant cluster of peaks will appear, and those clusters will be aligned vertically and diagonally. It is therefore likely that the FWM process responsible for the majority of the fully resonant signal in this experiment is process 4.

The HRC3DS experiments were designed such that the three input fields responsible for producing the output FWM signal from the sample are from two narrowband lasers and one broadband OPO. It is possible to hold ω_1 and scan ω_3 as has been described above, however it is also possible to conduct the experiment holding ω_3 constant and scanning ω_1. The resonance denominators from Table 3.2 are accurate regardless of which narrowband laser is fixed or scanned, however the intercluster patterns that result from each process will be different. Looking at the first resonance denominator for processes 2 and 3, since ω_3 is set to a molecular frequency and is held constant for the length of the scan, the entire 2D plane created when plotting ω_1 vs. ω_4 is resonant with $\omega_{da} = \omega_3$. Process 2 will yield fully resonant signal when $\omega_1 = \omega_{ha} - \omega_3$ and when $\omega_4 = \omega_{ga}$, resulting in clusters that are aligned vertically and horizontally in the plane ω_1 vs. ω_4. For process 3 to yield fully resonant signal, $\omega_2 = \omega_3 - \omega_{ba}$ and $\omega_4 = \omega_{ga}$, which yields clusters that are aligned vertically and diagonally in the plane created when plotting ω_1 vs. ω_4.

When holding ω_3 constant and scanning ω_1, processes 1 and 4 do not have a term in Table 3.2 that makes the entire 2D plane of ω_1 vs. ω_4 yield resonant signal. Process 1 requires $\omega_1 = \omega_{fa}$ simultaneously as $\omega_1 = \omega_{ha} - \omega_3$ for the output signal to be fully resonant, which will not happen often and as a result will not generate regularly repeating patterns of clusters of peaks. For process 4 to result in fully resonant signal, ω_4 must equal both ω_{ga} simultaneously as $\omega_{ea} + \omega_3$, which is a rare occurrence and therefore will also not display regularly repeating clusters. It is interesting to note that when setting ω_1 equal to a molecular transition and holding it constant while scanning ω_3, process 1 yields the same pattern as process 2 does when setting ω_3 equal to a molecular transition and holding it constant while scanning ω_1. Similarly, process 3 while holding ω_3 constant and scanning ω_1 will yield the same pattern as process 4 does when holding ω_1 constant and scanning ω_3. Figure 3.9 shows the resonance lines present in each of the two cases, holding ω_1 constant while plotting ω_3 vs. ω_4, and holding ω_3 constant while plotting ω_1 vs. ω_4. The resulting intercluster patterns are also summarized.

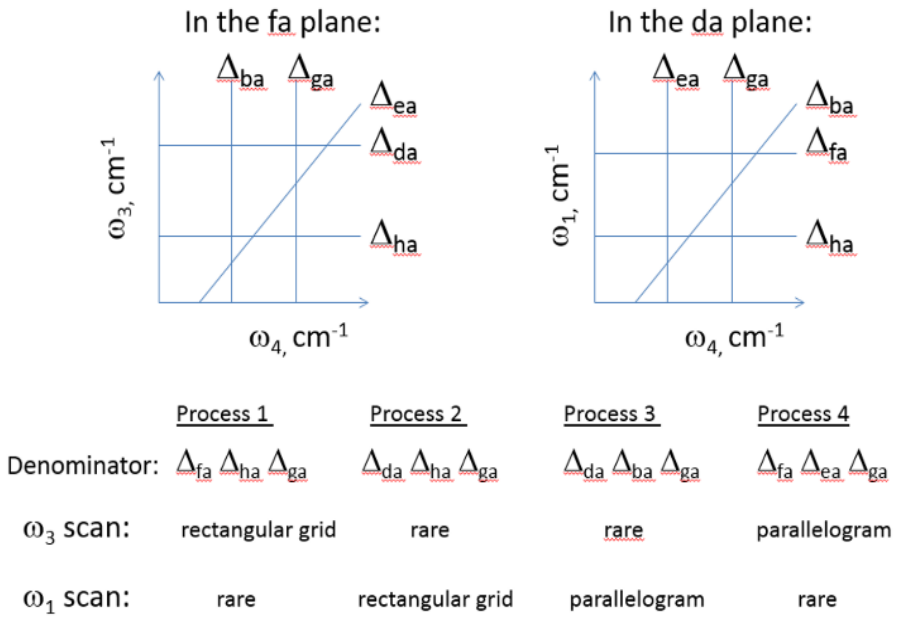

	Process 1	Process 2	Process 3	Process 4
Denominator:	Δ_{fa} Δ_{ha} Δ_{ga}	Δ_{da} Δ_{ha} Δ_{ga}	Δ_{da} Δ_{ba} Δ_{ga}	Δ_{fa} Δ_{ea} Δ_{ga}
ω_3 scan:	rectangular grid	rare	rare	parallelogram
ω_1 scan:	rare	rectangular grid	parallelogram	rare

Figure 3.9. Resonance vibrational patterns for the four parametric processes. The bottom two rows indicate the shape of the vibrational pattern ("rare" indicates that triple resonances are so infrequent that a regular repeating pattern may not be produced).[2]

3.4.2 Intracluster Patterns

The intracluster patterns that result from process 1 and process 4 for a scan in which ω_1 is tuned to a molecular transition and held fixed while ω_3 is scanned, are well explained in the work of Strangfeld, Wells, and Chen[2] which is included in the next chapter. Briefly, the FWM process responsible for the signal in the HRC3DS experiment is a parametric process. In the experiment for bromine, process 4 is responsible for the resultant FWM signal, but process 1 is also examined. Being parametric processes, the initial state must be the same as the final state, which

means the initial v" and J" must be the same as the final. Using the rotational selection rule $\Delta J = \pm 1$, this constricts the number of transitions possible for each resonance in the FWM process, since ω_1 is set to a specific molecular transition frequency and held constant. When ω_1 is tuned to a P-type transition in the molecule, three transitions are allowed via the selection rule, and three fully resonant peaks result in each cluster of signal. When ω_1 is set to an R-type transition, a different set of three peaks is the result. For process 4, two of the peaks in the P-type cluster are identical to two of the peaks in the R-type cluster, where as in process 1, all six peaks have unique resonant frequencies. By approximating the rotational energy with the simple rigid rotor formula, $E_J = B_v J(J + 1)$, it is possible to get an estimated relationship between the locations of the peaks within the cluster. Figure 3.10 summarizes the intracluster patterns for processes 1 and 4 when ω_1 is tuned to a molecular transition and held fixed while ω_3 is scanned, and also shows the relationship between the location of the peaks relative to each other in terms of the rotational quantum number J", and the vibrational constant for the relevant level in the FWM diagrams from Figure 3.3, B_v.

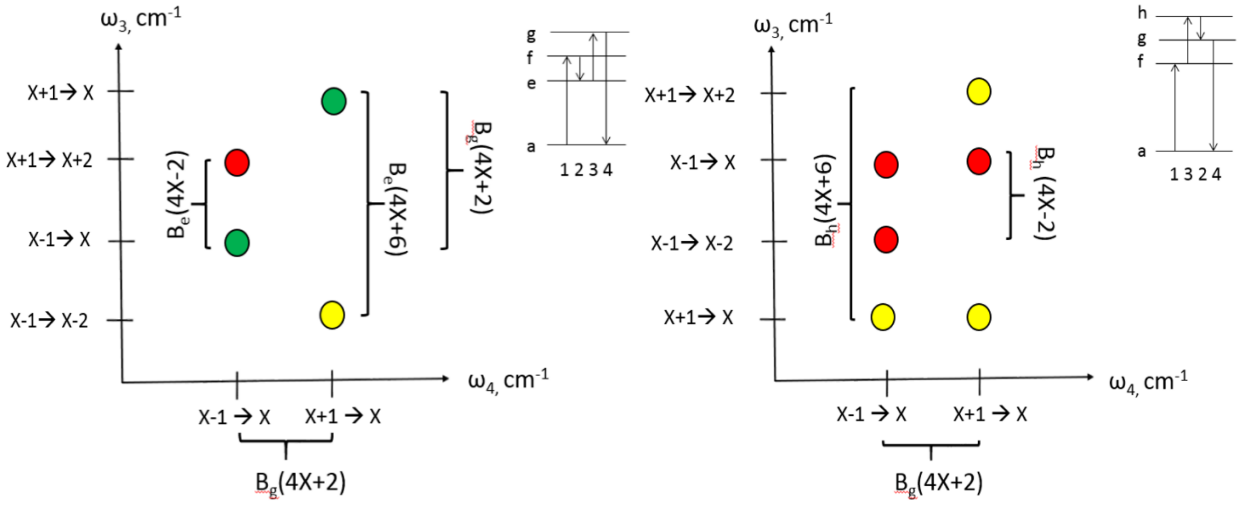

Figure 3.10. Intracluster patterns that result when ω_1 is fixed and ω_3 is scanned. Process 4 pattern is shown on the left and process 1 on the right. The green peaks are shared by both the P- and R-type cluster, while the yellow peaks are unique to the R-type pattern, and the red peaks are unique to the P-type pattern. The B_v's reference the vibrational level from the FWM diagrams, reproduced from Figure 3, and X has replaced J".[2]

In the experiments where bromine has been investigated using HRC3DS, the intensity of the peaks that result from the FWM signal have not been thoroughly analyzed, besides setting a baseline threshold below which peaks are removed from the analysis. This is due in part to some limitations in the experimental equipment; at times the input laser intensities and temporal overlap of the fields could not be maintained to the point where an intensity-dependent analysis would not have yielded much practical information. The intensity of the resultant FWM signal is dependent upon many factors, one being the concentration of the gas-phase sample being investigated. By using ω_1 to select a certain molecular transition frequency, it seems reasonable that a concentration analysis would be possible with accurate intensity data, perhaps even to the point of detecting trace compounds in a mixture. For a single species, examining the intensity of

the FWM peaks should also give some idea as to the degree of correlation between the two frequency axes.

3.5 References

[1]J. C. Wright, *Annu. Rev. Phys. Chem.* **62**, 209 (2011).

[2]B. R. Strangfeld, T. A. Wells, and P. C. Chen, *submitted for publication* (2014).

[3]P. C. Chen, *J. Phys. Chem. A* **114**, 11365 (2010).

[4]H. Kuhn, *Z. Phys*. **39**, 77 (1926).

[5]W. G. Brown, *Phys Rev.* **39**, 777 (1932).

[6]R. S. Mulliken, *Phys Rev.* **46**, 549 (1934).

[7]J. A. Horsely and R. F. Barrow, *Trans. Faraday Soc.* **63**, 32 (1967).

[8]J. A. Coxon, *J. Mol. Spectrosc.* **37**, 39 (1971).

[9]R. F. Barrow, T. C. Clark, J. A. Coxon, and K. K. Yee, *J. Mol. Spectrosc.* **51**, 428 (1974).

[10]S. Gerstenkorn, P. Luc, A. Raynal, and J. Sinzelle, *J. Phys. (France)* **48**, 1685 (1987).

[11]J. L. Dunham, *Phys. Rev.* **41**, 721 (1932).

[12]S. Gerstenkorn and P. Luc, *J. Phys. (France)* **50**, 1417 (1989).

[13]C. Focsa, H. Li, and P. F. Bernath, *J. Mol. Spectrosc.* **200**, 104 (2000).

[14]P. C. Chen and M. Gomes, *J. Phys. Chem. A* **112**, 2999 (2007).

[15]P. C. Chen and K. Mitchell, *J. Chem. Phys.* **129**, 194301 (2008).

Chapter 4

4. Rotational and Vibrational Pattern Interpretation for High Resolution Coherent 3D Spectroscopy and Analysis of Bromine

High-resolution coherent multidimensional spectroscopy provides an alternative to conventional methods for generating rotationally resolved electronic spectra of gas phase molecules. In addition to revealing information such as the relationships among peaks, it can provide clearly recognizable patterns for systems that otherwise appear patternless due to rotational congestion. Despite this improvement, high-resolution coherent 2D spectroscopy can still exhibit congestion problems; expansion to the second dimension is often not sufficient to prevent overlapping of peaks from different patterns. A new 3D version of the technique has been developed that can provide improved resolution and selectivity to help address cases with severe congestion. This 3D technique also produces vibrational and rotational peak patterns that are different from the 2D version. These patterns depend upon the scanning strategy and the corresponding four wave mixing process. This chapter provides information on the theory, patterns, and possible ways to use high-resolution coherent 3D spectroscopy.

4.1 Introduction

Coherent two-dimensional[1-6] and three-dimensional spectroscopy[7-15] have gained much attention as analogs to multidimensional NMR that reveal the relationship between peaks in optical spectroscopy. Most coherent multidimensional techniques have been developed for condensed phase systems. However, a high-resolution form using nanosecond lasers and frequency-domain acquisition has been created for gas phase electronic spectroscopy, where severe rotational congestion often causes pattern obscuration.[16] The 2D spectra produced by high-resolution coherent 2D (HRC2D) spectroscopy can show clearly recognizable patterns for systems where other techniques yield seemingly patternless spectra. HRC2D spectra utilize 2D space to show two types of patterns, a vibrational pattern and a rotational pattern, so that vibrational information is spatially distinct from rotational information. Within the patterns, peaks are sorted sequentially by their quantum numbers.[17] The patterns for hot bands are spatially distinguishable from those for cold bands.[18] Patterns from different isotopologues may also appear spatially separated.[19,20] HRC2D is useful for taking spectra of molecules at any temperature, making it suitable for studying systems where rotational information is needed or cryogenic preparation is not feasible.

One key difference between HRC2D spectroscopy and most other forms of high-resolution spectroscopy is the fact that it relies upon resonantly enhancing a coherent optical process rather than creating an excited state population. As a result, the technique is more robust than laser-induced fluorescence, which can be diminished by depopulating effects such as quenching and predissociation. Another key advantage is that the coherent process can be a

parametric form of four wave mixing (FWM). In such cases, light that is coherently generated comes from molecules where the final level is identical to the initial level (i.e., the molecule does not experience a net gain or loss of energy from the input light fields). Unlike most other forms of conventional spectroscopy (absorption, fluorescence, etc.) the initial and final levels of a parametric FWM process will have identical vibrational and rotational quantum numbers. This fact restricts the number of levels that can participate in the creation of light and the types of peaks that subsequently appear in the coherent 2D spectrum. The resulting peaks and patterns are therefore limited in number, freer from congestion, and yet sufficiently rich in information to facilitate a detailed spectroscopic study.

Despite the reduction in congestion made possible by expansion into a second dimension, all of the molecules that have been studied using HRC2D spectroscopy have yielded 2D spectra that show some degree of persistent spectral congestion. It appears that expansion into the second dimension may reduce rotational congestion for gas phase electronic spectroscopy sufficiently for some molecules but not for others. Severe congestion can be expected to be a serious problem for systems containing mixtures, molecules at elevated temperatures, and molecules that are large and/or have mixed states due to conical intersections. In order to address severe congestion problems, a three-dimensional form of high-resolution coherent multidimensional spectroscopy was pursued and has recently been demonstrated.[21] The purpose of this approach is similar to that for 3D NMR: to use the third dimension to further reduce the peak density by several orders of magnitude. In that initial demonstration, several different patterns were observed, but the theory needed to explain them had not yet been developed. For example, it was unclear whether some of the patterns may have been due to different FWM processes, different levels in the same species, or different isotopologues.

The purpose of this chapter is to provide the background and theory needed to understand and use high-resolution coherent 3D (HRC3D) spectroscopy. While HRC2D spectroscopy provides specific advantages over conventional (1D) spectroscopy (e.g., it improves resolution, reveals patterns, and sorts peaks), it lacks the options and flexibility needed when trying to deal with regions in the 2D spectrum that appear highly congested. In addition to improving the resolution by expansion into the third dimension, HRC3D spectroscopy also provides a means for achieving selectivity (i.e., produces spectra that contain peaks from a specific species, quantum number, process, etc.). On the other hand, HRC3D experiments are also more complicated to carry out and 3D spectra can be more challenging to interpret compared to that for HRC2D spectroscopy. Solutions to these challenges are also discussed in this chapter.

4.2 Background

High-resolution rotationally resolved electronic spectroscopy is a powerful technique that can provide exquisitely detailed information on the structure and behavior of gas phase molecules. However, the technique is limited to very small and simple molecules; spectra produced by larger and more complicated molecules have long evaded analysis. In addition to reducing congestion by expanding into a second dimension, HRC2D can help address these problems because the 2D spectra show patterns based upon the relationship between peaks, even for molecules where patterns in conventional (1D) spectra are obscured by severe rotational congestion. Within these patterns, peaks are spatially sorted by quantum number, species, selection rules, hot band vs. cold band, etc. In fact, vibrational and rotational information is

separated into a rotational pattern (where the peaks are sorted by rotational quantum number) and a vibrational pattern (where the rotational patterns and their peaks are sorted by vibrational quantum number). However, coherent 2D spectroscopy is not a panacea; congestion still remains a potential problem in HRC2D spectra, and the technique lacks the flexibility and selectivity needed to further reduce persistent congestion problems. For example, the peaks from all isotopologues of a given species can appear in the 2D spectrum since the technique lacks the ability to provide species selectivity.

Tackling this problem by increasing the dimensionality from 2D to 3D involves an increase in experimental complexity. Additional time is then needed to collect data; a single 3D spectrum consisting of 1000 x 1000 x 1000 points would require a data collection time of more than 30 years if the points are collected at a rate of one point per second. HRC2D experiments involve two broadband near infrared beams in order to achieve dual-broadband multiplexing. Expansion to 3D can be achieved by replacing one of the two broadband near infrared input fields used in HRC2D spectroscopy with an independently tunable laser source. The use of a multichannel array detector, which can be used because one of the input lasers is still broadband, significantly reduces the time required to take 3D data, but it is still considerably longer than the time required to take 2D data.

Careful selection of one of the (narrowband) input beam frequencies can reduce the number of fully resonant FWM processes and therefore help simplify analysis of the resulting HRC3D spectra. Most molecules do not have strong resonances in the near infrared (1000-2000 nm) region. If only one of the input beams is narrowband, tunable, and in the UV or visible region while the other two are in the near infrared region, then the number of possible fully resonant FWM processes can be limited to a small number. As a result, spectral interpretation

will be greatly simplified and the output beam can also be generated in the UV or visible region, allowing use of highly efficient monochromator and CCD systems.

Unlike traditional spectra that are simple xy plots (a plot of a measured quantity as a function of wavelength or frequency), high-resolution coherent multidimensional spectra display the intensity of a beam (produced by four wave mixing) as a function of two or more independent frequencies. For HRC3D spectra, the intensity of the generated beam is a function of *three* independent input frequencies. As a result, it is possible to use resonance patterns to distinguish among singly resonant, doubly resonant, and fully (triply) resonant FWM processes. In a conventional coherent 1D spectrum, peaks may be produced by singly resonant, doubly resonant, or triply resonant FWM processes, and determining the degree of resonance requires additional experimentation or careful lineshape analysis (e.g., modeling coherence interference effects). For coherent 3D spectra, where the peaks reside in three-dimensional space (each orthogonal dimension corresponds to a unique frequency axis), the degree of resonance may be determined by the observed structure (see Table 4.1). Singly resonant processes should produce resonance planes that propagate through 3D space because the same resonance can be maintained by either keeping one of the four fields constant (for a resonance such as $\omega_1 = \omega_{level}$ where the resonance plane would be parallel to the axes for two of the fields) or by keeping the relationship between two fields constant (for a resonance such as $\omega_1 - \omega_2 = \omega_{level}$ where the resonance plane would be diagonal with respect to the axes for two of the fields). Doubly resonant processes should produce resonance lines that propagate through 3D space. Only fully (triply) resonant processes can produce discrete resonance points (peaks) in the 3D space; a triply resonant process requires that all fields have the appropriate wavelengths needed to create a fully resonant four wave mixing process.

Table 4.1. Effect of different degrees of resonance enhancement on multidimensional resonance patterns.

	singly resonant	doubly resonant	fully resonant
conventional 1D spectroscopy	Peak	Peak	Peak
coherent 2D spectroscopy	Continuous line	Peak	Peak
coherent 3D spectroscopy	Continuous plane	Continuous line	Peak

Since displaying the four dimensions of a 3D spectrum is a challenge, the spectra presented in this chapter are 2D slices through the 3D spectrum, where one of the input field frequencies is held constant. If the data is displayed as a 2D slice rather than a complete 3D spectrum, additional slices may be needed in order to confirm the degree of resonance. For example, a doubly resonant process will produce a ridge (due to the resonance line) in a coherent 2D spectrum if the data plane contains the entire double resonance line. If the double resonance line and the plane of the 2D slice intersect, however, then the coherent 2D signal will contain a peak (at that point of intersection) rather than a line. This observation is consistent with the notion that peaks in HRC2D spectra may be caused by doubly resonant or fully resonant processes, and peaks in conventional (1D) coherent spectra may be singly resonant, doubly resonant, or triply resonant.

4.3 Theory

A common challenge in coherent spectroscopy is to identify the appropriate FWM process for setting up an experiment and/or for interpreting experimental results. The use of three independent input beam frequencies (ω_1, ω_2, and ω_3) to produce a FWM signal can result in up to eight possible frequency combinations ($\omega_4 = \pm\omega_1 \pm\omega_2 \pm\omega_3$). For our experiments, only one of the input fields (ω_1) is from a tunable visible (or UV) beam. The other two input fields are in the near infrared region: ω_2 is broadband to facilitate multiplex detection, ω_3 is narrowband and tunable, and $\omega_3 > \omega_2$. As a result, only one frequency combination ($\omega_4 = \omega_1 - \omega_2 + \omega_3$) can be phasematched and generate light that is anti-Stokes of ω_1, a condition that is preferred in order to reduce susceptibility to spectral interference from other processes such as laser-induced fluorescence. Figure 4.1 shows the ten possible FWM processes that can be used to generate coherent light at $\omega_4 = \omega_1 - \omega_2 + \omega_3$. Energy level diagrams 1-4 describe parametric processes (final state = initial state), diagrams 5-7 correspond to one set of nonparametric processes, and diagrams 8-10 correspond to a second set of nonparametric processes. All ten processes have the same phasematching geometry because they all can produce the same output frequency. However, the molecular energy levels that can provide resonance enhancements and produce peaks in the spectra are different. Therefore, the pattern of multidimensional resonance features produced by each will be unique. For a specific molecule and a given set of input wavelengths, some of the FWM processes shown in Figure 4.1 may be fully resonant, while others may be doubly resonant, singly resonant, or non-resonant.

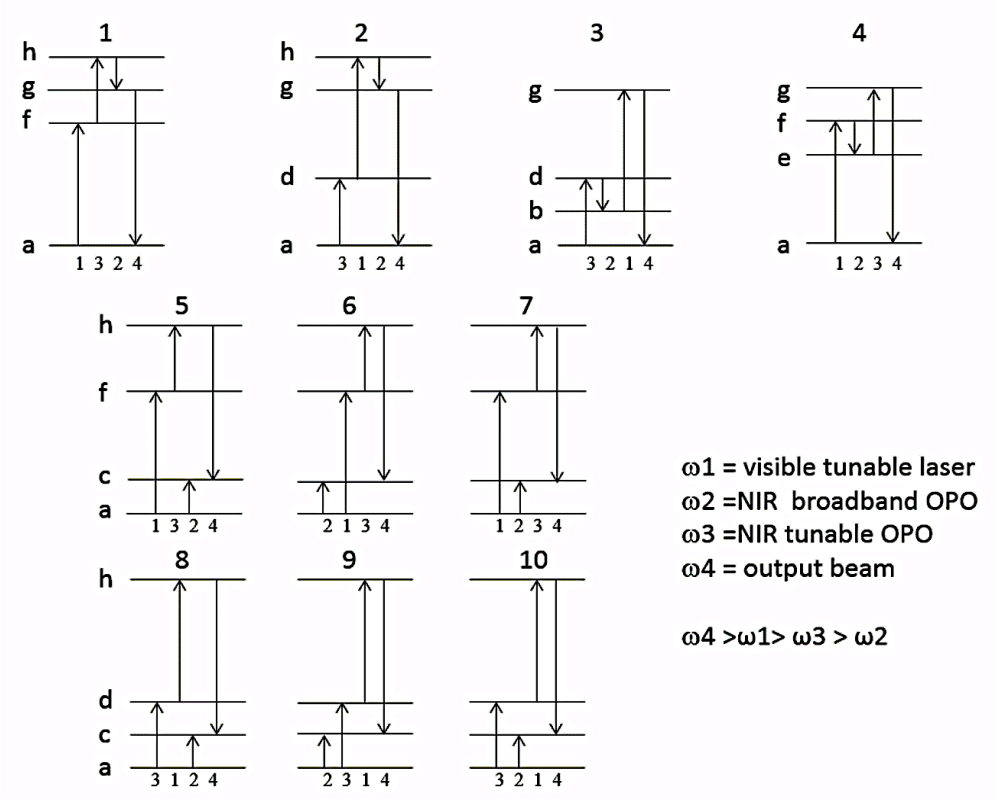

Figure 4.1. FWM diagrams that can produce an output frequency at $\omega_4 = \omega_1 - \omega_2 + \omega_3$

The FWM process responsible for generating the observed peaks must be known in order to design appropriate experiments and to correctly interpret results. During the development of HRC2D spectroscopy, it was discovered that the FWM processes could be determined using the observed vibrational pattern[18]. For example for a typical HRC2D spectrum where ω_1 is plotted on the y-axis and ω_4 is plotted on the x-axis, process 1 in Figure 4.1 produces a rectangular vibrational pattern (showing vertical and *horizontal* alignment), while process 3 in Figure 4.1 produces a parallelogram vibrational pattern with vertical and *diagonal* (rather than horizontal) alignment.

A similar approach would be useful for HRC3D spectroscopy; if available, differences among the rotational and/or vibrational patterns could be used to determine which FWM process is responsible for generating the observed peaks and patterns. But first, it is important to note that some FWM diagrams in Figure 4.1 can be eliminated because they are unlikely to provide a fully resonant FWM process. Since the vast majority of molecules have excited electronic states in the UV or visible region, any resonances involving the broadband near infrared beam (ω_2) and level **a** will usually involve overtones or combination bands that are too weak to provide a significant resonance enhancement. Therefore, none of the nonparametric processes (5 through 10) will be fully resonant. Of the parametric processes, the first and fourth have the best chance of being fully resonant because it is also unlikely that the first photon (ω_3) for processes 2 and 3 will be fully resonant. For process 4, each photon can cause strong interactions if the resonance occurs between levels from different electronic states that have reasonably large Franck-Condon factors. The first photon can match a resonance between a level in the ground electronic state and a level in an excited electronic state. The second, third, and fourth photons can each also cause resonant interactions between the ground and excited electronic states if levels **a** and **e** are in the ground electronic state and levels **f** and **g** are from an excited electronic state. For process 1, two different excited electronic states are needed in order to avoid the harmonic oscillator selection rule of $\Delta v = \pm 1$ for levels in the same electronic state. Therefore, levels **f** and **g** should involve different electronic states from level **a**, and level **h** should involve a different electronic state compared to levels **f** and **g**.

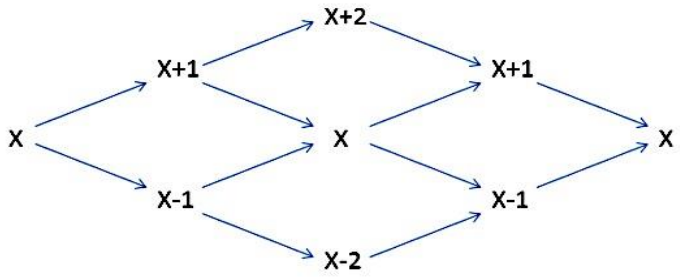

Process 1	Level:	a	f	h	g	a		
	Field:	ω1	ω3	ω2	ω4			
Process 2	Level:	a	d	h	g	a		
	Field:	ω3	ω1	ω2	ω4			
Process 3	Level:	a	d	b	g	a		
	Field:	ω3	ω2	ω1	ω4			
Process 4	Level:	a	f	e	g	a		
	Field:	ω1	ω2	ω3	ω4			

Figure 4.2. Evolution of the rotational quantum number for processes 1-4; X is the initial value for J" at the starting energy level (a). For each process, the level and field (see Figure 4.1) are directly below the corresponding rotational quantum numbers and arrow.

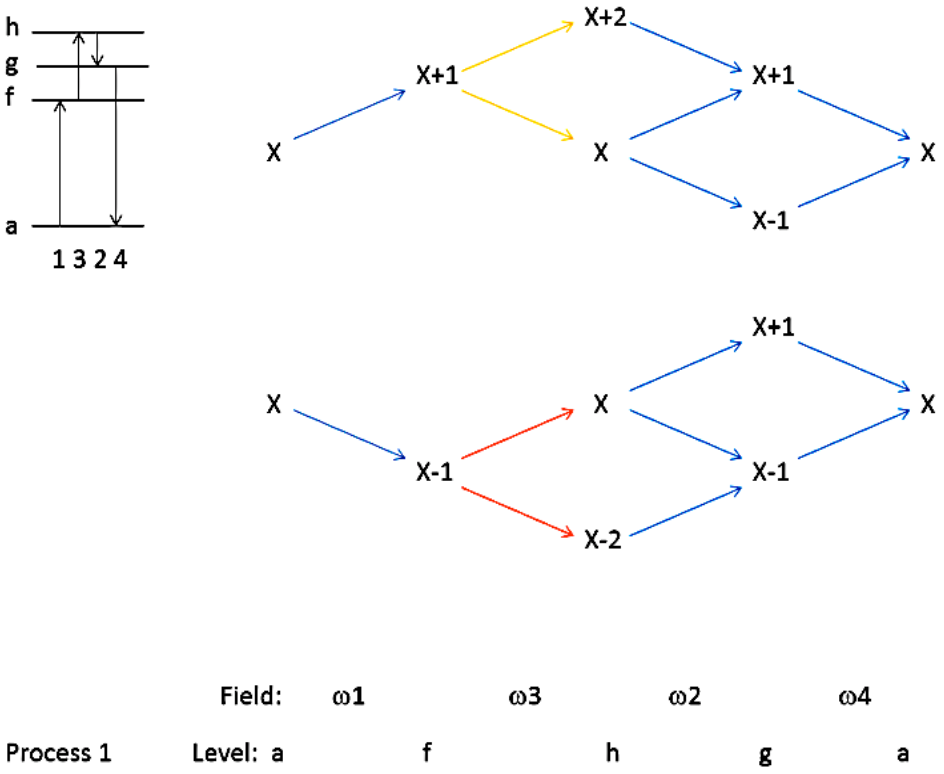

Figure 4.3. Evolution of the rotational quantum number for process 1 when ω_1 is fixed and ω_3 is scanned. The top diagram with yellow arrows is for an R process, while the bottom diagram with the red arrows is for a P process.

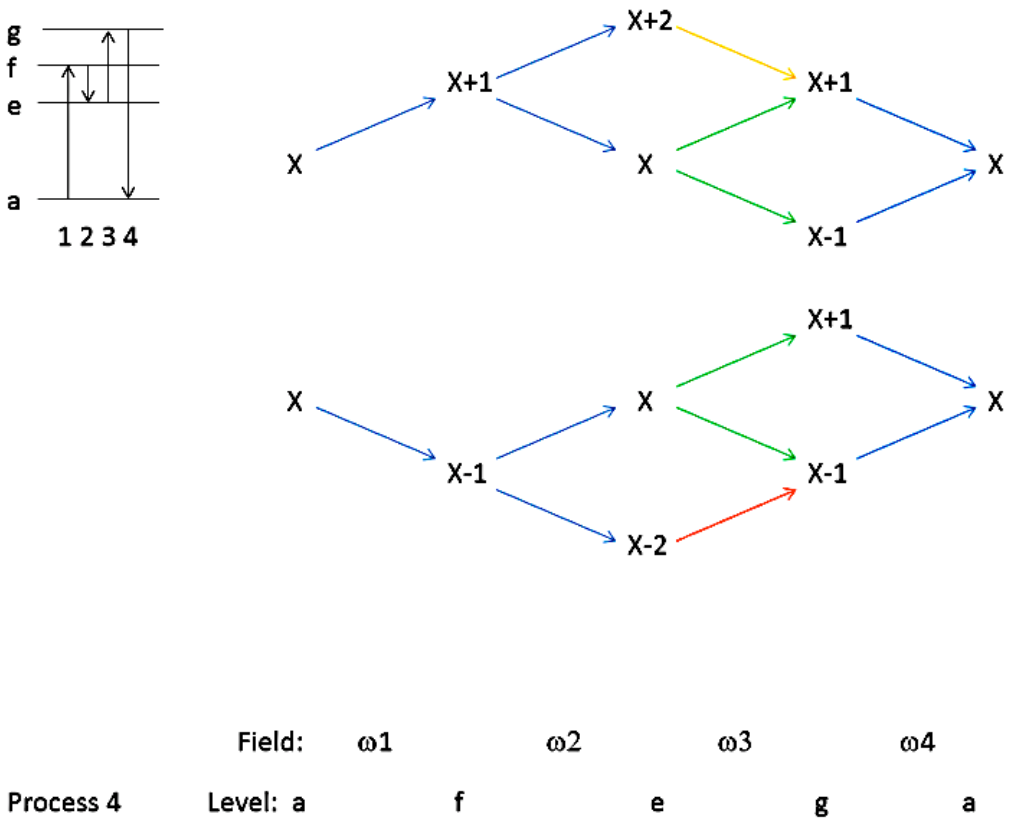

Figure 4.4. Evolution of the rotational quantum number for process 4 when ω_1 is fixed and ω_3 is scanned. The top diagram is for an R process and the bottom diagram is for a P process.

The next step is to determine the rotational pattern produced by each FWM process. For parametric processes 1-4, the rotational quantum numbers can evolve according to the diagram shown in Figure 4.2, which is based upon a selection rule of $\Delta J = +/-1$. In this Figure, X represents the starting value of J". Since ω_2 is broadband and ω_4 is always spectrally dispersed and analyzed, the two choices for creating a 2D slice are to scan ω_3 (while keeping ω_1 fixed) or to scan ω_1 (while keeping ω_3 fixed). For processes 1 and 4, if ω_1 is fixed, the first photon can either decrease J by one unit (a P-type resonance) or it can increase it by one unit (an R-type resonance). Figure 4.3 shows both cases during the evolution of the rotational quantum number

for process 1 when ω_1 is fixed and ω_3 is scanned. Figure 4.4 shows the same type of diagram for process 4. For both cases, there are two possible values for ω_4, so the corresponding rotational patterns shown in Figures 4.5 and 4.6 indicate two possible resonances on the x-axis. Process 4 has four possible values of ω_3, three for the P-type process (the red and green peaks in Figure 4.5) and three for the R-type process (the yellow and green peaks). The two green peaks are common for both the P-type process and the R-type process, and the presence of a sole peak (not paired with another peak that has the same x-axis value) on the right or left immediately reveals whether ω_1 involves a P-type or R-type resonance. The y-axis position of the red and yellow peaks relative to the green peaks depends upon the relationship between the rotational constants. The relative y-axis positions drawn in this figure assume that the $B_e = B_g$, where B_e represents the rotational constant for level **e** and B_g represents the rotational constant for level **g**. The positions on the y-axis correspond to the following ω_3 resonances (the values below show the change in the rotational quantum number from level **e** → level **g**):

A X-2 → X-1

B X → X+1

C X → X-1

D X+2 → X+1

Process 1 also has four possible values of ω_3, but according to Figure 4.3, two are exclusively P-type (red in Figure 4.6) and the other two are only for the R-type (yellow). Unlike that for process 3, the P-type and R-type patterns for process 1 have no peaks in common. The relative y-axis positions drawn in this figure assume that the $B_f = B_h$. Again, the sole peak on the right

indicates a P-type pattern and a sole peak on the left indicates an R-type pattern. However, the process 4 pattern provides an additional advantage over the process 1 pattern; the duplicate green peaks may facilitate the pairing of P-type and R-type patterns that have the same initial J" value when comparing different 2D slices of the 3D spectrum.

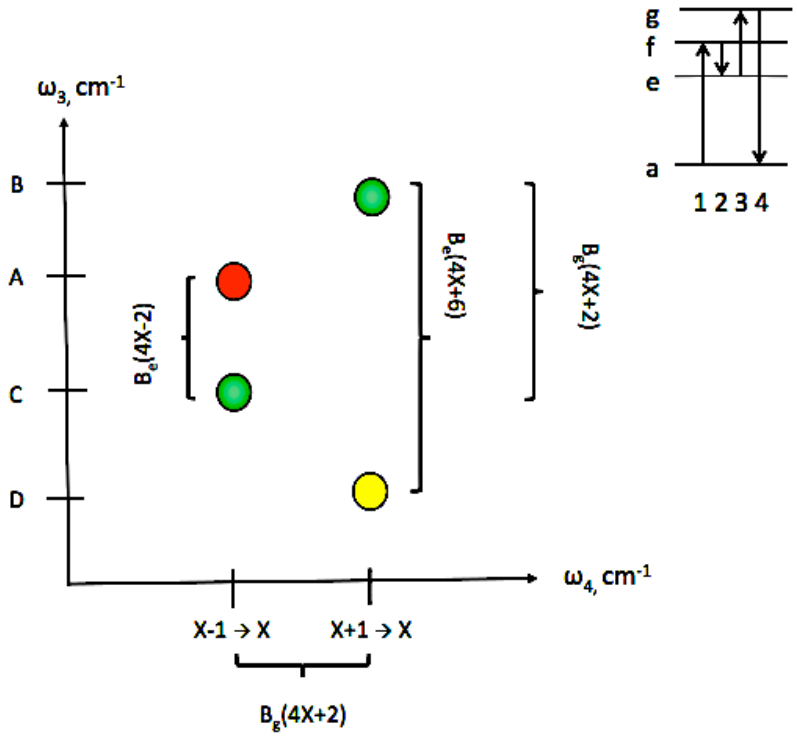

Figure 4.5. Process 4 rotational pattern (ω_1 fixed, ω_3 scanned). The yellow peak is part of the R-type pattern (see Figure 4.3), the red peak is part of the P-type pattern, and the green peaks are common to both R-type and P-type patterns.

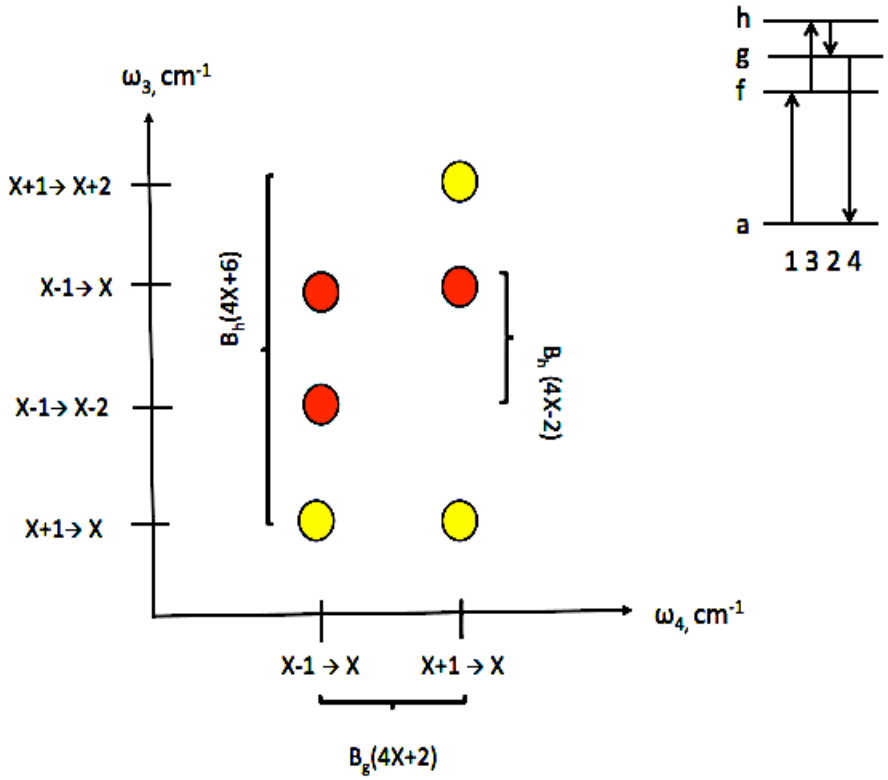

Figure 4.6. Process 1 rotational pattern (ω_1 fixed, ω_3 scanned): the yellow peaks make up the R-type pattern and the red peaks comprise the P-type pattern.

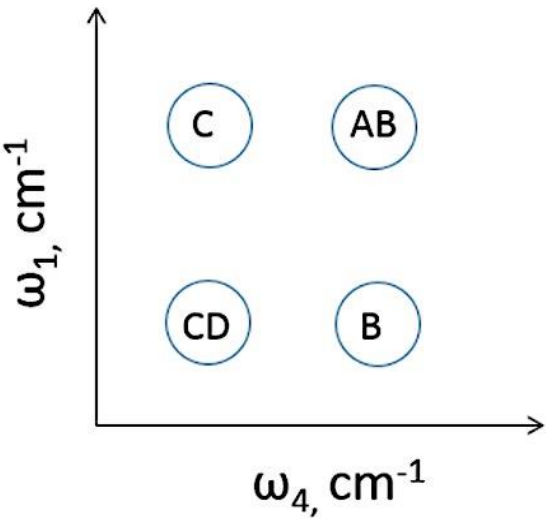

Figure 4.7. Process 4 rotational pattern where ω_3 is fixed and ω_1 is scanned. Four different kinds of rotational patterns (A-D) may be observed: A and D produce a single peak, while B and C each produce a pair of peaks that have the same x-axis value.

The situation is strikingly different when ω_3 is fixed and ω_1 is scanned for process 4. Examples of four different kinds of patterns (A-D) for this situation are shown in Figure 4.7. As observed earlier in Figure 4.5, there are two possible resonances for ω_4 and four possible resonances for ω_3. Each of these four possible ω_3 resonances (A-D in Figure 4.5) will now produces a different kind of rotational pattern; setting ω_3 to A or D yields a single peak, while setting it to B or C yields a pair of vertically aligned peaks. When combined, the four possible peaks shown in Figure 4.7 are similar to that observed in HRC2D spectroscopy, where both ω_2 and ω_3 are broadband. Since ω_3 is narrowband and fixed in HRC3D spectroscopy, no more than

one of those four possible patterns can exist during a given scan. This kind of scan therefore has the disadvantage that the rotational patterns contain only one or two peaks and may therefore be more difficult to identify; a repeating pattern of three peaks is probably easier to recognize than a repeating pattern of just one or two peaks, especially when the number and/or density of peaks (from other molecules and/or processes) is high.

The predicted rotational patterns for all four parametric processes and both types of scans are summarized in Table 4.2. The case where the rotational pattern consists of just one or two peaks is expected for half of the cases, (ω_3 scan for processes 2 and 3, or ω_1 scan for processes 1 and 4), and the easier-to-find pattern of three peaks that form the shape of a triangle is found for the remaining cases (ω_3 scan for processes 1 and 4, or ω_1 scan for processes 2 and 3). Since processes 1 and 4 are the most likely to be fully resonant, the best general strategy for creating 2D slices appears to be keeping ω_1 fixed while scanning ω_3.

Table 4.2. Rotational patterns for parametric FWM processes.

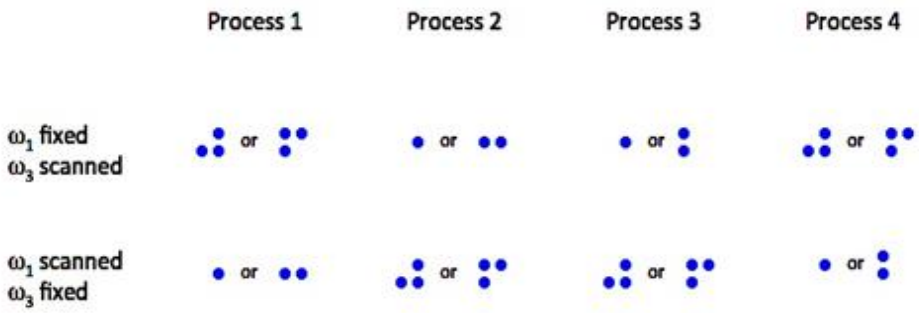

In addition to the rotational pattern, the vibrational pattern in the 2D slice of a HRC3D spectrum can also be used to determine the FWM process. The equations for the two candidates

most likely to be fully resonant (processes 1 and 4) can be generated using density matrix diagrams, and the simplified expressions are:

$$\chi^{(3)}_1 = \xi \left(\Delta_{fa} \Delta_{ha} \Delta_{ga} \right)^{-1}$$

$$\chi^{(3)}_4 = \xi \left(\Delta_{fa} \Delta_{ea} \Delta_{ga} \right)^{-1}$$

where the ξ is the product of transition dipole moments for the four fields and the Δ's are resonance denominators:

$$\Delta_{ea} = \omega_{ea} - (\omega_1 - \omega_2) - i\Gamma_{ea}$$

$$\Delta_{fa} = \omega_{fa} - \omega_1 - i\Gamma_{fa}$$

$$\Delta_{ga} = \omega_{ga} - \omega_4 - i\Gamma_{ga}$$

$$\Delta_{ha} = \omega_{ha} - (\omega_1 + \omega_3) - i\Gamma_{ha}$$

Figure 4.8 shows the kinds of resonance lines that these resonant denominators will generate for a coherent 2D slice of the HRC3D spectrum. First consider the situation where ω_3 (narrowband NIR beam) is tuned while the UV-visible input laser frequency (ω_1) is fixed. If ω_1 has been tuned to a resonance, then the left side of the diagram in Figure 4.8 is in the Δ_{fa} plane, so that $\Delta_{fa} = -i\Gamma_{fa}$. The equations for processes 1 and 4 both include a Δ_{fa} denominator, which results in one resonance. For process 1, two additional resonances occur at the intersection between resonance lines Δ_{ha} (horizontal) and Δ_{ga} (vertical). Therefore, a triple resonance situation occurs at the

intersection of these two perpendicular lines within the Δ_{fa} resonance plane. In the harmonic oscillator approximation, Δ_{ha} and Δ_{ga} will each produce a set of somewhat regularly spaced horizontal and vertical lines (each with separate vibrational quantum numbers). Therefore, the triply resonant vibrational patterns will be regularly spaced as well, forming a rectangular grid of rows and columns. For a simple diatomic molecule, the distance between rows will be roughly equal and the distance between columns will also be roughly equal because of the roughly equal spacing between vibrational levels. Polyatomic molecules will appear more varied due to the existence of 3N-5 or 3N-6 vibrational modes, but the pattern should still show a recognizable rectangular vibrational pattern with repeating x-axis and y-axis values.

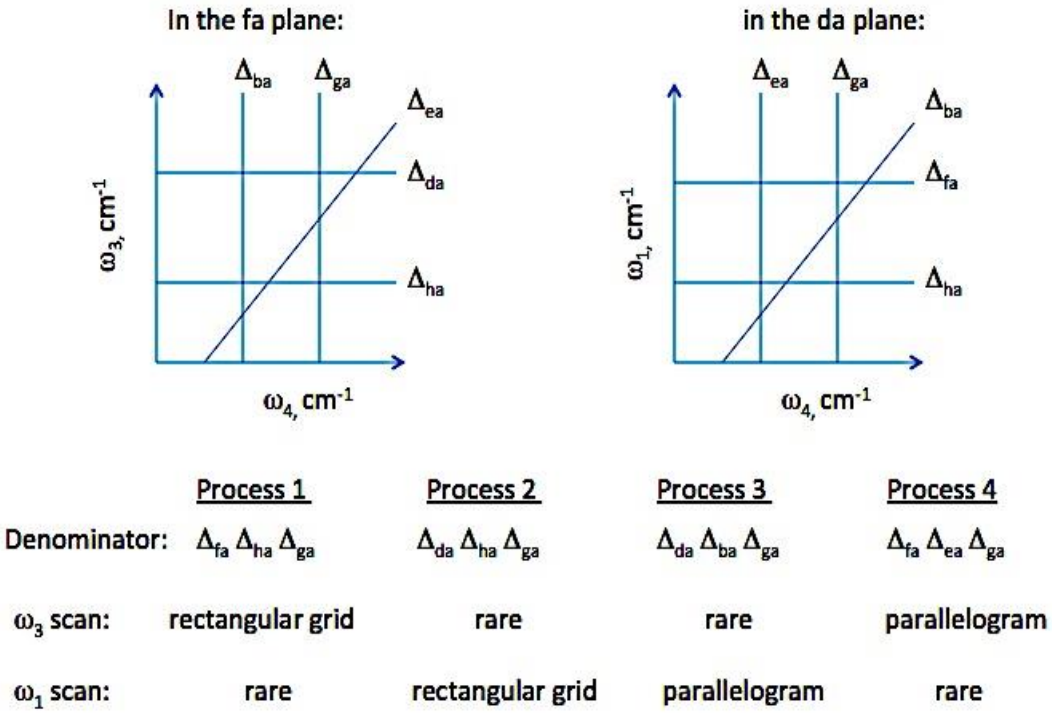

	Process 1	Process 2	Process 3	Process 4
Denominator:	$\Delta_{fa}\,\Delta_{ha}\,\Delta_{ga}$	$\Delta_{da}\,\Delta_{ha}\,\Delta_{ga}$	$\Delta_{da}\,\Delta_{ba}\,\Delta_{ga}$	$\Delta_{fa}\,\Delta_{ea}\,\Delta_{ga}$
ω_3 scan:	rectangular grid	rare	rare	parallelogram
ω_1 scan:	rare	rectangular grid	parallelogram	rare

Figure 4.8. Resonance vibrational patterns for the four parametric processes. The bottom two rows indicate the shape of the vibrational pattern ("rare" indicates that triple resonances are so infrequent that a regular repeating pattern may not be produced).

For process 4 (ω_3 scanned, ω_1 fixed), the resonance denominator Δ_{ea} produces a diagonal resonance line in the Δ_{fa} resonance plane. Therefore, the triply resonant vibrational patterns occur at intersections between vertical double resonance lines (from Δ_{ga}), diagonal double resonance lines (from Δ_{ea}), and the resonance plane Δ_{fa}. The resulting parallelogram pattern appears different from that of process 1; many peaks will have the same x-axis value, but they will not have the same y-axis values (except by accidental coincidence).

The resulting vibrational pattern changes if the ω_1 is scanned while ω_3 is fixed. If ω_3 has been tuned to a resonance, then the right side of the diagram in Figure 4.8 (in the Δ_{da} plane,

where $\Delta_{da} = \omega_{da} - \omega_3 - i\Gamma_{da} = -i\Gamma_{da}$) becomes useful and processes 2 and 3 now yield regularly spaced rectangular and parallelogram vibrational patterns. On the other hand, processes 1 and 4 now require the overlap of three separate resonance lines rather than the overlap of two resonance lines and one resonance plane. For process 1, two resonance lines are horizontal (Δ_{fa} and Δ_{ha}) while one is vertical (Δ_{ga}). Therefore, triple resonances only occur when the Δ_{fa} and Δ_{ha} resonance lines are on top of each other. Since this situation rarely occurs, peaks from this process are infrequent and are irregularly spaced along the y-axis. For process 4, Δ_{ea} and Δ_{ga} both produce vertical resonance lines, so triple resonances from this process are also rare and irregularly spaced along the x-axis.

Ultimately, the *strongest* FWM process depends upon the choice of lasers and the energy level diagrams of the molecule. For the purpose of pattern recognition, the *most useful* FWM process is one that produces both a rotational pattern with three peaks (as opposed to just one or two peaks) and a regular vibrational pattern (rectangular or parallelogram). The patterns that satisfy these two requirements for the choice of lasers discussed above ($\omega_1=\omega_{vis}$, $\omega_2= \omega_{broad}$ and $\omega_3= \omega_{nir}$) are processes 1 & 4 with an ω_3 scan and processes 2 & 3 with an ω_1 scan. Of these, the most useful strategy for conducting HRC3D experiments appears to be the latter, since processes 2 and 3 require resonances with overtones and combination bands in the ground electronic state that are usually weak. If this approach is taken, the vibrational and rotational patterns may then be used to determine whether process 1 or process 4 is responsible for the observed peaks. The combined rotational and vibrational patterns for the two best candidates (processes 1 and 4 with an ω_3 scan) are shown in Figure 4.9. Fortunately, these two processes are easy to discern because of their different vibrational patterns. Process 1 produces a vibrational pattern that aligns horizontally and vertically (i.e., a rectangular grid), while the ω_3-scanned process 4 creates

a vibrational pattern made from vertical and diagonal resonance lines (i.e., a parallelogram shaped grid). Furthermore, processes 1 and 4 yield different rotational patterns (see Figures 5 and 6). For process 4, none of the peaks have the exact same y-axis value (except by coincidence), and two of the peaks appear in both the P-type resonance and the R-type resonance (selected by ω_1). For process 1, two of the three peaks that form a "triangle" must have the exact same y-axis value, and all of the peaks will change their position when ω_1 is changed between a P-type resonance and an R-type resonance. The rotational spacing between peaks is also different for these two processes, as indicated in Figures 4.5 and 4.6.

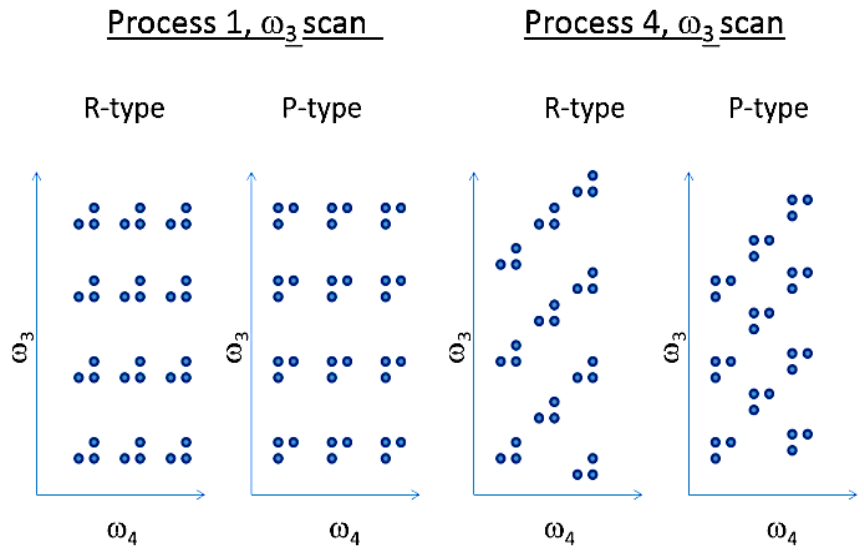

Figure 4.9. Combined rotational and vibrational patterns for processes 1 and 4 when ω_3 is scanned and ω_1 is fixed. For the Process 4 ω_3 scan spectra, none of the peaks have the same y-axis values, except by coincidence. All axes are in units of cm^{-1}.

One additional benefit of HRC3D spectroscopy over HRC2D spectroscopy is that it can provide information on intermediate levels. For example, consider the intermediate level **e** in process 4. For an ω_3 scan with a frequency equation of $\omega_4 = \omega_1 - \omega_2 + \omega_3$, the y-axis corresponds to ω_3 and the x-axis corresponds to ω_4. Rearranging the above equation yields a linear equation with a slope=1 and a y-intercept of ω_2-ω_1, which also equals ω_3-ω_4. Therefore, the difference in energy between level **e** and level **a** is equal to the negative of the y-intercept of the line that runs through the vibrational patterns that align diagonally in the spectrum. This line runs through the "common points" that are colored green in Figure 4.5. As mentioned earlier, these points are common to both the P-type and R-type patterns for a given J" value, while the other two points (red and yellow in Figure 4.5) only appear for the P-type and R-type triangles, respectively. The two common points are relatively easy to identify because the line forming them has a slope of m=1, and they therefore line up with other common points involving the same overtone or combination band (level **e**). A similar approach can be developed for process 1, where the energy of level **h** should be equal to ω_1+ω_3 for a given row.

If the sample consists of a mixture, it is possible that species selectivity may be achieved by analyzing only the patterns that lie along a specific diagonal corresponding to known overtones and combination bands of the molecule of interest. This pattern-based selectivity would be in addition to that made possible by fixing the dye laser at a specific wavelength during the ω_3 scan.

4.4 Experimental Methods

Nonlinear spectroscopy serves as a well-suited method for generating coherent multidimensional spectra because the resulting signal depends upon multiple beams that can have independently controllable frequencies, each of which can constitute an orthogonal axis in a multidimensional spectrum. Four wave mixing (FWM) techniques can therefore be used to generate spectra with up to 4 orthogonal frequency dimensions. By using three independently controllable beams to drive the FWM signal, fully (triply) resonant FWM signals can be generated that provide greater selectivity and resonant enhancement over doubly or singly resonant processes that might be used to create 1D or 2D spectra. The fully resonant FWM approach used in this work was pioneered by Wright and coworkers and makes effective use of the additional dimensions that are available when creating coherent 3D spectra.[19,20] The use of a broadband beam for one of the fields can facilitate multichannel detection with a CCD, which helps reduce the time required to acquire data. The FWM signals produced in this work were driven by three independent input beams (ω_1= narrowband tunable visible dye laser beam, ω_2 = broadband near-infrared OPO beam, and ω_3 = narrowband near-infrared tunable OPO beam). The use of three independent beams to drive fully (triply) resonant FWM processes allows us to explore and maximize the capabilities of coherent 3D spectroscopy.

A simplified diagram of the setup is shown in the top portion of Figure 4.10. Three independent injection-seeded Nd:YAG lasers (SpectraPhysics Lab 150, GCR 230, and PRO 250) were used to pump a dye laser (Coherent Scanmate plus, linewidth = 0.15 cm^{-1}), a broadband OPO (custom-built, linewidth >3000 cm^{-1})), and a narrowband tunable OPO (SpectraPhysics MOPO 730, linewidth = 0.2 cm^{-1}, pumped by 355 nm). The idler beam from the MOPO 730

was used in this experiment, but the wavelength of the idler beam was controlled using the signal beam wavelength ($\omega_{pump} = \omega_{signal} + \omega_{idler}$). The firing of the three pump lasers was synchronized using a delay generator (Stanford Research System DG 535). The three beams were combined using collinear phasematching before being focused into the sample cell. The pump beams were then removed by KG3 and BG40 absorption filters and a Semrock 633 nm notch filter. The remaining FWM beam was focused into a 1.25 meter monochromator (SPEX 1250m) equipped with a 2400 g/mm grating and CCD (2048 elements, 13 micron pixels).

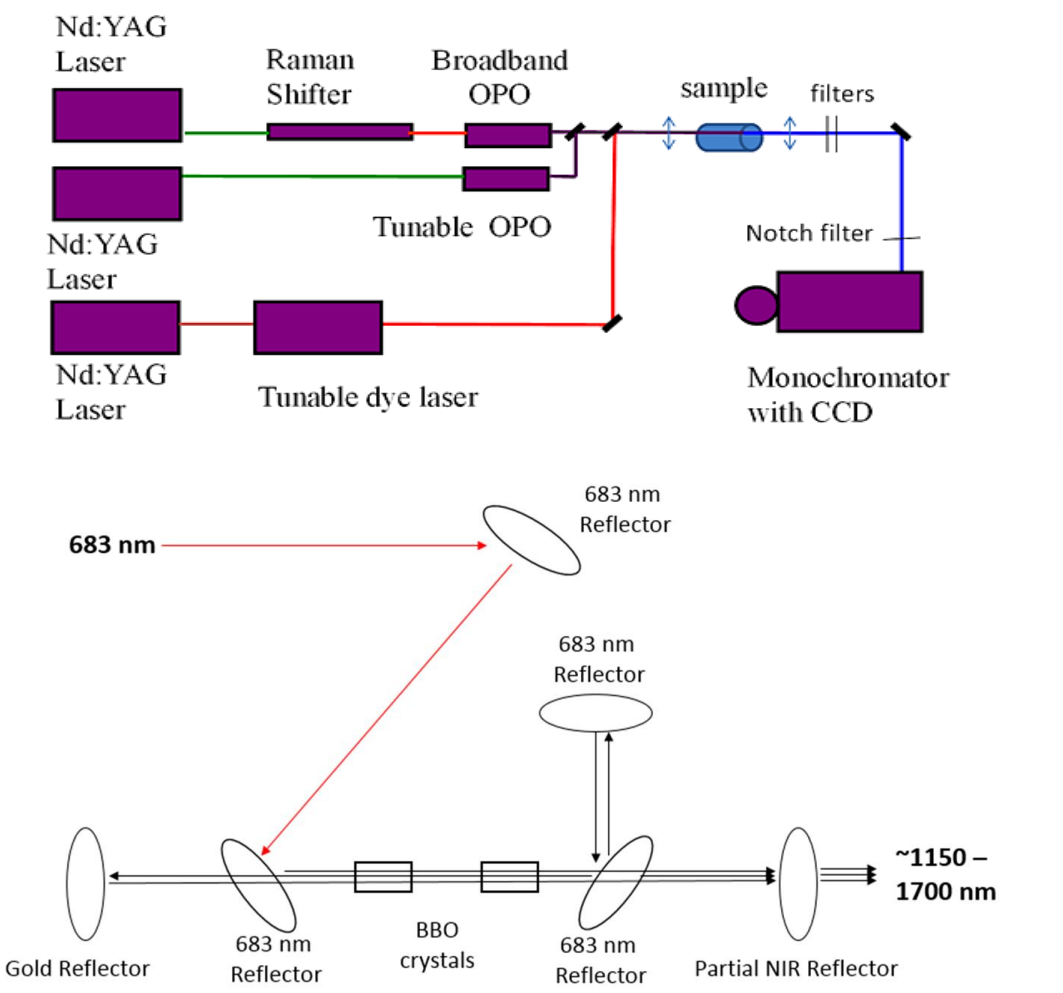

Figure 4.10. Top: Simplified experimental layout of the coherent 3D spectrometer. Bottom: Schematic diagram of the custom built broadband OPO used by Chen and coworkers.

In order to produce a single 2D slice of a coherent 3D spectrum, we set the dye laser to a specific wavelength, scanned the narrowband near infrared OPO (ω_3) wavelength, and collected a series of spectra using the monochromator and CCD (ω_4). During the scan, the dye laser wavelength was continuously monitored using a Bristol instruments 821 wavemeter. The resulting 1D spectra were stacked in order to produce the 2D slice. The wavelength of the light from the dye laser (ω_1) could then be changed in order to produce different 2D slices within the third dimension. Multichannel detection (needed to reduce the amount of time required to collect data) along the ω_4 axis was facilitated by the use of a degenerate OPO for ω_2, which was not tuned but generated broadband light covering a continuous range of wavelengths from 1150-1700 nm. A diagram of this broadband OPO is shown in the bottom portion of Figure 4.10. The three axes of the 3D spectra therefore correspond to ω_1, ω_3, and ω_4, with intensity as an additional (unplotted) dimension. For plotting purposes, the results are most clearly shown as a series of stackable 2D plots where the x and y axes correspond to ω_4 and ω_3 and peaks appear as dots. These peak positions were obtained using a modified version of a computer program (nmrDraw) that includes a two-dimensional peak picker.

Each 2D slice consists of approximately 5000 stacked 1D spectra, each taken with a specific ω_1 wavelength. Small step sizes (0.002 nm) that were a factor of 3 times smaller than the linewidth of the ω_3 beam were used in order to help distinguish FWM peaks from spurious peaks caused by cosmic rays that periodically hit the CCD detector. The "real" FWM peaks persist for several steps (appearing as a group of peaks along the y-axis) and are reproducible, while the cosmic ray spikes appear as single sporadic events that are irreproducible. The

acquisition time required to produce each 2D slice was approximately 2 hours. The spectra were repeated, and spurious cosmic ray spikes were removed using a Fortran computer program that eliminated many (but not all) of the irreproducible peaks.

The sample consisted of 0.001 atm of bromine in an evacuated 0.5 meter long glass cell. Bromine was selected because of its simplicity as a diatomic molecule and the availability of published spectroscopic constants for its *B* and *X* states.[22-25] The beam pulse energies were 3 mJ for the broadband OPO, 3 mJ for the narrowband tunable OPO, and 0.3 mJ for the dye laser. In order to ensure that the observed signal depended upon all three beams, we periodically blocked each beam and confirmed that the signal disappeared. The wavelengths of the dye and OPO beams were also changed to confirm that the signal was triply resonant.

4.5 Results and Discussion

Bromine is a spectroscopically well-characterized molecule that serves as a useful test case.[22-25] The well-known *B*-*X* transition for bromine involves light in the visible region, so achieving electronic resonance enhancements is easily accomplished using a visible dye laser. Previously published[20] HRC2D spectra of bromine show a considerable amount of congestion due to several factors. First, the rotational and vibrational spectroscopic constants are small due to the relatively large mass of the bromine atom. Second, the rotational constants B' (~0.06 cm^{-1}) and B" (~0.08 cm^{-1}) differ considerably, causing a rotational pattern of elongated double Fortrat parabolas. This elongation causes parabolas to run into each other. Third, bromine's 2D spectrum is further complicated because of the presence of peaks from all three naturally

occurring isotopologues ($^{79}Br_2$, $^{81}Br_2$, and $^{79,81}Br_2$). The parabolas produced by the isotopologues overlap; they are shifted in position from each other because their vibrational constants slightly differ. Finally, HRC2D spectroscopy does not provide the ability to use selectivity or other methods for addressing the resulting overlap and congestion problems.

HRC3D spectroscopy was used to reduce congestion by expansion to a third dimension. Selectivity was also explored by setting the visible dye laser frequency (ω_1) to match a resonance frequency for the species of interest. To produce the resulting 2D slice, the narrowband tunable near-infrared OPO idler beam was then scanned while the monochromator and CCD monitored the output beam. The results after setting the dye laser to 612.336 +/- 0.002 nm (16326.46 cm^{-1}) and scanning the near infrared OPO from 9290 - 10,000 cm^{-1} are shown in the top half of Figure 4.11. The data used to create this 2D slice is from the same coherent 3D spectroscopy experiment that was discussed in an earlier paper[21], where the spectra were not fully analyzed and interpreted. The concepts presented earlier in this chapter may now be used to complete this analysis.

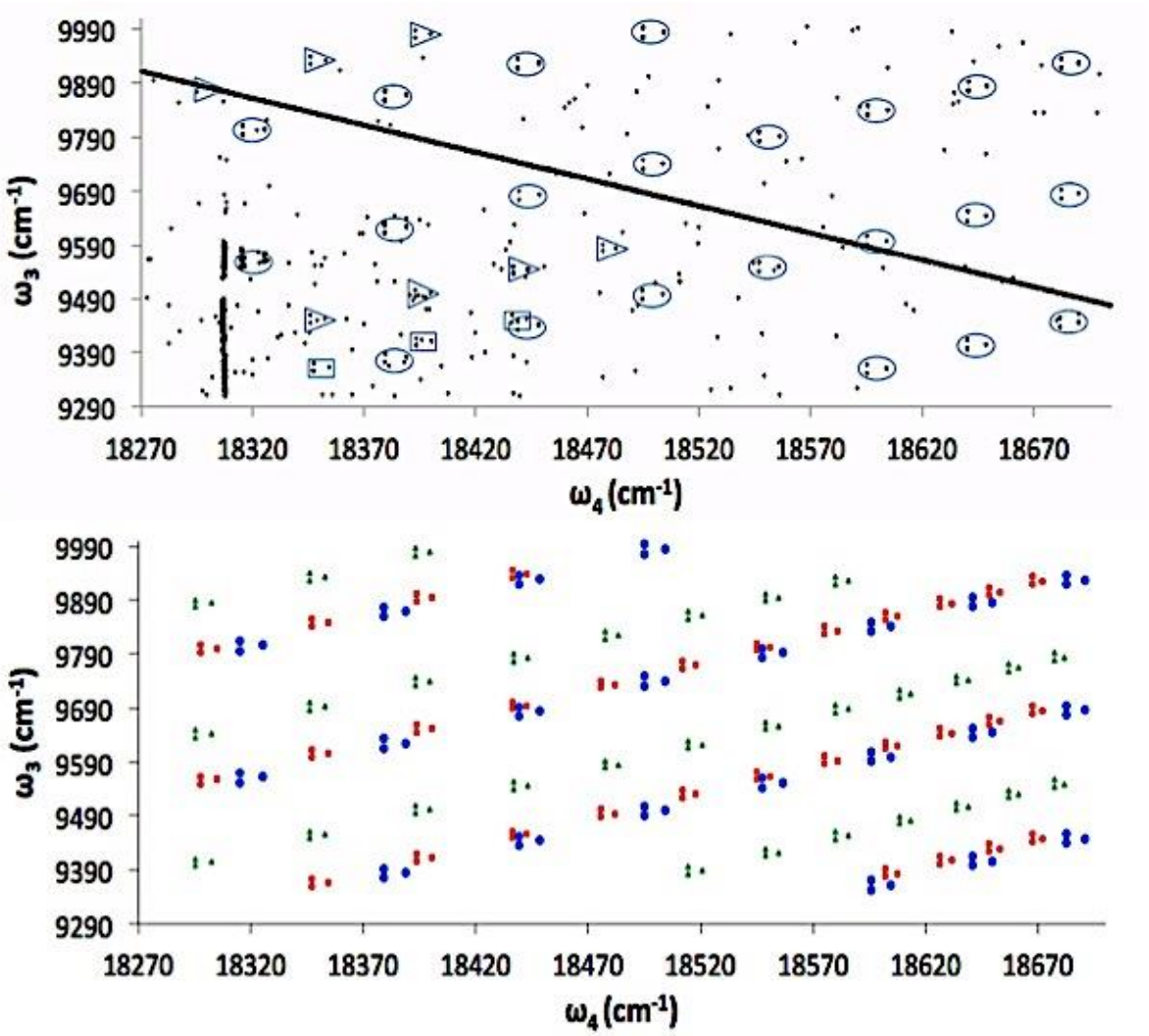

Figure 4.11. Coherent 3D spectrum of bromine with the dye laser set to 612.336 (+/- 0.002) nm. For the experimental spectrum (top), triangles are drawn around the observed $^{81}Br_2$ patterns, rectangles are drawn around the $^{79}Br_2$ patterns, and circles are drawn around the $^{79,81}Br_2$ patterns. The simulated spectrum on the bottom shows the peaks for the same three isotopologues, and are indicated by green, red, and blue markers.

The easily recognized patterns in this 2D slice immediately reveal several important features. First, the rotational patterns consist of multiple sets of three peaks that form repeating

triangles, indicating that the peaks are coming from either process 1 or 4. Process 1 can be eliminated because none of the triangles have the same y-axis values; the vibrational patterns reveal a structure that shows repeating columns, but not repeating rows. Instead, they resemble parallelograms (vertical and diagonal alignment), providing further evidence that process 4 is responsible for these peaks. The fact that there are at least two differently sized triangles (see the enclosing ovals, triangles, and rectangles in Figure 4.11) suggests the possibility of multiple sets of quantum numbers and/or isotopologues. Finally, each triangle consists of a sole peak on the right side, indicating that the ω_1 frequency in process 4 matches a P-type resonance.

The next step in the analysis was to determine the vibrational and rotational quantum numbers from the positions of the peaks in the 2D slice. The size and shape of a triangle reveal information about the rotational constants and quantum numbers, and relatively simple relationships between the triangle dimensions and the rotational constants and/or quantum number can be obtained. For example, the width of the triangle depends upon the two possible output (ω_4) frequencies for a given initial rotational quantum number. For process 4 (ω_3 scan), these two frequencies correspond to:

$$Te' - Te'' + G'(v') - G''(v'') + F'(J''+1) - F''(J'')$$

And

$$Te' - Te'' + G'(v') - G''(v'') + F'(J''-1) - F''(J'')$$

Where J" is the initial rotational quantum number of the molecule. If the molecule acts like a rigid rotor with a small amount of vibration-rotation interaction, then the difference between these two frequencies is

$$[B'(J"+1)(J"+2) - B"(J")(J"+1)] - [B'(J"+1)(J"+2) - B"(J")(J"+1)] = B' (4J"+2)$$

where B can be written in terms of Dunham coefficients ($B = Y_{01} + Y_{11}(v+1/2) + Y_{21}(v+1/2)^2 + \ldots$). The four y-axis ($\omega_3$) resonance frequencies, labeled A-D (see Figure 4.5) can be used to calculate the following y-axis spacings:

A-C: $B_e(4J"-2)$

B-C: $B_g(4J"+2)$

B-D: $B_e(4J"+6)$

where the subscripts on the rotational constants indicate the corresponding level in the accompanying four wave mixing diagram. Y-axis frequencies A, B, and C are involved in a P-type pattern, while frequencies B, C, and D are found in an R-type pattern. Since the shapes of the triangles in Figure 4.11 (two points on the left and one point on the right) correspond to a P-type rotational pattern, the spacings A-C and B-C may be helpful while analyzing this spectrum.

To illustrate this point, the following method was used to complete the assignment of quantum numbers for the triangles enclosed in ovals in Figure 4.11. This method is suitable for analyzing triangles produced by process 4 when ω_1 is held fixed and ω_3 is scanned. The first step was to identify a series of triangles that lie along the same diagonal. All peaks that comprise these triangles should have identical values of J" and v" for level **a** as well as an identical value of v" for level **e** (see Figure 4.1). Two of the three peaks in each triangle are "common peaks",

and a straight line with a slope of 1 can be drawn connecting all of these common peaks if both axes on the spectrum are in units of cm^{-1}. The negative of the y-intercept for the resulting diagonal line should be equal to the sum of $\Delta G + \Delta F$ between levels **e** and **a**. Values of ΔG for several v" → v" resonances between levels **a** and **e** were then calculated. For a room temperature sample, it was reasonable to assume that several vibrational levels (v"= 0-5 for level **a**) are initially populated. Two approximations were used to help determine the correct values of v" for levels **a** and **e**. The first assumption was that $\Delta G > \Delta F$, so that ΔG should be roughly comparable in size to the y-intercept. This assumption was used to calculate an approximate value of v" for level **e**, which was then used to calculate an approximate value for J" using the formula $A\text{-}C = B_e(4J"\text{-}2)$, where A-C is the difference in y-axis energy spacing between the two peaks in the triangle that share the same x-axis value. (For an R-type process, $A\text{-}C = B_e(4J"+6)$). The second assumption was that the value of ΔF is not highly dependent upon the value of J"; for Br_2, ΔF changed by only 1-2 cm^{-1} for neighboring values of J". The resulting values for $\Delta G + \Delta F$ were then compared with the y-intercept, and the best pairs of v" values (for energy levels **a** and **e**) were identified. The values of J" for these best fits were then refined to minimize the discrepancy. This procedure was carried out for all three isotopologues. The correct isotopologue could be easily identified because incorrect ones had simulated triangle widths (values of $B_g(4J"+2)$) that differed considerably from the observed experimental values (by several wavenumbers).

In addition to the triangles enclosed in ovals, additional unexpected patterns (enclosed in triangles and rectangles) in Figure 4.11 are attributed to additional ω_1 resonances due to the relatively wide linewidth of the dye laser (0.15 cm^{-1}). Both the expected and unexpected patterns could be assigned. The triangles enclosed in ovals correspond to a $^{79,81}Br_2$ resonance at 16326.42

cm^{-1}, where v"= 1, J"= 62 and v'= 6, J'= 61. Eight vertical columns of triangles are due to a vibrational pattern involving v' = 25-32 (from left to right) for level **g** and four diagonal lines of triangles are observed, corresponding to v" = 31-34 (top to bottom) for level **e**. The triangles enclosed in rectangles are attributed to a $^{79}Br_2$ resonance at 16326.53 cm^{-1}, where v"=2, J"=49 and v'=8, J'=48. Twelve columns of these triangles are attributed to the vibrational pattern involving v' = 29-40, while the four diagonal lines of triangles are due to v"=32-35. The triangles enclosed in triangles correspond to a $^{81}Br_2$ resonance at 16326.39 cm^{-1}, with v"=2, J"=48 and v'=8, J'=47. Twelve observed columns are due to v' = 29-40 and the four diagonals are due to v" = 32-35. The lower half of Figure 4.11 shows a simulation based upon these assignments. The spectroscopic constants used for this simulation were taken from references 22-24. The agreement between experimental and simulated peak positions along the x-axis and y-axis was typically within a few hundredths of a nanometer. The strong diagonal line that runs through the spectrum was caused by unwanted stray light from the MOPO 730 signal beam during the scan. The strong vertical line was caused by unwanted stray light from nearby fluorescent lights (Hg emission at λ = 546.075 nm).

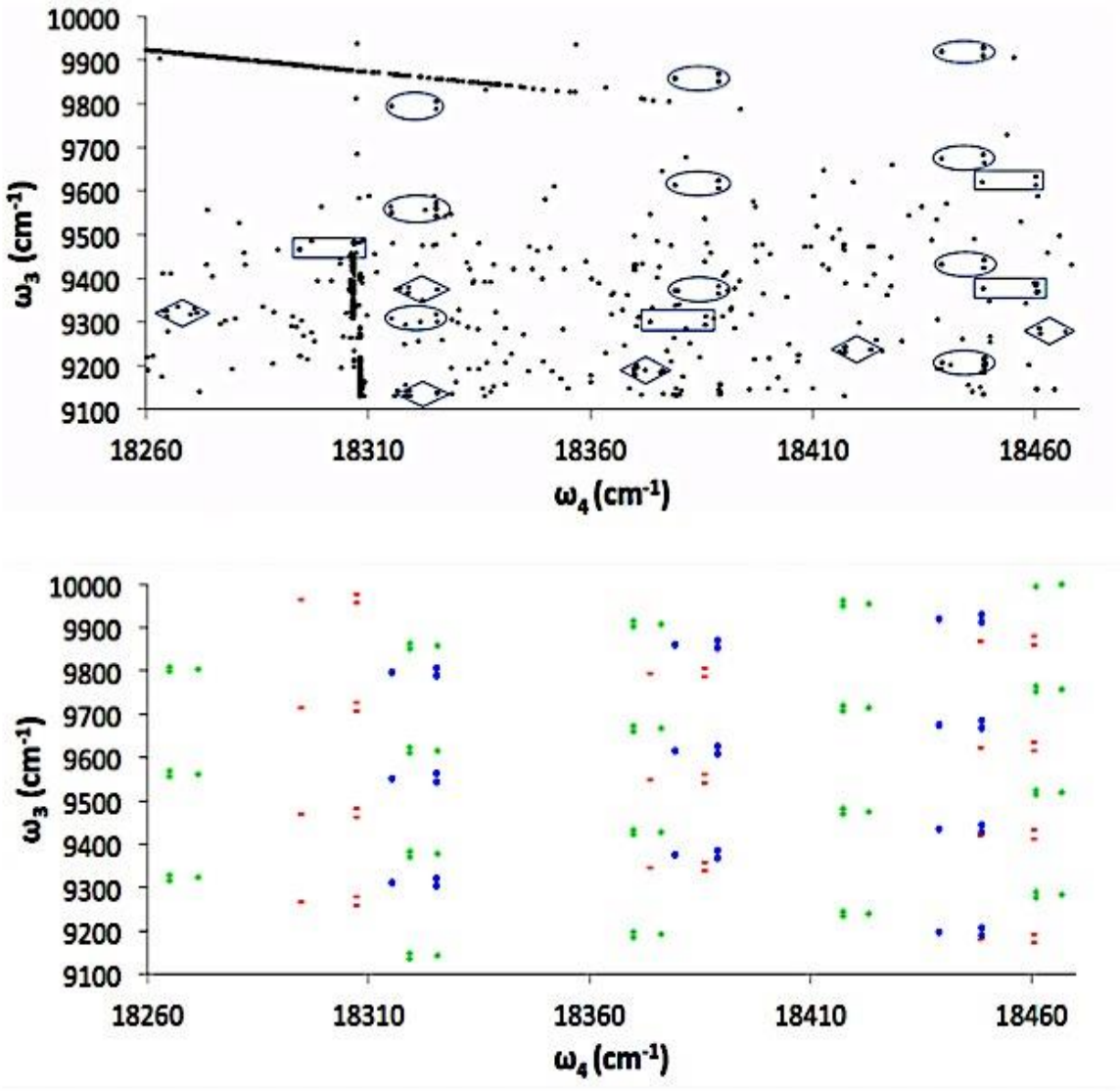

Figure 4.12. Coherent 3D spectrum of bromine when the dye laser is set to 611.821 (+/- 0.002) nm. All simulated peaks (lower half) were for $^{79,81}Br_2$: the blue and red dots (peaks) are for two different R-type processes and the green peaks are for a P-type process. For the experimental spectrum (top), different shaped circles, boxes, or triangles were used to indicate different v and J values, and colors were used for to differentiate these three types of peaks in the simulated spectrum. (See text for more details).

The top half of Figure 4.12 shows results after moving the dye laser to 611.821 (+/- 0.002) nm, which is very close to the wavelength predicted for the R-type counterpart to the

pattern in Figure 4.11 enclosed in ovals. The predicted value of this counterpart is 16340.21 cm^{-1} and involves a resonance between v"= 1, J"= 62 and v'= 6, J'= 63 for $^{79,81}Br_2$. The corresponding observed peaks in Figure 4.12 are also enclosed in ovals (blue dots in the simulated plots). For this pattern, the columns correspond to v' = 25-27 and the diagonals correspond to v" = 31-33. Once again, additional unexpected patterns were observed due to the relatively wide bandwidth of the dye laser. One of these patterns (enclosed in rectangles) was another R-type process at a calculated value of ω_1 = 16340.18 cm^{-1}, corresponding to v"=0, J"=71 to v'=4, J'=72 for the same isotopologue. For this pattern, the columns correspond to v' = 21-23 and the diagonals correspond to v" = 30-32. An additional unexpected pattern (enclosed in triangles) was observed and attributed to a P-type process at ω_1 = 16340.36 cm^{-1}, corresponding to v"=2, J"=43 to v'=8, J'=42, also for the same isotopologue. For this pattern, the columns correspond to v' = 28-32 and the diagonals correspond to v" = 32-35.

For both Figures 4.11 and 4.12, the experimental results show excellent agreement with simulated results (shown on the bottom half of these figures) that were based on the assigned quantum numbers above. Both experimental spectra are dominated by peaks from $^{79,81}Br_2$, with starting level quantum numbers v"= 1 and J"= 62. Unexpected peaks from other resonances and/or isotopologues can be distinguished from the expected ones because the vibrational and rotational patterns are significantly different; the size of the triangles and their locations in the plot are different. Vibrational and rotational pattern recognition therefore facilitates additional selectivity by providing the ability to determine the number of simultaneously contributing ω_1 resonances/isotopologues and to classify the peaks accordingly. Obviously, improved selectivity may also be achieved by using a dye laser with a narrower bandwidth.

4.6 Conclusion

HRC2D spectroscopy can be used to overcome problems of congestion and pattern obscuration in high-resolution spectroscopy. For the rotationally resolved electronic spectra of many gas phase molecules, however, expansion to the second dimension may not be sufficient to overcome severe congestion. HRC3D spectroscopy may be an effective way to fix these severe congestion problems; in addition to using an additional dimension to increase the spacing between peaks, HRC3D spectroscopy also provides selectivity by species and quantum number(s).

These findings suggest that the best approach for carrying out high-resolution coherent 3D spectroscopy may be to use one tunable visible/UV beam to select a resonance, and two near infrared beams, one that is scanned in frequency and the other that is broadband. This approach limits the number of possible FWM processes, and also employs multichannel detection to help reduce collection times that might otherwise be prohibitively long. Fixing the tunable visible/UV beam and scanning the tunable near infrared beam should produce spectra with patterns that are easier to recognize and interpret. In order to analyze molecules like bromine (e.g., no excited electronic states in the near infrared region), the FWM processes that are most likely to be successful are processes 1 and 4, which will produce rotational patterns consisting of three peaks that form triangles. These two processes are easily distinguishable based upon their different rotational and vibrational patterns. Achieving the desired fully-resonant FWM process may be easier for process 4 than process 1 because each field can create resonances between the ground electronic state and an excited electronic state; a simple system with a ground electronic state and just one bound excited electronic state would be sufficient. HRC3DS also provides a

possible method for identifying the intermediate level (**h** for process 1 and **e** for process 4) by studying the diagonals that can be drawn between triangles in HRC3D spectra.

After analyzing the vibrational and rotational patterns to identify the process, one can use the shapes of the patterns to determine quantum numbers and assign peaks, provided that high quality spectroscopic constants are known. One can imagine that the reverse should also be true; determining the spectroscopic constants should be possible if the quantum numbers are known. Doing so, however, will probably require the acquisition of a substantial number of 2D slices. Each slice requires a couple of hours to acquire, so the time required to generate a complete 3D cube, or enough of a cube to obtain a full set of Dunham coefficients, could be considerable. Nonetheless, considerable time and effort might be worth it for molecular systems that have otherwise evaded analysis.

4.7 References

[1]J. C. Wright, *Ann. Rev. Phys. Chem.* **62**, 209 (2011).

[2]D. Jonas, *Ann. Rev. Phys. Chem*. **54**, 425 (2003).

[3]M. Cho, *Chem. Rev*. **2008**, **108**, 1331 (2008).

[4]S. Mukamel, *Ann. Rev. Phys. Chem.* **51**, 691 (2000).

[5]F. Fournier, E. M. Gardner, D. A. Kedra, P. M. Donaldson, R. Guo, S. A. Butcher, I. R. Gould, K. R. Willison, and D. R. Klug, *Proc. Nat. Acad. Sci.* **105**, 15352 (2008).

[6]S. D. Moran, A. M. Woys, L. E. Buchanan, E. Bixby, S. M. Decatur, and M. T. Zanni, *Proc. Nat. Acad. Sci.* **109**, 3329 (2012).

[7]D. Hayes and G. S. Engel, *Biophys. J.* **100**, 2043 (2011).

[8]F. Ding and M. T. Zanni, *Chem. Phys.* **341**, 95 (2007).

[9]D. B. Turner, K. W. Stone, K. Gundogdu, and K. A. Nelson, *J. Chem. Phys.* **131**, 144510 (2009).

[10]M. Cho, *J. Chem. Phys.* **115**, 4424 (2001).

[11]A. F. Fidler, E. Harel, and G. S. Engel, *J. Phys. Chem. Lett*. **1**, 2876 (2010).

[12]S. Garrett-Roe and P. Hamm, *J. Chem. Phys.* **130**, 164510 (2009).

[13]S. Garrett-Roe and P. Hamm, *Acc. Chem. Res.* **42**, 1412 (2009).

[14]J. A. Davis, C. R. Hall, L. V. Dao, K A. Nugent, H. M. Quiney, H. H. Tan, and C. Jagadish, *J. Chem. Phys.* **135**, 44510 (2011).

[15]S. S. Mukherjee, D. R. Skoff, C. T. Middleton, and M. T. Zanni, *J. Chem. Phys.* **139**, 144205 (2013).

[16]P. C. Chen, *J. Phys. Chem. A* **114**, 11365 (2010).

[17]P. C. Chen and C. C. Joyner, *Anal. Chem.* **77**, 5467 (2005).

[18]P. C. Chen and C. C. Joyner, *J. Phys. Chem. A* **110**, 7989 (2006).

[19]P. C. Chen and K. Mitchell, *J. Chem. Phys.* **129**, 194301 (2008).

[20]P. C. Chen and M. Gomes, *J. Phys. Chem. A* **112**, 2999 (2008).

[21]P. C. Chen, T. A. Wells, and B. R. Strangfeld, *J. Phys. Chem. A* **117**, 5981 (2013).

[22]C. Focsa, H. Li, and P. F. Bernath, *J. Mol. Spectrosc*. **200**, 104 (2000).

[23]S. Gerstenkorn, P. Luc, A. Raynal, and J. Sinzelle, *J. Phys. (France*) **48**, 1685 (1987).

[24]S. Gerstenkorn and P. Luc, *J. Phys. (France*) **50**, 1417 (1989).

[25]R. F. Barrow, T. C. Clark, J. A. Coxon, and K. K. Yee, *J. Mol. Spectrosc.* **51**, 428 (1974).